

OXIDATION BEHAVIOR OF ZIRCONIUM ALLOYS IN TRANSIENT  
CONDITIONS

by

Jordan Lee Vandegrift



A thesis

submitted in partial fulfillment

of the requirements for the degree of

Master of Science in Materials Science and Engineering

Boise State University

August 2019

Jordan Lee Vandegrift

SOME RIGHTS RESERVED



This work is licensed under a Creative  
Commons Attribution-Noncommercial 4.0  
License.

BOISE STATE UNIVERSITY GRADUATE COLLEGE

**DEFENSE COMMITTEE AND FINAL READING APPROVALS**

of the thesis submitted by

Jordan Lee Vandegrift

Thesis Title: Oxidation Behavior of Zirconium Alloys in Transient Conditions

Date of Final Oral Examination: 13 June 2019

The following individuals read and discussed the thesis submitted by student Jordan Lee Vandegrift, and they evaluated her presentation and response to questions during the final oral examination. They found that the student passed the final oral examination.

Brian J. Jaques, Ph.D., P.E. Chair, Supervisory Committee

Michael Hurley, Ph.D. Member, Supervisory Committee

Clementè J. Parga, Ph.D. Member, Supervisory Committee

The final reading approval of the thesis was granted by Brian J. Jaques, Ph.D., P.E., Chair of the Supervisory Committee. The thesis was approved by the Graduate College.

## DEDICATION

For my family.

## ACKNOWLEDGEMENTS

I would like to start by thanking Dr. Darryl Butt, who gave me the opportunity to start my research career in the Advanced Materials Laboratory (AML) during my second year as an undergraduate. It was during this time that I developed the skills and passion for research that I would carry with me to graduate school. During this time, I got the privilege of working with Dr. Patrick Price, who I would like to thank for showing me the importance of doing careful science and for his continued support. Additionally, I would like to thank Dr. Brian Jaques for teaching me leadership, work/life balance and for providing me with countless opportunities to grow as an engineer. Most importantly, Dr. Jaques taught me the value of learning something new every day, and I will carry that mindset with me for the rest of my career.

I would like to thank my other committee members, Dr. Hurley and Dr. Parga for their support and guidance. I would also like to thank my peers at Boise State University for their support during this journey and for being excellent role models both in the lab and in life. Finally, I want to thank my friends and my family for pushing me to take every opportunity that has come my way. Without their continued support, this thesis would not exist.

## ABSTRACT

The effect of sample geometry, welding strategies, atmosphere, plastic deformation, and rapid heating on the oxidation behavior of zirconium alloys has been investigated in this work. The goal of this work was to determine which zirconium alloy would be best suited as nuclear fuel cladding material in the Transient Reactor Test (TREAT) facility at the Idaho National Laboratory (INL), which has unique operating conditions compared to typical reactors. TREAT is air-cooled, operates at high temperatures (400-600 °C), and produces rapid transients ( $\leq 700$  °C/s). Additionally, TREAT's cladding geometry is unique in that it has chamfers and welds. Alloying elements such as Fe, Sn, Cr, and Nb are typically added to zirconium and can drastically alter the corrosion properties of the material. The effects of such fabrication on the oxidation behavior of zirconium alloys is not well documented in literature and no direct comparison is provided for the alloys of interest, thus it is unclear how these alloys will behave under TREAT's conditions.

Isothermal and non-isothermal oxidation studies were completed on pure Zr, Zircaloy-3 (Zry-3), Zircaloy-4 (Zry-4), Zr-1Nb, and Zr-2.5Nb plate specimens in both Ar+20%O<sub>2</sub> and N<sub>2</sub>+20%O<sub>2</sub> to study the effect of nitrogen on the oxidation behavior. Electron beam welded (EBW) and tungsten inert gas (TIG) welded Zry-3, Zry-4, and Zr-1Nb tube samples were oxidized under rapid heating and isothermal conditions in dry and humid N<sub>2</sub>+20%O<sub>2</sub>. Through these studies, the effect of chamfering, welding, humidity, and rapid heating were characterized. Macroscopic images of the samples were taken after

oxidation, the oxide thickness was measured, and mass gain data was used to determine the oxidation rate constants and activation energies.

It was found that Zry-3, Zry-4, and Zr-1Nb experience faster oxidation in  $N_2+20\%O_2$  than  $Ar+20\%O_2$  at 800 °C, while Zr and Zr-2.5Nb were relatively unaffected. Zry-3, Zry-4, and Zr-1Nb were found to experience accelerated oxidation in the weld region. Additionally, Zry-3 and Zry-4 experienced accelerated oxidation at the chamfers, while the chamfered region of Zr-1Nb experienced less oxidation. In all oxidation experiments, Zr-1Nb had the most favorable oxidation behavior.

## TABLE OF CONTENTS

DEDICATION .....	iv
ACKNOWLEDGEMENTS .....	v
ABSTRACT .....	vi
LIST OF TABLES .....	xii
LIST OF FIGURES .....	xiv
LIST OF ABBREVIATIONS .....	xiv
CHAPTER ONE: INTRODUCTION .....	1
1.1 Motivation .....	3
1.2 Oxidation of Zirconium Alloys in Air .....	5
1.3 Effect of Alloying Elements on Oxidation Behavior .....	6
1.4 Welding of Zirconium Alloys .....	7
1.5 References .....	8
CHAPTER TWO: OXIDATION BEHAVIOR OF ZIRCONIUM, ZIRCALOY-3, ZIRCALOY-4, ZR-1NB, AND ZR-2.5NB IN AIR AND OXYGEN .....	12
Oxidation Behavior of Zirconium, Zircaloy-3, Zircaloy-4, Zr-1Nb, and Zr-2.5Nb in Air and Oxygen .....	13
2.1 Abstract .....	13
2.2 Introduction .....	14
2.3 Experimental Procedures .....	16
2.3.1 Specimens .....	16

2.3.2 Oxidation Experiments .....	17
2.3.3 Post Test Characterization .....	18
2.4 Results.....	19
2.4.1 Oxidation Behavior .....	19
2.5 Discussion.....	26
2.5.1 Oxidation Kinetics .....	26
2.5.2 Pre-Breakaway.....	30
2.5.3 Post-Breakaway .....	31
2.6 Conclusion .....	32
2.7 Acknowledgements.....	33
2.8 References.....	33
<b>CHAPTER THREE: OXIDATION BEHAVIOR OF WELDED ZRY-3, ZRY-4, AND ZR-1NB TUBES.....</b>	<b>36</b>
Oxidation Behavior of Welded Zry-3, Zry-4, and Zr-1Nb Tubes .....	37
3.1 Abstract.....	37
3.2 Introduction.....	38
3.3 Experimental Procedures .....	41
3.3.1 Materials .....	41
3.3.2 Isothermal Oxidation .....	41
3.3.3 Transient Oxidation .....	43
3.4 Results.....	45
3.4.1 Isothermal Oxidation .....	45
3.4.2 Transient Oxidation .....	51
3.5 Discussion.....	52

3.5.1 General Oxidation Behavior .....	52
3.5.2 Effect of Welding and Plastic Deformation on Oxidation Behavior	53
3.5.3 Transient Oxidation .....	60
3.6 Conclusion .....	61
3.7 Acknowledgements.....	63
3.8 References.....	63
CHAPTER FOUR: OXIDATION BEHAVIOR OF ZR-ALLOY CLADDING CANDIDATES FOR THE TREAT REACTOR.....	67
Oxidation Behavior of Zr-alloy Cladding Candidates for the TREAT Reactor ....	68
4.1 Abstract.....	68
4.2 Introduction.....	69
4.3 Experimental Procedures .....	71
4.3.1 Isothermal Oxidation .....	71
4.3.2 Transient Oxidation .....	73
4.3.3 Raman and SKPFM Characterization.....	74
4.4 Results.....	75
4.4.1 Isothermal Oxidation .....	75
4.4.2 Transient Oxidation .....	79
4.4.3 Raman and SKPFM Characterization.....	80
4.5 Discussion.....	82
4.5.1 Effect of Welding, Chamfering, and Alloying.....	82
4.5.2 Effect of Oxide Phase and Stresses at Interface.....	84
4.6 Conclusion .....	86
4.7 Acknowledgements.....	87

4.8 References.....	87
CHAPTER FIVE: CONCLUSIONS .....	93
APPENDIX.....	96
Determination of Zirconium Oxide Chemistry Through Complementary Characterization Techniques.....	97
A.1 Abstract .....	97
A.2 Introduction.....	98
A.3 Experimental Methods .....	100
A.4 Results and Discussion.....	102
A.4.1 Thermogravimetric Analysis.....	102
A.4.2 Raman Spectroscopy.....	103
A.4.3 Scanning Kelvin Probe Force Microscopy .....	110
A.4.4 Atom Probe Tomography.....	112
A.5 Conclusions.....	114
A.6 Acknowledgments.....	115
A.7 References .....	116

## LIST OF TABLES

Table 2.1:	Composition (wt %) of zirconium alloys presented here.....	17
Table 2.2:	Time to breakaway determined from isothermal oxidation experiments (Figure 2.4) and oxide thickness of pure zirconium, Zry-3, Zry-4, Zr-1Nb, and Zr-2.5Nb after 20-hour isothermal oxidation in air and oxygen environments.....	25
Table 2.3:	Constants and slopes obtained from Arrhenius fits (Equation 2) as described above. The Arrhenius dependence for zirconium and zirconium alloys before and after breakaway during isothermal oxidation in oxygen is shown in Figure 2.8.....	29
Table 2.4:	Calculated activation energies ( $E_a$ ) of each alloy in air or oxygen compared to values reported in literature. Activation energies are calculated for pre-breakaway (Pre-B) and post-breakaway (Post-B) regimes.....	29
Table 3.1:	Typical composition of zirconium alloys in wt % [24]. .....	41
Table 3.2:	Constants, $R^2$ values, and calculated activation energies for oxidation of chamfered and welded Zry-3, Zry-4, and Zr-1Nb in air obtained from Arrhenius fits. ....	53
Table 4.1:	Typical composition (wt%) of zirconium alloys investigated in this work [1].....	71
Table 4.2:	Average oxide thickness and standard deviation of sections of the welded tubes oxidized at 700 °C for 20 hours in dry or humid air. ....	84
Table A.1:	Zirconium alloy compositions. ....	100
Table A.2:	Approximate oxide thickness of each sample, pre- and post-breakaway, to the nearest 5 $\mu\text{m}$ . ....	102

Table A.3: Notable tetragonal (T) and monoclinic (M) zirconia Raman peak positions  
[16,20,25,27,29,44,46-48]..... 104

## LIST OF FIGURES

Figure 1.1:	Rendering of the fuel cladding assembly to be used in the TREAT facility. ..... 5
Figure 1.2:	Microstructure of an electron-beam welded zirconium alloy. .... 7
Figure 2.1:	Backscatter SEM images of the as received microstructure of the materials investigated. .... 17
Figure 2.2:	Image showing the custom sample setup for the TGA. The platinum sample carrier is loaded with a notched alumina crucible to minimize contact between the sample and crucible while maximizing the surface area exposed to the oxidizing gas. .... 18
Figure 2.3:	Non-isothermal mass gain of pure Zr, Zry-3, Zry-4, Zr-1Nb, and Zr-2.5Nb in synthetic air, oxygen, and nitrogen. Samples were heated to 940 °C at 20 °C/min. Inset shows macro-images of the surface of the Zry-4 after non-isothermal oxidation..... 20
Figure 2.4:	Normalized mass gain versus isothermal oxidation time of Zr, Zry-3, Zry-4, Zr-1Nb, and Zr-2.5Nb in air and oxygen at 400-800 °C. The inset in the 800 °C graph is the first two hours of the isothermal oxidation showing the onset of breakaway in Zry-3, Zry-4, and Zr-2.5Nb. .... 21
Figure 2.5:	Macro images of the surface of each alloy showing the material degradation after 20-hour isothermal oxidation at 600, 700, and 800 °C in air and oxygen..... 23
Figure 2.6:	Representative sample cross-sections after oxidation. The specimen shown is Zry-4 after oxidation in air and oxygen at 600 °C and 800 °C. .... 24
Figure 2.7:	Average measured oxide thickness versus isothermal oxidation temperature in air and oxygen for all cladding materials. The error increases with increasing oxidation temperature due to the cracked nature of the oxide. The inset shows cross-section images of Zry-4 after 20 hours of isothermal oxidation at 800 °C. .... 26
Figure 2.8:	Arrhenius dependence of oxidation rate constant as a function of temperature after isothermal oxidation in oxygen where $K_p$ and $K_I$ are the

	parabolic and linear rate constants, respectively. The activation energy for oxidation can be derived from the slope of the plot according to Equation 2.....	28
Figure 2.9:	Calculated activation energies for Zr, Zry-3, Zry-4, Zr-1Nb, and Zr-2.5Nb compared to reported values. Solid symbols represent values obtained from oxidation in air, hollow symbols represent values obtained from oxidation in oxygen.....	31
Figure 3.1:	Rendering of TREAT's unique fuel cladding assembly, which includes chamfered corners and welded end caps.....	40
Figure 3.2:	Experimental setup inside the STA showing a welded tube specimen on the platinum mesh plate. ....	42
Figure 3.3:	Transient oxidation temperature profile followed for each sample showing fifteen transients from 600 – 500 °C simulating normal TREAT operation, followed by a DBA temperature profile from 820 – 450 °C. ....	44
Figure 3.4:	Experimental setup for transient oxidation experiments. A pure Zr tube with a thermocouple spot welded to the surface was inserted into the furnace with the EBW zirconium alloy tube to monitor temperature during the experiment.....	45
Figure 3.5:	Macroscopic images of Zry-3 EBW or TIG welded tubes after isothermal oxidation experiments in dry or humid air.....	46
Figure 3.6:	Macroscopic images of Zry-4 EBW or TIG welded tubes after isothermal oxidation experiments in dry or humid air.....	47
Figure 3.7:	Macroscopic images of Zr-1Nb EBW or TIG welded tubes after isothermal oxidation experiments in dry or humid air.....	48
Figure 3.8:	Mass gain normalized to measured initial surface area during isothermal oxidation experiments of EBW or TIG welded Zry-3, Zry-4, Zr-1Nb tubes in dry or humid air. ....	49
Figure 3.9:	Oxide thickness of each section of the welded tubes after 20-hour isothermal oxidation at 700 °C. The error bars are the standard deviation of 15 (weld) or 30 (bulk and chamfer) measurements.....	51

Figure 3.10:	EBW Zry-3, Zry-4, and Zr-1Nb after N = 0, 1, 15 (600 °C) and DBA (820 °C) transient oxidation cycles.....	52
Figure 3.11:	Dark field optical images of as received (AR) EBW Zry-3 and after 20-hour isothermal oxidation at 700 °C in dry air. The microstructure of the weld, chamfered, and bulk regions are shown.....	54
Figure 3.12:	Dark field optical images of as received (AR) EBW Zry-4 and after 20-hour isothermal oxidation at 700 °C in dry air. The microstructure of the weld, chamfered, and bulk regions are shown.....	55
Figure 3.13:	Dark field (weld) and bright field (chamfer and bulk) optical images of as received (AR) EBW Zr-1Nb and after 20-hour isothermal oxidation at 700 °C in dry air. The microstructure of the weld, chamfered, and bulk regions are shown. ....	55
Figure 3.14:	SEM images of the weld and bulk microstructure of as received (AR) and oxidized (700 °C dry air) EBW Zry-3. All images were collected using backscatter electrons. The circles on the images after oxidation highlight high concentration Fe precipitates. ....	56
Figure 3.15:	SEM images of the weld and bulk microstructure of as received (AR) and oxidized (700 °C dry air) EBW Zry-4. All images were collected using backscatter electrons except the oxidized weld region, which is a secondary electron image.....	57
Figure 3.16:	SEM images of the weld and bulk microstructure of as received (AR) and oxidized (700 °C dry air) EBW Zr-1Nb. All images were collected using backscatter electrons. The circles on the images highlight the Nb and O-rich precipitates identified through EDS.....	58
Figure 3.17:	SEM image and corresponding EDS maps of Fe-rich precipitates found at the grain boundaries of the non-welded regions of as received EBW Zry-3. The intensity of the EDS maps corresponds to concentration of the element in the material.....	59
Figure 3.18:	Average mass gain between runs 1 and 2 and associated theoretical oxide thickness after each 600 °C transient (N = 1-15) and after the final 820 °C DBA transient. Maximum allowed oxide thickness (17% of the original wall thickness) is shown for reference. The inset shows a magnified view	

	of the mass gain and theoretical oxide thickness after the 600 °C transients. ....	61
Figure 4.1:	Specimen geometries investigated with isothermal oxidation: A) plate samples and B) welded and chamfered tubes representative of TREAT's cladding.....	73
Figure 4.2:	Normalized mass gain during isothermal oxidation of Zry-3, Zry-4, and Zr-1Nb plate samples at 800 °C in air (solid lines and closed symbols) or oxygen (dashed lines and open symbols).....	76
Figure 4.3:	Macroscopic images of Zry-3, Zry-4, and Zr-1Nb plate samples after 20-hour isothermal oxidation at 800 °C in air or oxygen.....	76
Figure 4.4:	Normalized mass gain during isothermal oxidation of Zry-3, Zry-4, and Zr-1Nb EBW and TIG welded tubes in dry or humid air. ....	78
Figure 4.5:	Macroscopic images of Zry-3, Zry-4, and Zr-1Nb welded tube specimens after isothermal oxidation at 800 °C in dry and humid air. The specimens were oxidized for different lengths of time to minimize spallation of the material inside the STA. ....	79
Figure 4.6:	Images of Zry-3, Zry-4, and Zr-1Nb EBW tubes after transient oxidation experiments. The images in the left column are specimens after two successive rapid 600 °C transients in the induction furnace. The middle column shows specimens after fifteen 600 °C transients in the muffle furnace. The right column represents specimens after fifteen 600 °C transients and one 820 °C transient.....	80
Figure 4.7:	SKPFM mapping of oxidized Zry-3 after breakaway. Identified precipitates (Fe, Sn, and O) confirmed with EDS, where the intensity of the color in the map is proportional to the concentration of the element. ....	81
Figure 4.8:	SEM image, % tetragonality map, and stress map at the metal/oxide interface of Zry-3 and Zry-4 oxidized at 700 °C in air to points before and after breakaway.....	82
Figure A.1:	TGA results for each zirconium alloy, pre-breakaway designated with solid lines, post-breakaway with dotted lines. ....	103

Figure A.2:	(a) Optical image of pre-breakaway Zr sectioned sample. White lines separate (left) epoxy/oxide and (right) oxide/metal interfaces. Blue line displays collected Raman line scan. (b) Spectra from collected Raman line scan, with notable peak ranges presented. (c) Percent tetragonality and (d) position of the $M_7$ peak as a function of distance from the metal/oxide interface. (e) Percent tetragonality as a function of the $M_7$ peak position. .... 107
Figure A.3:	(a) Optical image of pre-breakaway Zr sectioned sample. White lines separate (left) epoxy/oxide and (right) oxide/metal interfaces. Orange rectangle displays collected Raman map area. (b) Percent tetragonality and (c) position of the $M_7$ peak as a function of location. Grey represents metal, where Raman peaks are non-apparent. (d) Percent tetragonality as a function of the $M_7$ peak position for the data collected in the Raman map. .... 107
Figure A.4:	Raman mapping analysis for (top to bottom) post-breakaway Zr, pre- and post-breakaway Zr-2.65Nb, pre- and post-breakaway Zry-3, pre- and post-breakaway Zry-4. .... 109
Figure A.5:	Topography (left) and Volta potential (right) maps for pre- and post-breakaway Zr, Zr-2.65Nb, Zry-3, and Zry-4. Oxide/metal interfaces are noted in each map. .... 112
Figure A.6:	APT results from pre-breakaway Zr sample. (Left) Tip dimensions are $75.9 \times 74.6 \times 223.8 \text{ nm}^3$ , with the arrow representing a $4 \times 4 \times 60 \text{ nm}^3$ volume. (Right) 1D concentration profile of zirconium and oxygen, with phases segregated. Fixed bin size of 0.5 nm was used. .... 113
Figure A.7:	APT results from post-breakaway Zr-2.65Nb sample. (Top) Tip dimensions are $103.8 \times 97.9 \times 285.7 \text{ nm}^3$ , with the arrow representing a $5 \times 5 \times 150 \text{ nm}^3$ volume. (Bottom) 1D concentration profile of zirconium and oxygen across the volume, with average concentrations noted in each “tier”. Fixed bin size of 0.5 nm was used. .... 114

## LIST OF ABBREVIATIONS

AML	Advanced Materials Laboratory
TREAT	Transient Reactor Test
INL	Idaho National Laboratory
Zry-3	Zircaloy-3
Zry-4	Zircaloy-4
EBW	Electron Beam Weld
TIG	Tungsten Inert Gas
SKPFM	Scanning Kelvin Probe Force Microscopy
SPP	Secondary Phase Precipitate
EDS	Energy Dispersive X-ray Spectroscopy
HEU	High Enriched Uranium
LEU	Low Enriched Uranium
FZ	Fusion Zone
HAZ	Heat Affected Zone
HCP	Hexagonal Close-Packed
BCC	Body-Centered Cubic

## CHAPTER ONE: INTRODUCTION

This thesis consists of one publication, one paper and one conference proceeding. The research presented in Chapter Two has been published in Nuclear Materials and Energy. The research presented in Chapter Three is being prepared for submission to Nuclear Materials and Energy. The conference proceeding presented in Chapter Four has been submitted for publication in the proceedings of the Top Fuel 2019 conference. Chapter Two includes a study in which the effect of mixed oxygen/nitrogen atmosphere on the oxidation behavior of pure Zr, Zry-3, Zry-4, Zr-1Nb, and Zr-2.5Nb is characterized. It has been shown that oxidation in a mixed oxygen/nitrogen atmosphere results in increased oxidation kinetics due to the formation and re-oxidation of ZrN [1–9]. In-situ mass gain data was measured during isothermal oxidation experiments at 400, 600, 700, and 800 °C in Ar+20%O<sub>2</sub> or N<sub>2</sub>+20%O<sub>2</sub> and used to determine the oxidation rate constants and activation energies. This chapter concludes that Zry-3, Zry-4, and Zr-1Nb are the most affected by nitrogen in the oxidizing atmosphere and exhibit faster oxidation kinetics in N<sub>2</sub>+20%O<sub>2</sub> than Ar+20%O<sub>2</sub>.

Chapter Three, being prepared for publication in Nuclear Materials and Energy, outlines a study where the effects of welding, plastic deformation (chamfering), humidity, and rapid heating on Zry-3, Zry-4, and Zr-1Nb are investigated. Isothermal oxidation studies were performed at 500, 600, 700, 800, and 820 °C in dry and humid (30% relative humidity) N<sub>2</sub>+20%O<sub>2</sub> and the oxidation rate constants and activation energies were calculated. Two weld types were investigated: electron beam weld (EBW) and tungsten

inert gas (TIG) weld. Rapid thermal transients with heating rates up to 700 °C/s were performed using an induction furnace and a muffle furnace. It was determined that all three alloys exhibited accelerated oxidation in the weld regions, which resulted in failure during isothermal oxidation at 800 and 820 °C. Zry-3 and Zry-4 experienced accelerated oxidation at the chamfers, however Zr-1Nb did not. The oxidation behavior of TIG and EBW tubes were similar in Zry-3 and Zry-4. During isothermal oxidation of Zr-1Nb at 800 and 820 °C, the EBW tubes exhibited slower oxidation kinetics than TIG welded tubes. Similarly, the oxidation behavior in humid air was similar to that in dry air. The rapid transient oxidation experiments showed similar trends as the isothermal oxidation experiments.

Chapter Four, submitted for publication in the proceedings of the Top Fuel 2019 conference, combines and summarizes studies on the effect of atmosphere, welding, chamfering, and transient heating in the temperature range 400-820 °C on the oxidation behavior of Zry-3, Zry-4, and Zr-1Nb. Additionally, the mechanism of breakaway oxidation is investigated through advanced characterization techniques, including Raman spectroscopy and scanning Kelvin probe force microscopy (SKPFM). Specimens of each alloy (Zry-3 and Zry-4) were isothermally oxidized at 700 °C in dry air. Raman was used to map the percent tetragonality and induced stress, and SKPFM was coupled with energy dispersive x-ray spectroscopy (EDS) to characterize the secondary phase precipitates (SPPs) at the interface both before and after the onset of breakaway oxidation. It is highlighted, as in Chapter Two, that all alloys exhibit the breakaway transition sooner in nitrogen-containing atmospheres, resulting in more rapid degradation than in Ar+20%O<sub>2</sub>. Additionally, chamfering and welding do not significantly influence the oxidation behavior of Zry-3, but accelerated oxidation was observed at the chamfers and weld regions in Zry-4.

A thicker oxide layer was measured at the weld of Zr-1Nb ( $\approx 70\%$ ); however, it had the slowest oxidation kinetics in each experiment. Excessive cracking of the oxide was not noticed during the transient oxidation experiments and the transient oxidation behavior was similar to what was seen during isothermal oxidation experiments for each alloy. Raman spectroscopy identified a tetragonal-rich oxide layer at the metal/oxide interface of both Zry-3 and Zry-4 before and after breakaway, which has also been observed in literature [10]. The thickness of the layer decreased after breakaway, indicating that the tetragonal to monoclinic transformation occurred during further oxidation.

The work presented in this thesis was done as part of a larger project focused on the conversion from a highly enriched uranium (HEU) to low enriched uranium (LEU) fuel of the Transient Reactor Test (TREAT) facility at the Idaho National Laboratory (INL). The purpose of the project was to directly compare the oxidation behavior of Zry-3, Zry-4, and Zr-1Nb in TREAT's unique conditions with the goal of determining which alloy could replace the legacy Zry-3 fuel cladding currently being used, as it is no longer commercially available. The research in the following chapters helps fill a knowledge gap currently present in literature, as the oxidation behavior of zirconium alloys is not well studied in these extreme environments. It is becoming increasingly important to understand the behavior of cladding material in transient conditions with the development of research reactors that simulate accident type scenarios.

## **1.1 Motivation**

Zirconium alloys are typically used in as nuclear fuel cladding in water reactors due to their good corrosion resistance, mechanical properties, and low absorption cross section of thermal neutrons [11]. Although the corrosion resistance of zirconium alloys is favorable

in water at normal operating temperatures (250-350 °C), during transient or accident conditions the cladding may be exposed to air at high temperatures. It has been well documented that the oxidation rate increases drastically with temperature and the oxidation kinetics undergo a transition from parabolic to linear, after which the oxide cracks and becomes non-protective [1,4,12,13]. The transition from parabolic to faster kinetics is termed “breakaway.” Additionally, it has been shown that the oxidation reaction is catalyzed by the addition of nitrogen to the oxidizing atmosphere, such as in air [1–7]. The effect of nitrogen on the oxidation behavior of zirconium alloys will be discussed further in the next section. Finally, the oxidation behavior of zirconium alloys is dependent on the concentration of alloying elements, microstructure, and processing history [10,14–20]. The effect of all of these conditions must be considered when designing nuclear fuel cladding material and will be studied in this work.

The United States Department of Energy has a concerted effort to convert TREAT’s fuel from HEU to LEU [21]. One challenge of the conversion is that the Zircaloy-3 cladding currently being used is no longer commercially available; therefore, a new zirconium alloy cladding material must be identified. TREAT is a research reactor designed to simulate transient conditions ranging from mild upsets to severe accidents. TREAT can produce rapid power transients up to 600 °C in less than 1 second with a design basis accident temperature of 820 °C. The core is cooled by high velocity (28 mph) air that pulled from the environment outside the reactor. The maximum core temperature is limited by the oxidation rate of the zirconium cladding, which has been shown to increase in the presence of nitrogen (i.e. air) [22]. Additionally, TREAT’s cladding has a unique geometry; it is a rectangular prism with chamfers and welds (Figure 1.1). In order to determine which

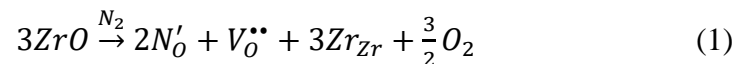
zirconium alloy will have the most favorable properties in TREAT's core, the effects of nitrogen in the oxidizing atmosphere, temperature, heating rate, welding, and plastic deformation on the oxidation behavior must be evaluated.



**Figure 1.1: Rendering of the fuel cladding assembly to be used in the TREAT facility.**

## 1.2 Oxidation of Zirconium Alloys in Air

Compared to oxidation in water or steam, the oxidation of zirconium alloys in air results in faster oxidation kinetics and the formation of non-protective oxide [1–7]. This increased degradation is thought to be due to the nitridation and re-oxidation of the zirconium oxide [6,8,9]. Additionally, zirconium is known to have a high solubility of oxygen (30 at.%) and oxidizes via inward diffusion of oxygen anions through the oxide, likely along the crystallite boundaries [11,23]. During oxidation in air, it has been proposed by Steinbrück et al. that nitrogen first reacts with the oxygen-stabilized  $\alpha$ -Zr(O) to form ZrN at the metal/oxide interface, creating oxygen vacancies via equation (1) [6].



As the oxidation reaction continues, the ZrN oxidizes in a rapid exothermic reaction to form ZrO<sub>2</sub>, which results in a volume expansion (approximately 49%), and is thought to be the cause of the porous oxide and crack formation [6,8,9]. The effect of nitrogen in the oxidizing atmosphere on the behavior of Zr, Zry-3, Zry-4, Zr-1Nb, and Zr-2.5Nb is discussed further in Chapter Two.

### 1.3 Effect of Alloying Elements on Oxidation Behavior

The alloying constituents and amount of those constituents added into the matrix drastically changes the oxidation behavior of zirconium alloys. Zirconium is typically alloyed with iron, tin, chromium, and niobium. Tin is soluble in zirconium up to 8% at 982 °C and goes into solution via substitution in the matrix [24]. It was originally added to zirconium to improve its corrosion resistance in the presence of nitrogen [11]. Iron and chromium form precipitates in the room temperature phase of zirconium but are soluble in the  $\beta$ -Zr phase [25,26]. Iron and chromium have been shown to improve the uniform and localized corrosion resistance in LWR conditions [11]. Although the elements can improve the properties of zirconium in certain conditions, they can also be detrimental to its oxidation behavior in specific scenarios. Proof et al. found that iron precipitates in contact with the surface of the alloy act as nucleation sites for oxidation [14,15]. Additionally, chromium precipitates in the oxide exhibit delayed oxidation. Chromium-rich precipitates ( $\text{Cr}_2\text{O}_3$ ) have a higher Pilling-Bedworth ratio than  $\text{ZrO}_2$  and cause cracking in the oxide during oxidation [16]. Tin has been found to stabilize the tetragonal zirconia phase [20]. During the oxidation of zirconium, tetragonal zirconia is formed before being transformed to the more stable monoclinic phase via a martensitic transformation [27]. The tetragonal to monoclinic phase transformation has been shown to result in cracking of the oxide due to volume expansion [10,20]. Finally, the addition of niobium has been shown to stabilize the tetragonal zirconia phase during oxidation, which results in increased resistance to breakaway [20]. However, at high concentrations of niobium (15-20%) the zirconium matrix becomes supersaturated with niobium and large  $\beta$ -Nb precipitates formed, resulting in a faster corrosion rate [19]. From the studies discussed above, it is clear that the oxidation

behavior is dependent on the alloying composition, concentration, and precipitation of secondary phases, which can be altered during fabrication processes. Section 1.4 will review how welding alters microstructure and SPP distribution in zirconium alloys.

#### 1.4 Welding of Zirconium Alloys

Among other parameters such as oxidizing atmosphere, temperature, and impurities, the oxidation behavior of zirconium alloys is also dependent on the microstructure and secondary phases present in the base metal [28–30]. Fabrication processes such as welding alter the microstructure of zirconium alloys in a variety of ways depending on the alloying elements, the weld type, and the parameters used during welding. It has been shown in literature and in Chapter Three that welding zirconium alloys typically results in three distinct regions with different microstructures (shown in Figure 1.2): the fusion zone (FZ) exists where the metal has experienced temperatures above the melting temperature, the heat affected zone (HAZ) is the region between the FZ and the bulk metal, where the metal has experienced temperatures that result in microstructural changes [31], and the third region is the base metal that is unaffected by welding. The grains are typically coarser in regions that experience higher temperatures [29].

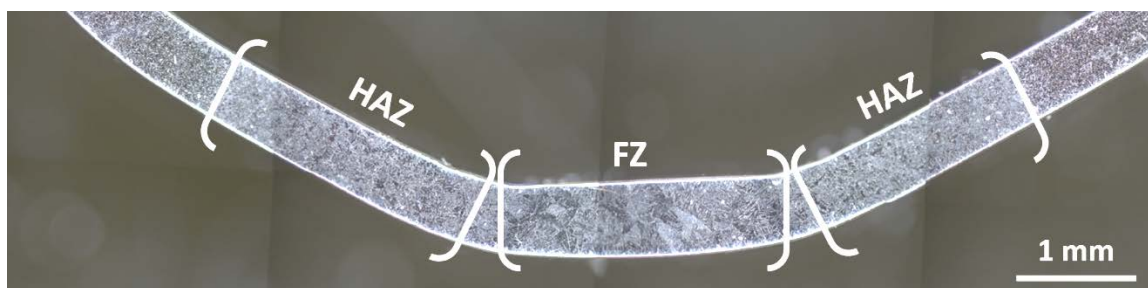


**Figure 1.2: Microstructure of an electron-beam welded zirconium alloy.**

Welding can affect the microstructure of the zirconium alloys in different ways. The high temperature can cause a structural phase transformation in the base metal;

zirconium undergoes an  $\alpha \rightarrow \beta$  transformation from hexagonal close-packed (HCP) to body-centered cubic (BCC) at 863 °C. Welding can also cause dissolution of secondary phase precipitates (SPPs) in the FZ and HAZ. Additionally, the shape of the weld can result in stress in the base metal during oxidation, which can lead to cracking of the oxide [32]. The effect of these microstructural changes is discussed in Chapter Three.

The work presented in the following chapters will characterize the effect of the previously mentioned parameters: nitrogen in the oxidizing atmosphere, plastic deformation (chamfering), welding and weld type, and alloying elements. The next chapter will present and compare the isothermal oxidation behavior of pure Zr, Zry-3, Zry-4, Zr-1Nb, and Zr-2.5Nb in Ar+20% O<sub>2</sub> and N<sub>2</sub>+20% O<sub>2</sub>.

### 1.5 References

- [1] C. Duriez, D. Drouan, G. Pouzadoux, Reaction in air and in nitrogen of pre-oxidised Zircaloy-4 and M5<sup>TM</sup> claddings, *J. Nucl. Mater.* 441 (2013) 84–95. doi:10.1016/j.jnucmat.2013.04.095.
- [2] C. Duriez, T. Dupont, B. Schmet, F. Enoch, Zircaloy-4 and M5<sup>®</sup> high temperature oxidation and nitriding in air, *J. Nucl. Mater.* 380 (2008) 30–45. doi:10.1016/j.jnucmat.2008.07.002.
- [3] M. Lasserre, V. Peres, M. Pijolat, O. Coindreau, C. Duriez, J.P. Mardon, Qualitative analysis of Zircaloy-4 cladding air degradation in O<sub>2</sub>-N<sub>2</sub> mixtures at high temperature, *Mater. Corros.* 65 (2014) 250–259.
- [4] M. Steinbrück, M. Böttcher, Air oxidation of Zircaloy-4, M5<sup>®</sup> and ZIRLO<sup>TM</sup> cladding alloys at high temperatures, *J. Nucl. Mater.* 414 (2011) 276–285. doi:10.1016/j.jnucmat.2011.04.012.
- [5] M. Steinbrück, Prototypical experiments relating to air oxidation of Zircaloy-4 at high temperatures, *J. Nucl. Mater.* 392 (2009) 531–544. doi:10.1016/j.jnucmat.2009.04.018.

- [6] M. Steinbrück, S. Schaffer, High-temperature oxidation of Zircaloy-4 in oxygen-nitrogen mixtures, *Oxid. Met.* 85 (2016) 245–262. doi:10.1007/s11085-015-9572-1.
- [7] E.T. Hayes, A.H. Roberson, Some effects of heating zirconium in air, oxygen, and nitrogen, *J. Electrochem. Soc.* 96 (1949) 142–151.
- [8] E. Beuzet, J.S. Lamy, A. Bretault, E. Simoni, Modelling of Zry-4 cladding oxidation by air, under severe accident conditions using the MAAP4 code, *Nucl. Eng. Des.* 241 (2011) 1217–1224. doi:10.1016/j.nucengdes.2010.04.024.
- [9] J. Stuckert, Z. Hózer, A. Kiselev, M. Steinbrück, Cladding oxidation during air ingress. Part I: Experiments on air ingress, *Ann. Nucl. Energy.* 93 (2016) 4–17. doi:10.1016/j.anucene.2015.12.034.
- [10] J. Wei, P. Frankel, E. Polatidis, M. Blat, A. Ambard, R.J. Comstock, The effect of Sn on autoclave corrosion performance and corrosion mechanisms in Zr – Sn – Nb alloys, *Acta Mater.* 61 (2013) 4200–4214.
- [11] B. Cox, V.G. Kristsky, C. Lemaignan, V. Polley, I.G. Ritchie, H. Ruhmann, V.N. Shishov, *Waterside corrosion of zirconium alloys in nuclear power plants*, Vienna, Austria, 1998.
- [12] H.H. Kim, J.H. Kim, J.Y. Moon, H.S. Lee, J.J. Kim, High-temperature oxidation behavior of Zircaloy-4 and Zirlo in steam ambient, *J. Mater. Sci. Technol.* 26 (2010) 827–832.
- [13] Y. Ishii, J.M. Sykes, Microstructure of oxide layers formed on Zircaloy-2 in air at 450 °C, *Mater. High Temp.* 17 (2014) 23–28. doi:10.1179/mht.2000.005.
- [14] C. Proff, S. Abolhassani, M.M. Dadras, C. Lemaignan, In situ oxidation of zirconium binary alloys by environmental SEM and analysis by AFM, FIB, and TEM, *J. Nucl. Mater.* 404 (2010) 97–108. doi:10.1016/j.jnucmat.2010.05.012.
- [15] C. Proff, S. Abolhassani, C. Lemaignan, Oxidation behaviour of binary zirconium alloys containing intermetallic precipitates, *J. Nucl. Mater.* 416 (2011) 125–134. doi:10.1016/j.jnucmat.2010.11.099.

- [16] C. Proff, S. Abolhassani, C. Lemaignan, Oxidation behaviour of zirconium alloys and their precipitates – A mechanistic study, *J. Nucl. Mater.* 432 (2013) 222–238. doi:10.1016/j.jnucmat.2012.06.026.
- [17] A. Yilmazbayhan, E. Breval, A.T. Motta, R.J. Comstock, Transmission electron microscopy examination of oxide layers formed on Zr alloys, *J. Nucl. Mater.* 349 (2006) 265–281. doi:10.1016/j.jnucmat.2005.10.012.
- [18] Y. Dong, A.T. Motta, E. a. Marquis, Atom probe tomography study of alloying element distributions in Zr alloys and their oxides, *J. Nucl. Mater.* 442 (2013) 270–281. doi:10.1016/j.jnucmat.2013.08.055.
- [19] K.N. Choo, Y.H. Kang, S.I. Pyun, V.F. Urbanic, Effect of composition and heat treatment on the microstructure and corrosion behavior of Zr-Nb alloys, *J. Nucl. Mater.* 209 (1994) 226–235. doi:10.1111/cpr.12282.
- [20] J.H. Baek, Y.H. Jeong, Breakaway phenomenon of Zr-based alloys during a high-temperature oxidation, *J. Nucl. Mater.* 372 (2008) 152–159. doi:10.1016/j.jnucmat.2007.02.011.
- [21] D. Diamond, Review of the TREAT Conversion Conceptual Design and Fuel Qualification Plan, Rep. BNL-114531-2017-FORE. (2017).
- [22] J. Carmack, Future transient testing of advanced fuels testing workshop, Rep. INL/EXT-09-16392. (2009).
- [23] P.Y. Chevalier, E. Fischer, B. Cheynet, Progress in the thermodynamic modelling of the O-U-Zr ternary system, *Comput. Coupling Phase Diagrams Thermochem.* 28 (2004) 15–40.
- [24] J.P. Abriata, J.C. Bolcich, D. Arias, Sn-Zr (Tin-Zirconium), *Bin. Alloy Phase Diagrams.* (1990) 3416–3419.
- [25] K. Zeng, M. Hämmäläinen, R. Luoma, A thermodynamic assessment of the Cr-Zr system, *Zeitschrift Für Met.* 84 (1993) 23–28.

- [26] F. Stein, G. Sauthoff, M. Palm, Experimental determination of intermetallic phases, phase equilibria, and invariant reaction temperatures in the Fe-Zr system, *J. Phase Equilibria*. 23 (2002) 480–494.
- [27] W. Gong, H. Zhang, Y. Qiao, H. Tian, X. Ni, Z. Li, X. Wang, Grain morphology and crystal structure of pre-transition oxides formed on Zircaloy-4, *Corros. Sci.* 74 (2013) 323–331. doi:10.1016/j.corsci.2013.05.007.
- [28] Y.H. Jeong, K. Ok, H.G. Kim, H.G. Jeong, Y. H., Lee, K. O., Kim, Y.H. Jeong, K. Ok, H.G. Kim, Correlation between microstructure and corrosion behavior of Zr – Nb binary alloy, *J. Nucl. Mater.* 302 (2002) 9–19. doi:10.1016/S0022-3115(02)00703-1.
- [29] C. Cai, L. Li, W. Tao, G. Peng, X. Wang, Weld bead size, microstructure and corrosion behavior of zirconium alloys joints welded by pulsed laser spot welding, *J. Mater. Eng. Perform.* 25 (2016) 3783–3792. doi:10.1007/s11665-016-2250-x.
- [30] K.Y. Huang, The effect of heat treatment on the microstructure and the corrosion resistance of Zircaloy-4 in 450 °C steam, *J. Nucl. Mater.* 136 (1985) 16–29.
- [31] P. Rudling, A. Strasser, F. Garzarolli, *Welding of Zirconium Alloys*, 2007.
- [32] C. Cai, W. Tao, L. Li, Y. Chen, Weld bead formation and corrosion behavior of pulsed laser welded zirconium alloy, *Int. J. Adv. Manuf. Technol.* 77 (2015) 621–628. doi:10.1007/s00170-014-6474-3.

CHAPTER TWO: OXIDATION BEHAVIOR OF ZIRCONIUM, ZIRCALOY-3,  
ZIRCALOY-4, ZR-1NB, AND ZR-2.5NB IN AIR AND OXYGEN

This chapter has been published in Nuclear Materials and Energy.

Reference:

J.L. Vandegrift, P.M. Price, J.P. Stroud, C.J. Parga, I.J. Van Rooyen, B.J. Jaques and D.P. Butt, "Oxidation Behavior of Zirconium, Zircaloy-3, Zircaloy-4, Zr-1Nb, and Zr-2.5Nb in Air and Oxygen" *Nuclear Materials and Energy*. (2019).

doi:10.1016/j.nme.2019.100692.

## **Oxidation Behavior of Zirconium, Zircaloy-3, Zircaloy-4, Zr-1Nb, and Zr-2.5Nb in Air and Oxygen**

Jordan L. Vandegrift<sup>1,2</sup>

Patrick M. Price<sup>1,2,3</sup>

John-Paul Stroud<sup>1,2</sup>

Clemente J. Parga<sup>4</sup>

Isabella J. Van Rooyen<sup>4</sup>

Brian J. Jaques<sup>1,2</sup>

Darryl P. Butt<sup>1,2,5</sup>

1. *Boise State University, 1910 University Dr., Boise, ID 83725*
2. *Center for Advanced Energy Studies, 995 University Blvd., Idaho Falls, ID 83401*
3. *Sandia National Laboratory, 1515 Eubank Blvd. SE, Albuquerque, NM 87123*
4. *Idaho National Laboratory, 2525 Fremont Ave, Idaho Falls, ID 83402*
5. *University of Utah, 201 Presidents Cir, Salt Lake City, UT 84112*

### **2.1 Abstract**

The Transient Reactor Test (TREAT) facility at the Idaho National Laboratory currently utilizes a legacy Zircaloy-3 cladding, which is no longer commercially available. TREAT is air cooled and routinely operates at temperatures well above that of traditional reactor designs. This study investigates the oxidation behavior of pure zirconium and its alloys (Zircaloy-3, Zircaloy-4, Zr-1Nb, Zr-2.5Nb) in Ar+20%O<sub>2</sub> and N<sub>2</sub>+20%O<sub>2</sub> atmospheres at temperatures ranging from 400-800 °C to determine which alloy should be

implemented as TREAT's cladding. While the oxidation behavior of zirconium based cladding materials has been extensively documented, this study focuses on direct comparison between legacy Zircaloy-3 and contemporary alloys using a flat plate geometry and similar conditions seen at the TREAT facility. In this work, thermogravimetric analysis was used to measure both steady state and breakaway oxidation, which was then used to calculate oxidation rate constants and activation energies of each material. Oxide thickness was evaluated through microscopy of oxidized specimen cross sections. The Zircaloy-3 and Zr-1Nb alloys were found to be the most resistant to oxidation under the conditions of this study, whereas the Zr-2.5Nb alloy was found to be the most susceptible.

## **2.2 Introduction**

The Transient Reactor Test (TREAT) facility, located at the Idaho National Laboratory (INL), is designed to provide safety data on various fuel designs during simulated transients varying between mild upsets to severe accidents. TREAT was decommissioned in 1994; however, it was reinstated to operational status in November of 2017. The core is being converted from a highly enriched uranium (HEU) core to a low enriched uranium (LEU) core, thus the structural materials used in the original core are being re-evaluated. TREAT's maximum operating temperature is limited by the rapid oxidation of the zirconium alloy cladding at high temperatures in air [1]. Due to this restriction, TREAT is designed such that the fuel core (including the zircaloy cladding) does not exceed a maximum temperature of 600 °C in normal transients with a design basis accident limit of 820 °C. Additionally, TREAT is air cooled. Nitrogen present in air has been shown by previous work to act as a catalyst for the oxidation reaction, resulting in faster oxidation kinetics and the formation of a more porous oxide when compared to

oxidation in pure oxygen or steam [2-8]. Once the oxide reaches a critical thickness it cracks, creating a direct pathway for oxygen to reach the metal surface resulting in a transition from parabolic to faster oxidation kinetics [9]. This transition is termed “breakaway”. The resulting oxide is porous and cracked, compromising the mechanical stability of the cladding.

It is fairly well documented that the pre-breakaway regime during zircaloy oxidation is a diffusion limited process (controlled by the diffusion of oxygen anions) during which a dense oxide layer is formed [10-13]. The post-breakaway regime is controlled by the nucleation and growth of nodules at the metal/oxide interface. In the breakaway regime during corrosion in air, it is thought that three reactions take place: 1) Cracks begin to form in the dense  $ZrO_2$  layer and  $ZrN$  and  $ZrO_2$  form at the metal oxide interface, 2)  $ZrN$  is oxidized and the volume change results in cracks in  $ZrO_2$ , 3) nitrogen can become trapped between  $ZrO_2$  and  $\alpha$ - $Zr(O)$  and form  $ZrN$ , which is then oxidized resulting in further cracking and oxidation [10,11,13].

While some research has been reported on the characterization of the oxidation behavior of zirconium alloys under similar conditions, no publications were found that directly compare  $Zry-3$ ,  $Zry-4$ ,  $Zr-1Nb$ ,  $Zr-2.5Nb$ , and  $Zr$  with similar geometry under similar conditions in the temperature range of interest to TREAT (400-800 °C). Duriez *et al.* provides direct comparisons of oxidized  $Zry-4$  and  $M5^{\text{®}}$  tube samples in air at temperatures between 600-1200 °C [2,3,14]. Their results conclude that the oxidation kinetics in  $Zry-4$  are faster than in  $M5^{\text{®}}$  both before and after breakaway oxidation when tested under the same experimental conditions with similar sample geometries. Steinbrück *et al.* investigated isothermal and non-isothermal oxidation of  $Zry-4$  tubes in oxygen, air,

and nitrogen from 800-1480 °C using thermogravimetric analysis (TGA) [6]. They found that Zry-4 tubes exhibit faster oxidation kinetics in air than in pure oxygen or nitrogen. Additionally, breakaway occurred earlier in samples oxidized in air and the resulting oxide was more porous. The authors attribute the increased oxidation behavior to the formation and subsequent re-oxidation of ZrN.

The work demonstrated here provides a direct comparison of the oxidation behavior of Zry-3, Zry-4, Zr-1Nb, Zr-2.5Nb, and pure zirconium with similar geometry and experimental conditions which will bridge discrepancies present in current literature. The results from the separate effects testing provide insight into the effect of nitrogen on the oxidation behavior of these zirconium-based alloys. The onset of breakaway oxidation and kinetics before and after breakaway are determined and the performance of the cladding materials is compared.

## **2.3 Experimental Procedures**

### **2.3.1 Specimens**

The composition of the zirconium alloys used are shown below in Table 2.1. Additionally, scanning electron microscope (SEM) images of the microstructure of the as received materials are shown in Figure 2.1. The Fe-rich precipitates found in Zry-3 are seen in the figure, however no precipitates were found in the other materials. The impurities present in the pure Zr are listed by the vendor (Goodfellow) in parts per million by mass as: Hf-(2500), O-(1000), C-(250), Fe-(200), Cr-(200), N-(100), H-(10). The materials were received in sheets of varying thickness (T) as listed in Table 2.1. The thickness of the pure Zr was 0.5 mm. Prior to oxidation, samples were machined from the sheets using electronic discharge machining (EDM). Zry-3, Zry-4, Zr-1Nb, and Zr had the dimensions 10.1 x 7.5

mm and Zr-2.5Nb had the dimensions 9.3 x 4.4 mm (due to the size of the original sheet of material received). Before oxidation experiments, the native oxide present on the samples was removed on all six surfaces by grinding with 800 and 1200 grit SiC paper. The samples were then sonicated in a 1:1:1 solution of acetone:ethanol:DI water and dried before loading into the simultaneous thermal analyzer (STA).

**Table 2.1: Composition (wt %) of zirconium alloys presented here.**

	Sn	Fe	Cr	O	Nb	H x W x T (mm)
<b>Zry-3</b>	0.25	0.25	-	-	-	10.1 x 7.5 x 0.63
<b>Zry-4</b>	1.2-1.7	0.18-0.24	0.07-0.13	0.1-0.14	-	10.1 x 7.5 x 1.62
<b>Zr-1Nb</b>	-	0.015-0.06	-	0.09-0.12	1	10.1 x 7.5 x 0.36
<b>Zr-2.5Nb</b>	-	0.061	-	0.11	2.62	9.3 x 4.4 x 1.49

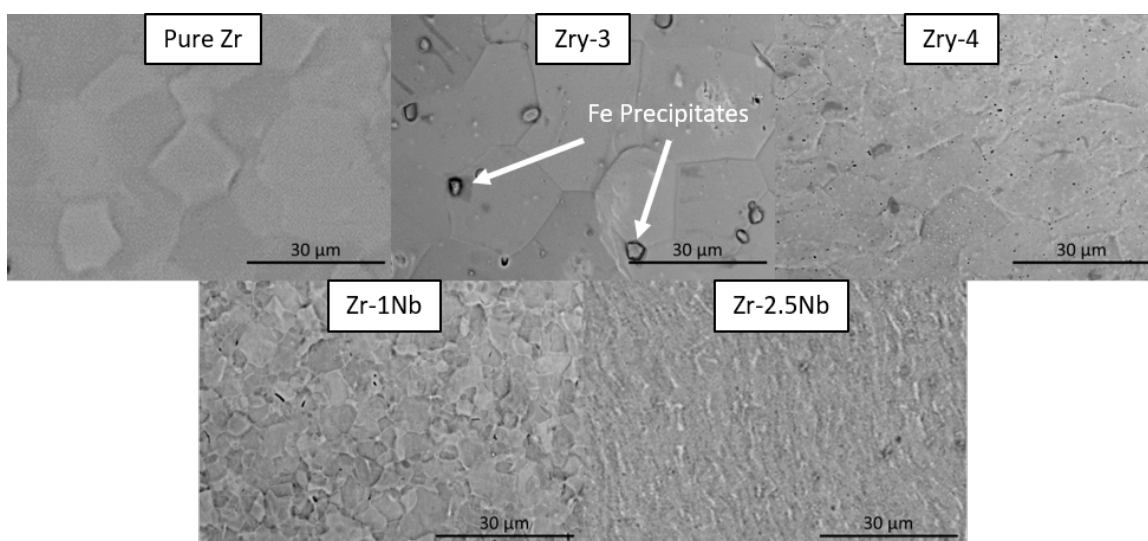


**Figure 2.1: Backscatter SEM images of the as received microstructure of the materials investigated.**

### 2.3.2 Oxidation Experiments

All oxidation experiments were performed in a NETZSCH STA-449 F3 Jupiter with thermogravimetric analysis (TGA). The 20-hour isothermal and non-isothermal experiments were completed in two different oxidizing atmospheres: 80% N<sub>2</sub>+O<sub>2</sub> (air) or 80% Ar+O<sub>2</sub> (oxygen). A custom notched alumina crucible was used to hold the plate

sample upright in the furnace, maximizing the surface exposed to the experimental gas while minimizing the contact between the sample and the crucible, as shown in Figure 2.2.

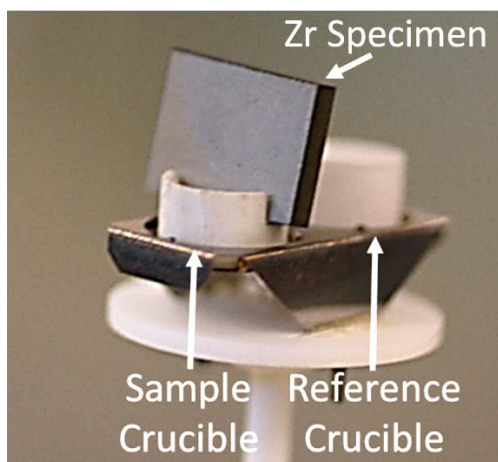


**Figure 2.2:** Image showing the custom sample setup for the TGA. The platinum sample carrier is loaded with a notched alumina crucible to minimize contact between the sample and crucible while maximizing the surface area exposed to the oxidizing gas.

During the non-isothermal oxidation experiments, specimens were individually heated to 940 °C at a rate of 20 °C/min, held for 10 minutes to allow the temperature to equilibrate, and cooled back down to room temperature at 20 °C/min.

The 20-hour isothermal oxidation measurements were collected at temperatures ranging from 400-800 °C. Specimens were individually heated to the temperature of interest at 20 °C/min with 100 mL/min of ultra-high purity (UHP) argon cleaned with a thermal oxygen getter (OG). After reaching the setpoint temperature the oxidizing gas (either air or oxygen) flowed at 100 mL/min for 20 hours. The specimen was then cooled to room temperature in 100 mL/min of UHP-OG argon at 20 °C/min.

### 2.3.3 Post Test Characterization

After oxidation, macro images were taken of each sample. The samples were then sectioned with a slow speed saw, mounted in epoxy, polished to 1 μm in a diamond slurry,

and imaged with optical microscopy. The cross section of each sample was used to measure oxide thickness every 100  $\mu\text{m}$ , resulting in approximately 80 measurements per sample, which were used to calculate average oxide thickness and associated standard deviation.

To quantify the onset of the breakaway transition, tangent lines were fit to the mass gain data before and after the transition from parabolic to linear kinetics. The intersection of the two lines was considered the breakaway time at each temperature. The mass gain data was normalized to the initial sample surface area and used to assess the oxidation kinetics and determine the activation energy of each sample before and after breakaway.

## **2.4 Results**

### **2.4.1 Oxidation Behavior**

The results of the normalized non-isothermal thermogravimetric data are summarized in Figure 2.3. Experiments done in pure nitrogen resulted in minimal mass gain consistent with the findings of Steinbrück *et al.* [6]. Samples heated in oxidizing conditions start experiencing rapid mass gain between 500-700 °C. It is interesting to note that the zirconium alloys with Sn and Fe (Zry-3, Zry-4) oxidize much faster in air than in oxygen, whereas this dependence on atmosphere is much less pronounced in pure Zr and zirconium alloys with Nb (Zr-1Nb, Zr-2.5Nb).

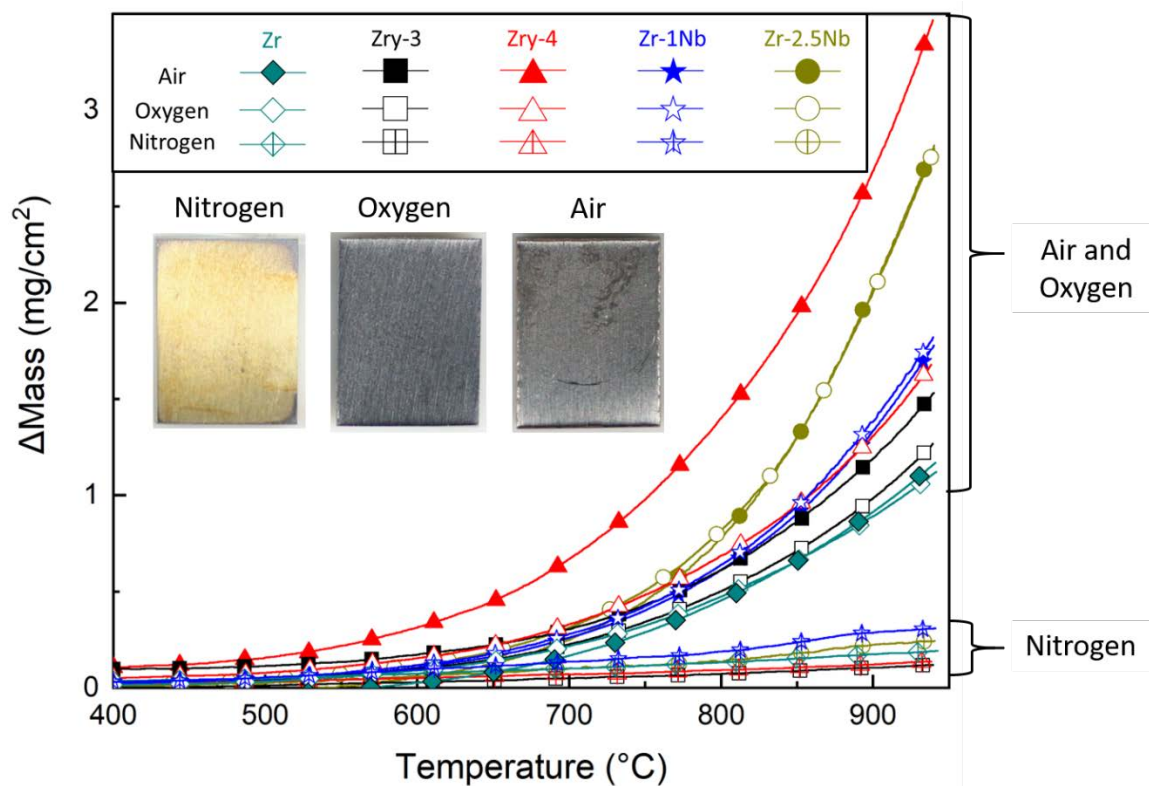


**Figure 2.3:** Non-isothermal mass gain of pure Zr, Zry-3, Zry-4, Zr-1Nb, and Zr-2.5Nb in synthetic air, oxygen, and nitrogen. Samples were heated to 940  $^{\circ}\text{C}$  at 20  $^{\circ}\text{C}/\text{min}$ . Inset shows macro-images of the surface of the Zry-4 after non-isothermal oxidation.

The 20-hour isothermal (400-800  $^{\circ}\text{C}$ ) oxidation results are summarized in Figure 2.4. The y-axis scales vary to best display the data. All the zirconium alloys undergo breakaway during oxidation above 700  $^{\circ}\text{C}$ , whereas pure Zr experiences minimal oxidation up to 800  $^{\circ}\text{C}$ . The Zr-2.5Nb oxidizes the most readily of all the materials at 600 and 700  $^{\circ}\text{C}$  up to 20 hours. However at 800  $^{\circ}\text{C}$ , as seen in the inset of Figure 2.4, Zry-4 experiences breakaway almost immediately during oxidation in air which results in rapid oxidation. The difference between extent of oxidation in air and oxygen containing gases is minimal from 400-700  $^{\circ}\text{C}$  but increases dramatically at 800  $^{\circ}\text{C}$  for all alloys with largest deviations associated with the Sn and Fe based zirconium alloys, which is consistent with the non-isothermal behavior. In addition, Zr-1Nb and Zr-2.5Nb both begin to spall heavily during

oxidation at 800 °C in air. An important observation is that the accelerated corrosion effect of nitrogen containing air is most pronounced after breakaway for all materials tested in this study.

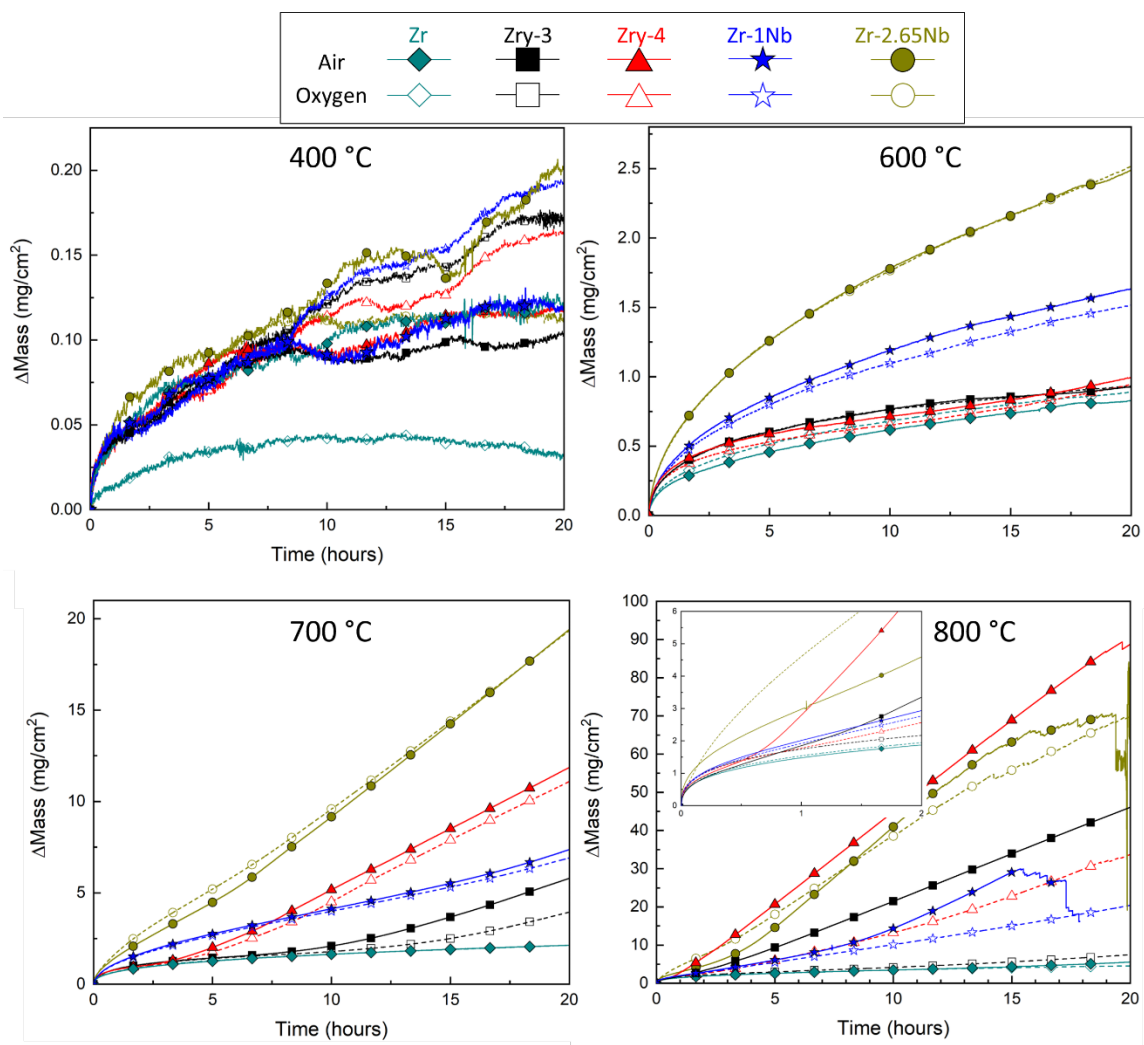


**Figure 2.4:** Normalized mass gain versus isothermal oxidation time of Zr, Zry-3, Zry-4, Zr-1Nb, and Zr-2.5Nb in air and oxygen at 400-800 °C. The inset in the 800 °C graph is the first two hours of the isothermal oxidation showing the onset of breakaway in Zry-3, Zry-4, and Zr-2.5Nb.

Macro images of specimens after 20-hour isothermal oxidation at 600, 700 and 800 °C are shown in Figure 2.5. Cross-section images of Zry-4 after isothermal oxidation at 600 and 800 °C in air and oxygen are presented in Figure 2.6 to show the change in the

oxide before and after the breakaway transition. From these images it is seen that before samples undergo breakaway ( $< 700\text{ }^{\circ}\text{C}$  for most alloys in this study), a dark and cohesive oxide is present. After breakaway, a thicker and non-protective oxide is present. In Zry-3 and Zry-4 the post-breakaway oxide has an orange color, while the post-breakaway oxide formed on the Nb alloys is primarily white (although a slight orange tint was observed on the corners and edges after  $800\text{ }^{\circ}\text{C}$  oxidation). The Sn-Fe based alloys develop post-breakaway oxide first on the corners and edges as well as isolated nodules on the surface of the samples. The Nb alloys form a network of horizontal cracks on the surface, inside of which the white post-breakaway oxide forms. The effect of nitrogen on the oxidation behavior of the zirconium alloys is seen most clearly after oxidation at  $800\text{ }^{\circ}\text{C}$ : oxidation in air results in a cracked oxide, while the oxide formed in oxygen remains comparatively cohesive. After oxidation at temperatures higher than  $600\text{ }^{\circ}\text{C}$ , Zr-1Nb becomes mechanically deformed; which is likely attributed to these samples being thinner than the other alloys. During oxidation at  $800\text{ }^{\circ}\text{C}$  in oxygen, Zr-1Nb becomes severely mechanically deformed and, in air, most of the sample has oxidized and spalled off. Additionally, an artifact of the positioning of the sample in the crucible is apparent in the Zr and Zry-3 specimens during oxidation at  $800\text{ }^{\circ}\text{C}$ , as seen in the upper right side of Figure 2.5 where an outline of the crucible is seen corresponding to reduced oxide growth.

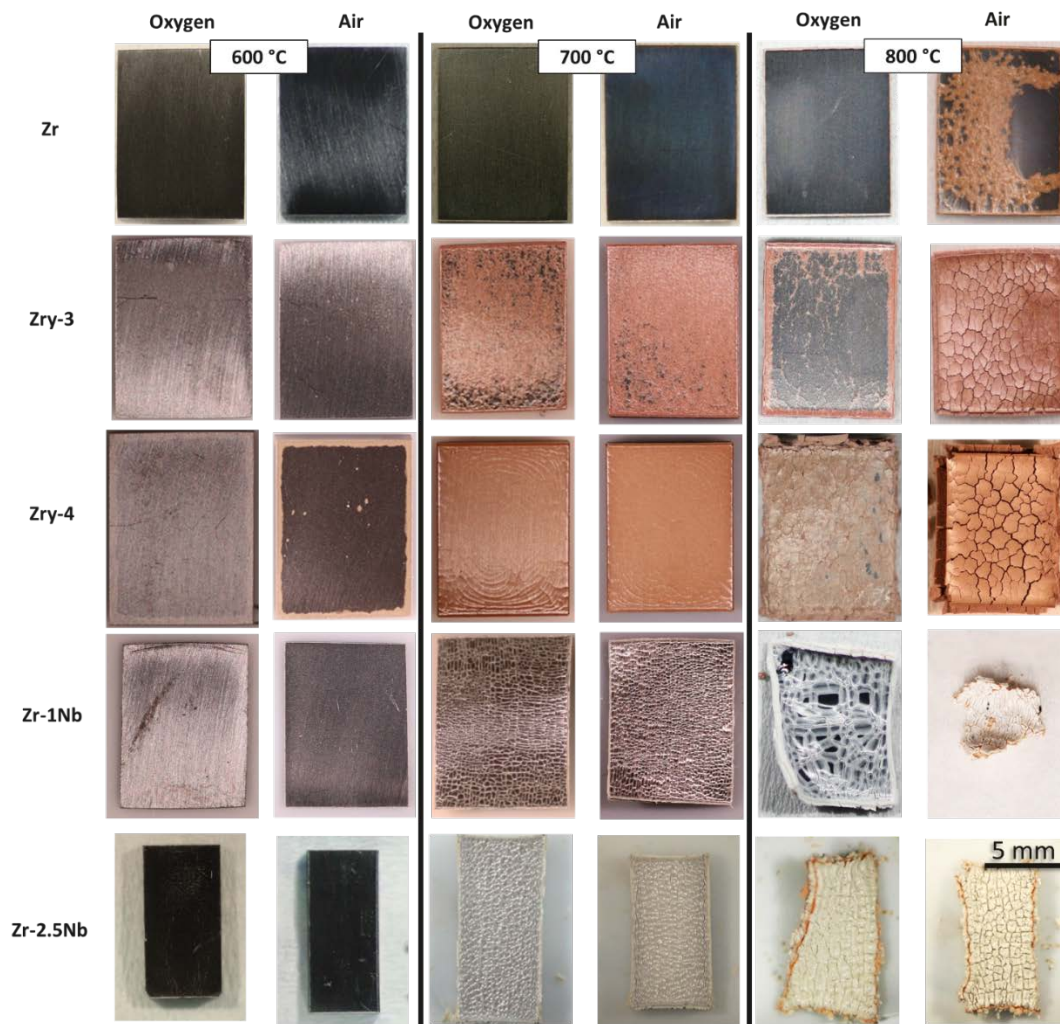


**Figure 2.5:** Macro images of the surface of each alloy showing the material degradation after 20-hour isothermal oxidation at 600, 700, and 800 °C in air and oxygen.

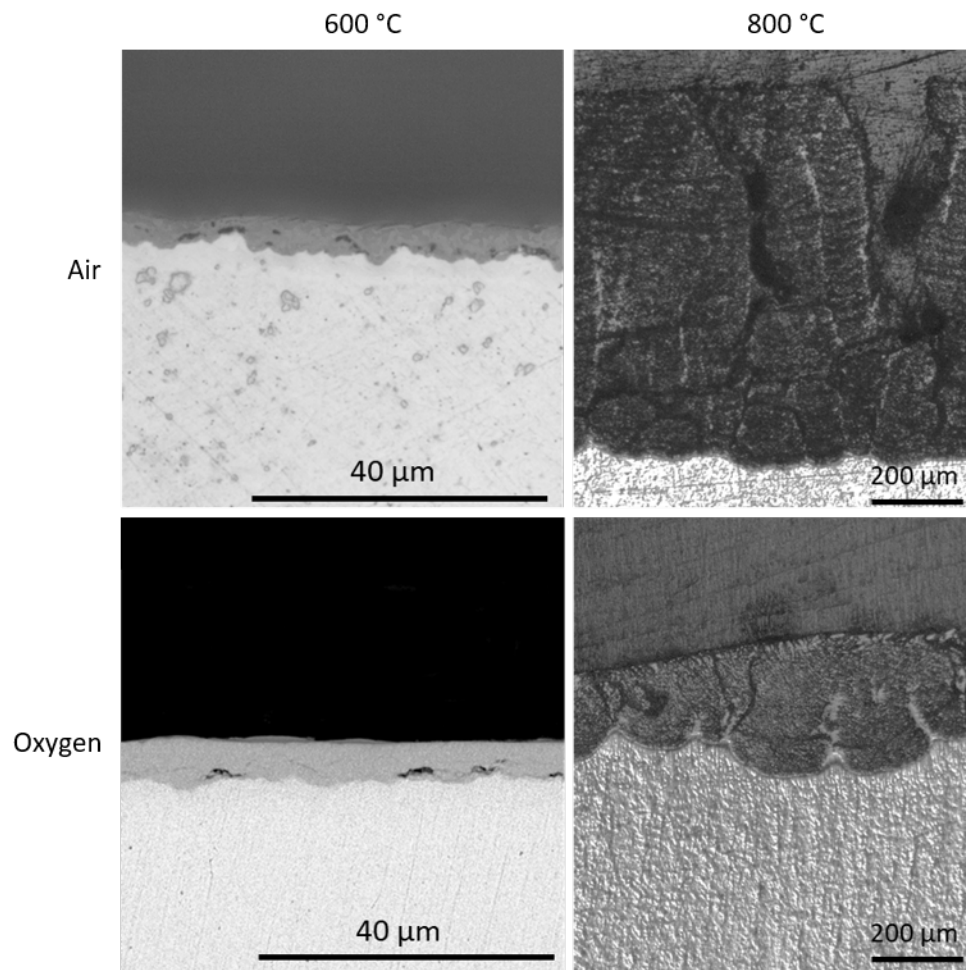


**Figure 2.6:** Representative sample cross-sections after oxidation. The specimen shown is Zry-4 after oxidation in air and oxygen at 600 °C and 800 °C.

The breakaway transition time and the oxide thickness of each alloy after 20 hours of isothermal oxidation are summarized in Table 2.2. As discussed with Figure 2.4, breakaway occurs more rapidly in samples oxidized in air compared to those oxidized in oxygen in all cases (except Zr-1Nb at 700 °C and Zr-2.5Nb at 800 °C where breakaway occurs only slightly sooner in oxygen). Additionally, as expected, the oxide formed in air is thicker than that formed in oxygen after breakaway (most notably for Zry-3, Zry-4, and Zr-1Nb). This is best illustrated in Figure 2.7, which shows oxide thickness versus isothermal oxidation temperature after 20 hours. The difference in oxide thickness between oxidation in air or oxygen continues to increase rapidly with increasing oxidation

temperature. However, it should be noted that the deviation associated with the oxide thickness measurements for samples that had reached breakaway was relatively high compared to those that had not reached breakaway due to the cracked nature of the oxide.

**Table 2.2: Time to breakaway determined from isothermal oxidation experiments (Figure 2.4) and oxide thickness of pure zirconium, Zry-3, Zry-4, Zr-1Nb, and Zr-2.5Nb after 20-hour isothermal oxidation in air and oxygen environments.**

Temp (°C)	Alloy	Air		Oxygen	
		Breakaway Onset (hours)	Oxide Thickness ± St. Dev. (µm)	Breakaway Onset (hours)	Oxide Thickness ± St. Dev. (µm)
600	Zr	-	4 ± 1	-	3 ± 1
	Zry-3	-	3 ± 1	-	4 ± 1
	Zry-4	16	4 ± 2	13.5	7 ± 3
	Zr-1Nb	-	8 ± 1	-	8 ± 1
	Zr-2.5Nb	-	17 ± 3	-	12 ± 2
700	Zr	-	10 ± 1	-	12 ± 1
	Zry-3	11.5	30 ± 10	15	20 ± 9
	Zry-4	4.5	80 ± 17	6	70 ± 17
	Zr-1Nb	16.5	30 ± 13	16	30 ± 13
	Zr-2.5Nb	6	105 ± 11	7	50 ± 7
800	Zr	-	60 ± 29	-	17 ± 1
	Zry-3	3	340 ± 28	14.5	30 ± 22
	Zry-4	1.5	790 ± 34	4	20 ± 6
	Zr-1Nb	9.5	190 ± 21	-	60 ± 24
	Zr-2.5Nb	4.5	340 ± 148	4	380 ± 41

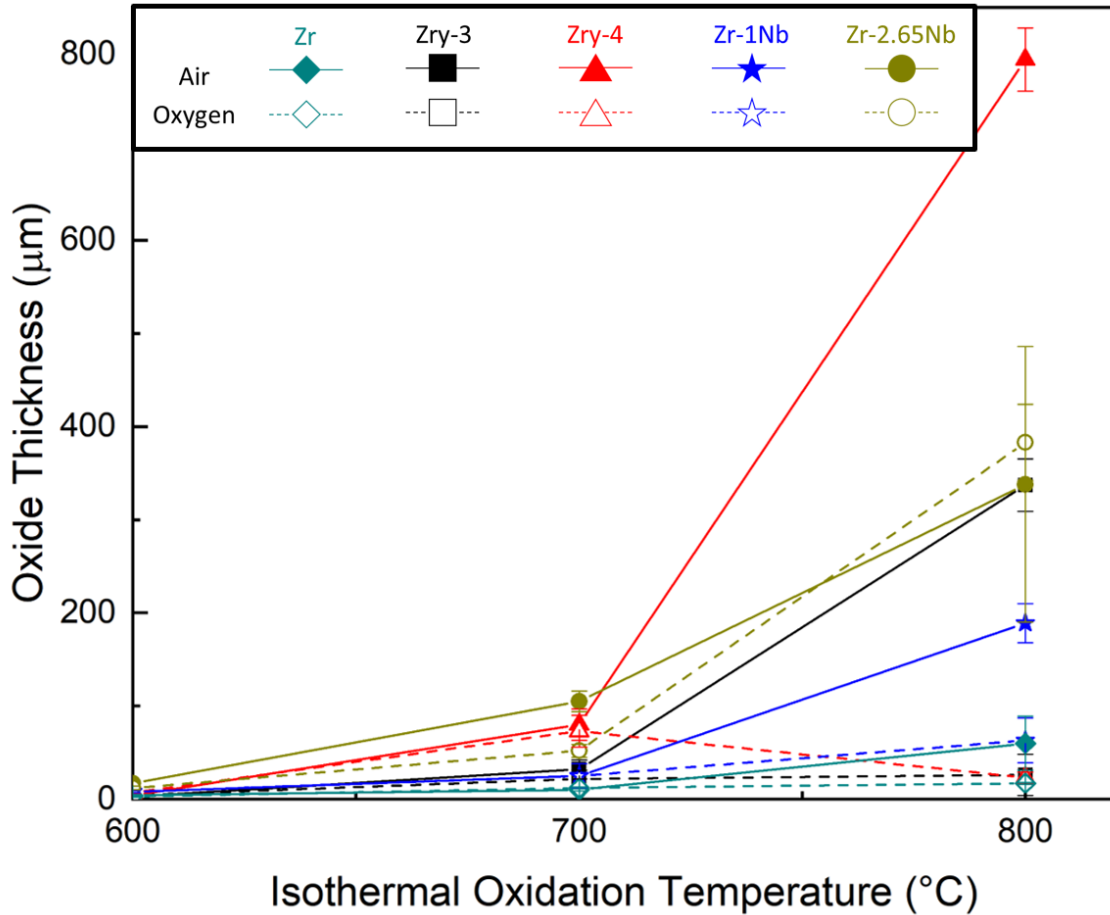


**Figure 2.7:** Average measured oxide thickness versus isothermal oxidation temperature in air and oxygen for all cladding materials. The error increases with increasing oxidation temperature due to the cracked nature of the oxide. The inset shows cross-section images of Zry-4 after 20 hours of isothermal oxidation at 800 °C.

## 2.5 Discussion

### 2.5.1 Oxidation Kinetics

The oxidation rate is related to the normalized mass gained during oxidation by the equation [12]:

$$W^n = K * t \left[ \frac{kg}{m^2} \right]^n \quad (1)$$

where  $W$  is the normalized mass gain,  $K$  is the oxidation rate constant,  $t$  is oxidation time, and  $n$  is the rate law identifier (i.e.  $n=1$  for linear  $n=2$  for parabolic oxidation behavior).

The oxidation rate constant is determined for each alloy and isothermal temperature by

fitting Equation 1 to the data in Figure 2.4. The pre- and post-breakaway rate constants were determined separately, with pre-breakaway following parabolic ( $n=2$ ) oxidation behavior and post-breakaway following linear ( $n=1$ ) oxidation behavior. The activation energy of each alloy before and after breakaway is then determined via an Arrhenius equation according to:

$$\ln(K) = \ln(A) + \left(\frac{1}{T}\right) \left(\frac{-E_a}{R}\right) \left[\frac{J}{mol}\right] \quad (2)$$

where  $A$  is a constant,  $E_a$  is the activation energy,  $R$  is the ideal gas constant, and  $T$  is the isothermal oxidation temperature. The  $\ln(K)$  values obtained from Equation 1 are plotted against  $1/T$  and are fit with a linear trend line. These plots before and after breakaway from oxidation in oxygen are shown in Figure 2.8 and the values found for Equation 2 are listed in Table 2.3. Activation energy before and after breakaway are obtained from the slopes of these plots and listed in Table 2.4.

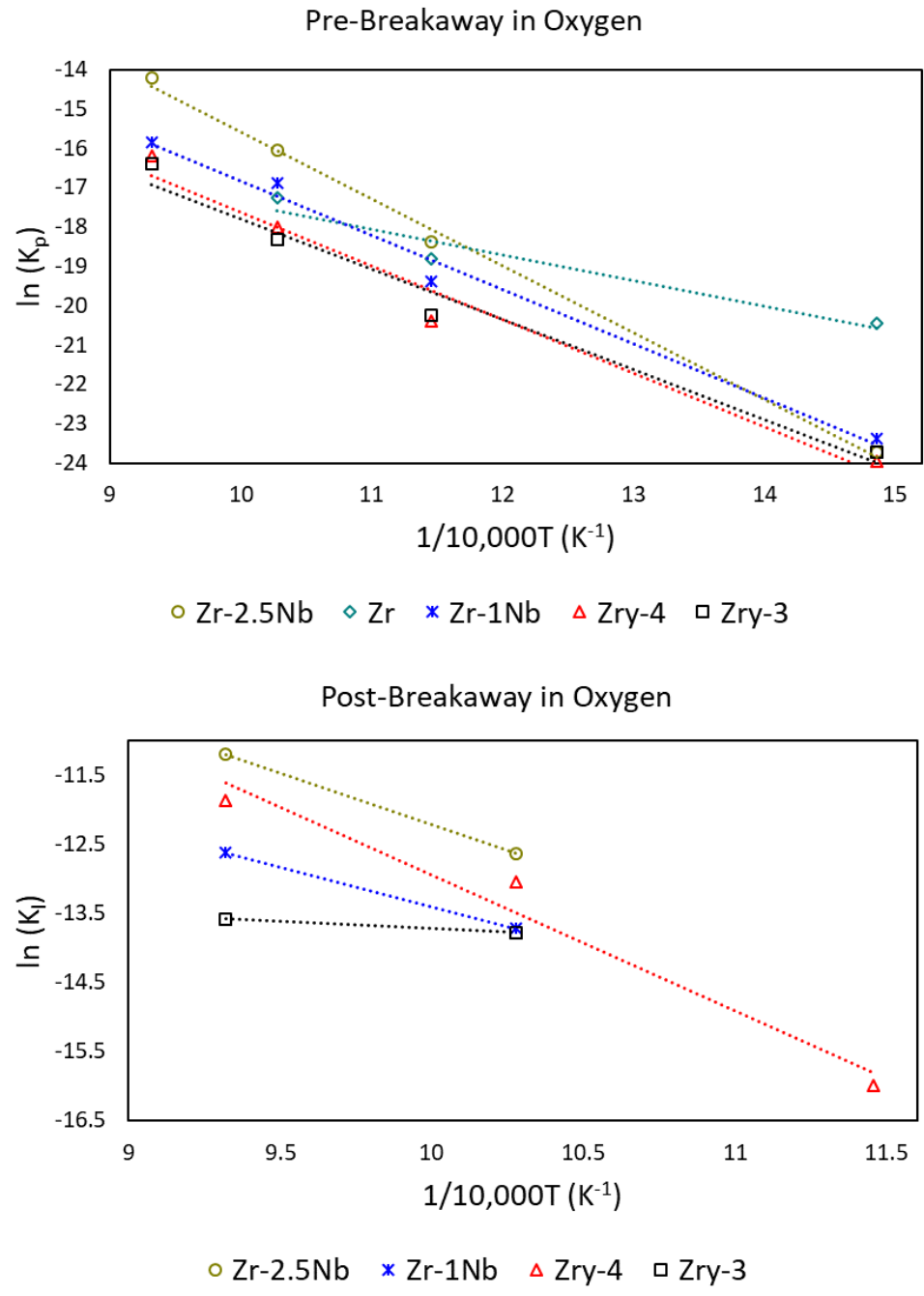


**Figure 2.8:** Arrhenius dependence of oxidation rate constant as a function of temperature after isothermal oxidation in oxygen where  $K_p$  and  $K_l$  are the parabolic and linear rate constants, respectively. The activation energy for oxidation can be derived from the slope of the plot according to Equation 2.

**Table 2.3:** Constants and slopes obtained from Arrhenius fits (Equation 2) as described above. The Arrhenius dependence for zirconium and zirconium alloys before and after breakaway during isothermal oxidation in oxygen is shown in Figure 2.8.

			Zr	Zry-3	Zry-4	Zr-1Nb	Zr-2.5Nb
Pre-Breakaway	Air	ln(A)	-5.30	-2.88	-3.26	-1.97	-0.69
		E <sub>a</sub> /R (K)	- 12890	-14535	-14018	-14821	-15384
		R <sup>2</sup>	0.98	0.98	0.95	0.99	0.99
	Oxygen	ln(A)	-3.36	-5.05	-3.98	-3.07	1.46
		E <sub>a</sub> /R (K)	- 14954	-12744	-13636	-13769	-17029
		R <sup>2</sup>	0.99	0.97	0.97	0.99	0.99
Post-Breakaway	Air	ln(A)	N/A	5.74	21.54	7.96	4.97
		E <sub>a</sub> /R (K)		-18719	-34459	-20897	-17087
		R <sup>2</sup>		-	0.96	-	-
	Oxygen	ln(A)	N/A	-11.68	6.66	-1.96	2.76
		E <sub>a</sub> /R (K)		-2041.8	-19612	-11441	-14972
		R <sup>2</sup>		-	0.97	-	-

**Table 2.4:** Calculated activation energies (E<sub>a</sub>) of each alloy in air or oxygen compared to values reported in literature. Activation energies are calculated for pre-breakaway (Pre-B) and post-breakaway (Post-B) regimes.

	Air			Oxygen		
	Pre-B E <sub>a</sub> (kJ/mol)	Literature Pre-B E <sub>a</sub> (kJ/mol)	Post-B E <sub>a</sub> (kJ/mol)	Pre-B E <sub>a</sub> (kJ/mol)	Literature Pre-B E <sub>a</sub> (kJ/mol)	Post-B E <sub>a</sub> (kJ/mol)
Zr	107	-	N/A	124	[16]: 179 [17]: 159	N/A
Zry-3	121	-	156	106	-	17.0
Zry-4	117	[5]: 86.8 [3]: 89.4 [18]: 114 [19]: 190 [20]: 130	286	113	[7]: 45.2	163
Zr-1Nb	123	[5]: 65.6 [3]: 54.2	174	114	-	95.0
Zr-2.5Nb	128	[21]: 79.4 [22]: 150	142	142	-	124

### 2.5.2 Pre-Breakaway

As previously mentioned, the oxidation of zirconium alloys typically follows parabolic or sub-parabolic kinetics until a transition (breakaway) occurs after which the kinetics become linear. After the initial adsorption of oxygen onto the surface of the metal, the parabolic (pre-breakaway) regime is controlled by the diffusion of oxygen anions through the oxide layer [12]. It is suggested in literature that the pre-breakaway oxidation mechanism is such that oxygen anions diffuse inward along crystallite boundaries in the oxide [9]. An inert marker experiment was performed on pure zirconium as well as all four alloys to determine if the same diffusion mechanism applies for all the materials investigated. A thin (50  $\mu\text{m}$  diameter) gold wire was welded onto the surfaces of the samples prior to oxidation at 700 °C in air and in oxygen for 140 minutes. Similar to literature, these experiments also suggested that an inward diffusion mechanism is present since the gold wire was found at the oxide/atmosphere interface in all cases. Although more studies would need to be done to confirm the exact oxidation mechanism, it is useful to know that the mechanism appears to agree with literature for all materials investigated.

The rate constants were determined by fitting the pre-breakaway regime with a parabolic fit, neglecting the initial oxidation of the bare metal (initial linear region of mass gain plot). The fitting parameters calculated by the method described in Section 2.5.1 are listed in Table 2.3 along with the  $R^2$  value that describes the variance between the data and the fit. For all materials except for Zry-4, there are only two temperatures where a post-breakaway oxidation rate can be extrapolated. For these alloys, an  $R^2$  value of 1 was found, indicating a perfect fit. This is an artifact of fitting two data points, thus the  $R^2$  values are not reported. The calculated activation energies are plotted with values reported in

literature in Figure 2.9. The pre-breakaway activation energies are similar between the two atmospheres (within approximately  $20 \text{ kJ/mol}$ ) for each alloy, further indicating that the presence of nitrogen in the oxidizing atmosphere does not significantly affect the pre-breakaway oxidation regime. Additionally, the activation energies are similar to values reported in literature. Discrepancies between literature values can be attributed to the wide variety of sample geometry, experimental setup, and oxidizing atmosphere reported.

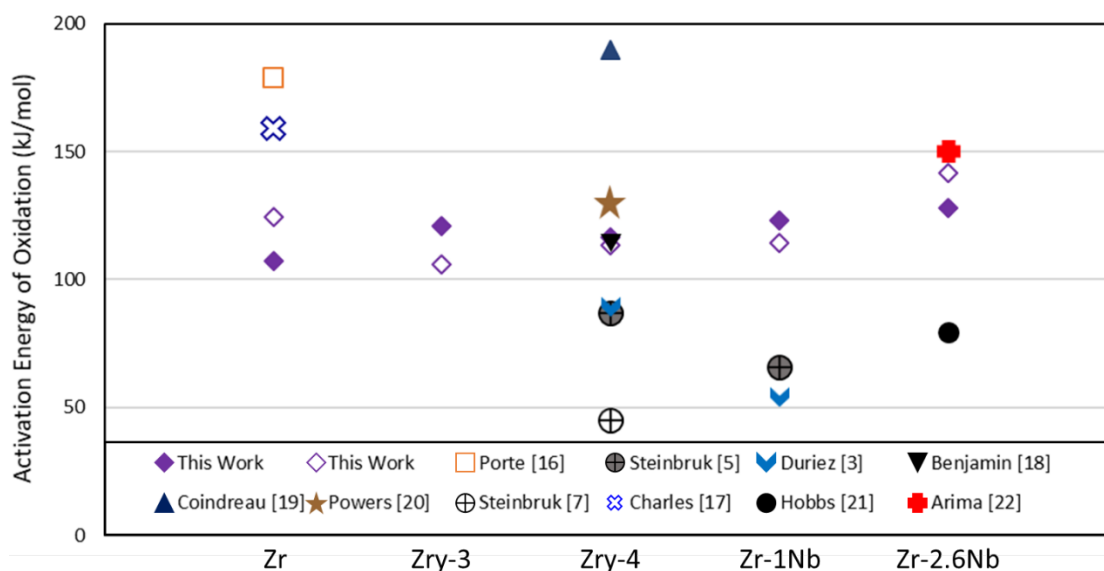


**Figure 2.9:** Calculated activation energies for Zr, Zry-3, Zry-4, Zr-1Nb, and Zr-2.5Nb compared to reported values. Solid symbols represent values obtained from oxidation in air, hollow symbols represent values obtained from oxidation in oxygen.

### 2.5.3 Post-Breakaway

The cracks formed during breakaway result in a direct path for oxygen to reach the metal surface, which has been shown to lead to accelerated oxidation kinetics. This transition is intensified by the presence of nitrogen in the atmosphere (Figure 2.4 and Table 2.2). It has been reported in literature that as oxygen is consumed within the cracks of the zirconium oxide, a nitrogen rich phase is formed [12,15]. As the oxygen is refreshed, the ZrN is oxidized in a rapid exothermic reaction, which results in a volume increase and a

porous, non-protective oxide [7,12,15]. This post-breakaway regime is best characterized with a linear rate law, where  $n=1$  in Equation 1. The calculated activation energies for each material in the post-breakaway regime are listed in Table 2.4 where it is seen that the activation energies for oxidation in air are significantly higher than in oxygen.

## 2.6 Conclusion

The oxidation behavior of Zr, Zry-3, Zry-4, Zr-1Nb, and Zr-2.5Nb of similar geometry in 80%N<sub>2</sub>+O<sub>2</sub> (air) and 80%Ar+O<sub>2</sub> (oxygen) in the temperature range 400-800 °C has been investigated and compared using thermogravimetric analysis. It has been observed that all four alloys exhibit the characteristic kinetic transition from parabolic to linear (breakaway) within 20 hours during isothermal oxidation at 700 and 800 °C. In all four alloys, the oxidation behavior is similar to what has been shown in literature; a dense protective oxide forms during pre-breakaway oxidation while the post-breakaway oxide is much thicker, cracked, and less protective [9-11].

Zr-2.5Nb was found to have most rapid oxidation kinetics of all the materials that were investigated and has similar oxidation rates in both air and oxygen. Zry-3 and Zr-1Nb were the most resistant to breakaway and had the slowest oxidation kinetics after breakaway. Zry-3, Zry-4, and Zr-1Nb had faster oxidation kinetics and thicker, more porous oxides after oxidation in air when compared to oxidation in oxygen. The Sn and Fe containing alloys were more sensitive to the oxidizing atmosphere than the Nb containing alloys and exhibited faster oxidation kinetics in air than in oxygen. The inert marker experiment confirmed that for all materials (including pure zirconium), the diffusing species is likely oxygen anions diffusing through the oxide to the underlying metal.

## 2.7 Acknowledgements

The work reported here was funded primarily through Department of Energy's National Nuclear Security Administration (DOE-NNSA) Office of Materials Minimization and Management. The authors would like to acknowledge K. Lester, L. Monteiro, N. Blancett, Y. Rodriguez-Ortego, and S. Mekonen at Boise State University for assistance in preparing and imaging samples. The authors would also like to acknowledge P. Boysen in the BSU machine shop for machining the sample coupons from the original sheet. Additionally, thanks to G. Alanko at ATI Specialty Alloys and Components for providing the Zr-2.5Nb material.

## 2.8 References

- [1] J. Carmack, Future transient testing of advanced fuels testing workshop, Rep. INL/EXT-09-16392. (2009).
- [2] C. Duriez, D. Drouan, G. Pouzadoux, Reaction in air and in nitrogen of pre-oxidised Zircaloy-4 and M5<sup>TM</sup> claddings, *J. Nucl. Mater.* 441 (2013) 84–95. doi:10.1016/j.jnucmat.2013.04.095.
- [3] C. Duriez, T. Dupont, B. Schmet, F. Enoch, Zircaloy-4 and M5<sup>®</sup> high temperature oxidation and nitriding in air, *J. Nucl. Mater.* 380 (2008) 30–45. doi:10.1016/j.jnucmat.2008.07.002.
- [4] M. Lasserre, V. Peres, M. Pijolat, O. Coindreau, C. Duriez, J.P. Mardon, Qualitative analysis of Zircaloy-4 cladding air degradation in O<sub>2</sub>-N<sub>2</sub> mixtures at high temperature, *Mater. Corros.* 65 (2014) 250–259.
- [5] M. Steinbrück, M. Böttcher, Air oxidation of Zircaloy-4, M5<sup>®</sup> and ZIRLO<sup>TM</sup> cladding alloys at high temperatures, *J. Nucl. Mater.* 414 (2011) 276–285. doi:10.1016/j.jnucmat.2011.04.012.

- [6] M. Steinbrück, Prototypical experiments relating to air oxidation of Zircaloy-4 at high temperatures, *J. Nucl. Mater.* 392 (2009) 531–544. doi:10.1016/j.jnucmat.2009.04.018.
- [7] M. Steinbrück, S. Schaffer, High-temperature oxidation of Zircaloy-4 in oxygen-nitrogen mixtures, *Oxid. Met.* 85 (2016) 245–262. doi:10.1007/s11085-015-9572-1.
- [8] E.T. Hayes, A.H. Roberson, Some effects of heating zirconium in air, oxygen, and nitrogen, *J. Electrochem. Soc.* 96 (1949) 142–151.
- [9] B. Cox, V.G. Kristsky, C. Lemaignan, V. Polley, I.G. Ritchie, H. Ruhmann, V.N. Shishov, *Waterside corrosion of zirconium alloys in nuclear power plants*, Vienna, Austria, 1998.
- [10] M. Lasserre, V. Peres, M. Pijolat, O. Coindreau, C. Duriez, J.P. Mardon, Modelling of Zircaloy-4 accelerated degradation kinetics in nitrogen–oxygen mixtures at 850°C, *J. Nucl. Mater.* 462 (2015) 221–229. doi:10.1016/j.jnucmat.2015.03.052.
- [11] M. Lasserre, O. Coindreau, M. Mermoux, M. Pijolat, V. Peres, J.P. Mardon, Study of Zircaloy-4 cladding air degradation at high temperature, in: *Int. Conf. Nucl. Eng. ICONE21-16440*, 2013: pp. 1–9.
- [12] E. Beuzet, J.S. Lamy, A. Bretault, E. Simoni, Modelling of Zry-4 cladding oxidation by air, under severe accident conditions using the MAAP4 code, *Nucl. Eng. Des.* 241 (2011) 1217–1224. doi:10.1016/j.nucengdes.2010.04.024.
- [13] B. Cox, Some thoughts on the mechanisms of in-reactor corrosion of zirconium alloys, *J. Nucl. Mater.* 336 (2005) 331–368. doi:10.1016/j.jnucmat.2004.09.029.
- [14] C. Duriez, M. Steinbrück, D. Ohai, T. Meleg, J. Birchley, T. Haste, Separate-effect tests on zirconium cladding degradation in air ingress situations, *Nucl. Eng. Des.* 239 (2009) 244–253. doi:10.1016/j.nucengdes.2008.10.017.
- [15] J. Stuckert, Z. Hózer, A. Kiselev, M. Steinbrück, Cladding oxidation during air ingress. Part I: experiments on air ingress, *Ann. Nucl. Energy.* 93 (2016) 4–17. doi:10.1016/j.anucene.2015.12.034.

- [16] H. a. Porte, J.G. Schnizlein, R.C. Vogel, D.F. Fischer, Oxidation of zirconium and zirconium alloys, *J. Electrochem. Soc.* 107 (1960) 506. doi:10.1149/1.2427733.
- [17] R.G. Charles, Prolonged oxidation of zirconium at 350 ° and 450 °C, *Trans. Am. Inst. Min. Metall. Eng.* 212 (1958) 101.
- [18] A. Benjamin, D.J. McCloskey, D.A. Powers, S. Dupree, Spent fuel heatup following loss of water during storage, *Nucl. Technol.* 49 (1980) 274–294.
- [19] O. Coindreau, C. Duriez, S. Ederli, Air oxidation of Zircaloy-4 in the 600–1000 °C temperature range: Modeling for ASTEC code application, *J. Nucl. Mater.* 405 (2010) 207–215. doi:10.1016/j.jnucmat.2010.07.038.
- [20] D.A. Powers, L.N. Kmetyk, R.C. Schmidt, A review of the technical issues of air ingress during severe reactor accidents, Nuclear Regulatory Commission, Washington, DC (United States). Div. of Systems Research; Sandia National Labs, Albuquerque, NM (United States), 1994.
- [21] L.W. Hobbs, V.B. Rosen, S.P. Mangin, M. Treska, G. Hunter, Oxidation microstructures and interfaces in the oxidized zirconium knee, *Int. J. Appl. Ceram. Technol.* 2 (2005) 221–246. doi:10.1111/j.1744-7402.2005.02025.x.
- [22] T. Arima, K. Miyata, K. Idemitsu, Y. Inagaki, Oxidation properties of Zr-Nb alloys at 973-1273 K in air, *Prog. Nucl. Energy.* 51 (2009) 307–312. doi:10.1016/j.pnucene.2008.08.001.

CHAPTER THREE: OXIDATION BEHAVIOR OF WELDED ZRY-3, ZRY-4, AND  
ZR-1NB TUBES

This chapter is in preparation for submission to Nuclear Materials and Energy.

## Oxidation Behavior of Welded Zry-3, Zry-4, and Zr-1Nb Tubes

Jordan L. Vandegrift<sup>1,2</sup>

Clemente J. Parga<sup>3</sup>

Ben Coryell<sup>3</sup>

Brian J. Jaques<sup>1,2</sup>

In preparation for submission to:

Nuclear Materials and Energy

1. *Boise State University, 1910 University Dr., Boise, ID 83725*
2. *Center for Advanced Energy Studies, 995 University Blvd., Idaho Falls, ID 83401*
3. *Idaho National Laboratory, 2525 Fremont Ave, Idaho Falls, ID 83402*

### 3.1 Abstract

The Transient Reactor Test (TREAT) facility is a research reactor designed to simulate rapid transients to test new fuel designs. TREAT's cladding is exposed to unique conditions compared to normal water reactors. These conditions include: exposure to air at high temperatures ( $\geq 600$  °C), rapid heating ( $\approx 700$  °C/s), and cladding geometry that includes chamfers and welds. This work investigates the effects of chamfering and welding on the oxidation behavior of zirconium alloys (Zircaloy-3, Zircaloy-4, and Zr-1Nb). Tube specimens were examined under isothermal and transient conditions in dry and humid air. The effect of weld type (tungsten inert gas or electron beam), the number of welds, and alloying elements are compared. Thermogravimetric analysis was used to collect mass gain data during isothermal oxidation and the data was used to quantify the oxidation rate

constant and the activation energy of oxidation. Oxide behavior in the weld region, chamfered region, and bulk tube was measured and compared. The microstructure and secondary phase precipitates in EBW tubes before and after breakaway were characterized. The electron beam welded Zr-1Nb specimen was found to have the most favorable oxidation behavior under both isothermal and transient conditions. Zry-4 oxidized the most readily and was the most affected by mechanical deformation.

### **3.2 Introduction**

The Transient Reactor Test (TREAT) facility is a nuclear test facility at the Idaho National Laboratory (INL) which is designed to simulate a variety of transient type scenarios and provide safety data on new fuel designs. As part of an effort to convert TREAT from a highly enriched uranium fuel core to a low enriched uranium core, and because the legacy Zircaloy-3 (Zry-3) fuel cladding material is no longer commercially available, alternative zirconium alloys are being evaluated for use as cladding. It is important to understand the oxidation behavior of zirconium alloys, because it is the limiting factor for the maximum core temperature [1]. The oxidation behavior of zirconium alloys is not well studied in TREAT's conditions, which include: operation temperatures between 400-600 °C with an 820 °C design basis accident temperature (DBA), rapid transients up to 700 °C/s, and the use of air as coolant. Some literature is available on the behavior of zirconium alloys in these conditions; however, no studies have been completed to provide a direct comparison, with the same experimental parameters, of the alloys of interest. It has been shown that the corrosion resistance of zirconium alloys decreases with increasing temperature, and the oxidation reaction is thought to be catalyzed by the nitrogen present in air [2-4]. In a previous publication, the oxidation behavior of pure Zr,

Zry-3, Zircaloy-4 (Zry-4), Zr-1Nb, and Zr-2.5Nb plate samples were systematically compared in both synthetic air and oxygen from 400-800 °C [5]. It was found that all four alloys experienced faster post-breakaway oxidation kinetics and had thicker, less protective oxides after oxidation in air compared to oxygen. Additionally, the Zr-1Nb oxidation kinetics were the slowest and it was the most resistant to the characteristic breakaway oxidation when compared to the Sn and Fe (Zry-3 and Zry-4) containing alloys [5].

TREAT's cladding differs from traditional cladding in that it has chamfers and welds (as seen in Figure 3.1), both of which can alter the microstructure and, ultimately, the oxidation behavior of the fuel pin [6-8]. The grains in the weld region typically coarsen from the base metal towards the fusion zone, where the metal has experienced the highest temperature during welding [7]. The grains in the base metal are usually equiaxed grains corresponding to  $\alpha$ -Zr that coarsen in the heat affected zone (HAZ). In the fusion zone (FZ), the grains are found to be lamellar  $\alpha$ -Zr [9]. Zhang et al. found that electron beam welded (EBW) Zr-702 (an Fe, Cr, and Hf containing alloy) had improved corrosion resistance in the weld region over the base metal due to dissolution of secondary phases during welding [9]. Cai et al. determined that weld beads formed using pulsed laser beam welding on a zirconium alloy containing Nb, Sn, and Fe spacer grid experienced excessive cracking compared to the base metal due to stresses at the metal/oxide interface [10]. Additionally, Ryabichenko et al. found that tungsten inert gas (TIG) welded Zr-Nb alloys had similar corrosion resistance to EBW alloys [11]. Although some studies on the oxidation behavior of EBW and TIG welded zirconium alloys have been reported, none present a direct comparison of the oxidation of Zry-3, Zry-4, and Zr-1Nb welded tubes in TREAT's conditions.



**Figure 3.1: Rendering of TREAT's unique fuel cladding assembly, which includes chamfered corners and welded end caps.**

Mechanical deformation (such as chamfering) affects the microstructure of the bulk metal, however, it is unclear how this affects the oxidation behavior of zirconium alloys. Plastic deformation has been shown to decrease the grain size and increase dislocation density of zirconium [12-14]. Modeling the oxidation of zirconium with various grain sizes indicates that corrosion resistance of zirconium increases with decreasing grain size before breakaway [15]. However, the model did not predict how grain size would affect the breakaway transition or the oxidation kinetics after breakaway. Additionally, only zirconium metal was modelled, alloying constituents were not considered. In some cases, such as plastic deformation via high pressure torsion, the stresses created from the deformation can result in phase transformations in the zirconium matrix and secondary phase precipitates [13]. Studies have reported that the oxidation behavior of zirconium varies with the phase of the metal. The room temperature  $\alpha$ -Zr phase and  $\beta$ -Nb phase improve corrosion resistance, while the  $\beta$ -Zr phase is detrimental to corrosion resistance [16,17]. It is unknown how plastic deformation from chamfering will affect the microstructure and oxidation behavior of zirconium alloys. Although some studies have been reported on the effect of plastic deformation on the microstructure of zirconium, the effect of chamfering on the oxidation behavior Zry-3, Zry-4, and Zr-1Nb remains unclear.

This work is intended to provide a direct comparison between three candidate zirconium alloy cladding materials, Zry-3, Zry-4, and Zr-1Nb during both isothermal and

rapid transient experiments in dry and humid air. The effects of welding, weld type, and chamfering on the oxidation kinetics are compared.

### 3.3 Experimental Procedures

#### 3.3.1 Materials

Zry-3, Zry-4, and Zr-1Nb tube samples were fabricated at the INL by plastically deforming sheets of material with 15 chamfers and welding the seam with either a single longitudinal EBW, two longitudinal EBW, or two longitudinal TIG welds. The tubes had an approximate diameter of 16 mm and the Zry-3 tubes had a wall thickness of 0.63 mm while Zry-4 and Zr-1Nb had wall thicknesses of 0.66 mm. Prior to oxidation, the tubes were subjected to an annealing heat treatment to remove stresses present from fabrication. The annealing heat treatment included heating to 450 °C at 20 K/min ramp under high vacuum ( $10^{-7}$  torr) where they were held for 24 hours before being cooled to room temperature at the same rate. The tubes were cleaned by sonication in a solution of 1:1:1 acetone:ethanol:deionized water before oxidation. The composition of the zirconium alloys is shown in Table 3.1.

**Table 3.1: Typical composition of zirconium alloys in wt % [24].**

	Sn	Fe	Cr	O	Nb
<b>Zry-3</b>	0.25	0.25	-	-	-
<b>Zry-4</b>	1.5	0.21	0.1	0.13	-
<b>Zr-1Nb</b>	-	0.015-0.06	-	0.09-0.12	1

#### 3.3.2 Isothermal Oxidation

Twenty-hour isothermal oxidation experiments in dry and humid synthetic air (certified N<sub>2</sub> + 20% O<sub>2</sub>) were performed in a NETZSCH STA-449 F3 Jupiter equipped with thermogravimetric analysis (TGA). A platinum-mesh plate was used as a sample carrier to maximize the interaction of the sample with the reactant gases as shown in Figure 3.2.

Humid air oxidation experiments were done with a partial pressure of water  $P_{H_2O}=0.29$  psi (30% relative humidity at 100 °F), which is typical of the moisture content in the desert air during typical TREAT operation. The dry air oxidation experiments were performed on single EBW, double EBW (2-EBW), and TIG welded tubes. All isothermal oxidation experiments in the temperature range 500-700 °C were held for 20 hours. Experiments done at 800 and 820 °C were shortened due to severe degradation of the specimens. After oxidation the mass gain data (normalized to the measured initial surface area of the tubes) was used to quantify the oxidation rate constants of each alloy at each temperature. The determined oxidation rates were then used to determine the activation energies for oxidation of each specimen.

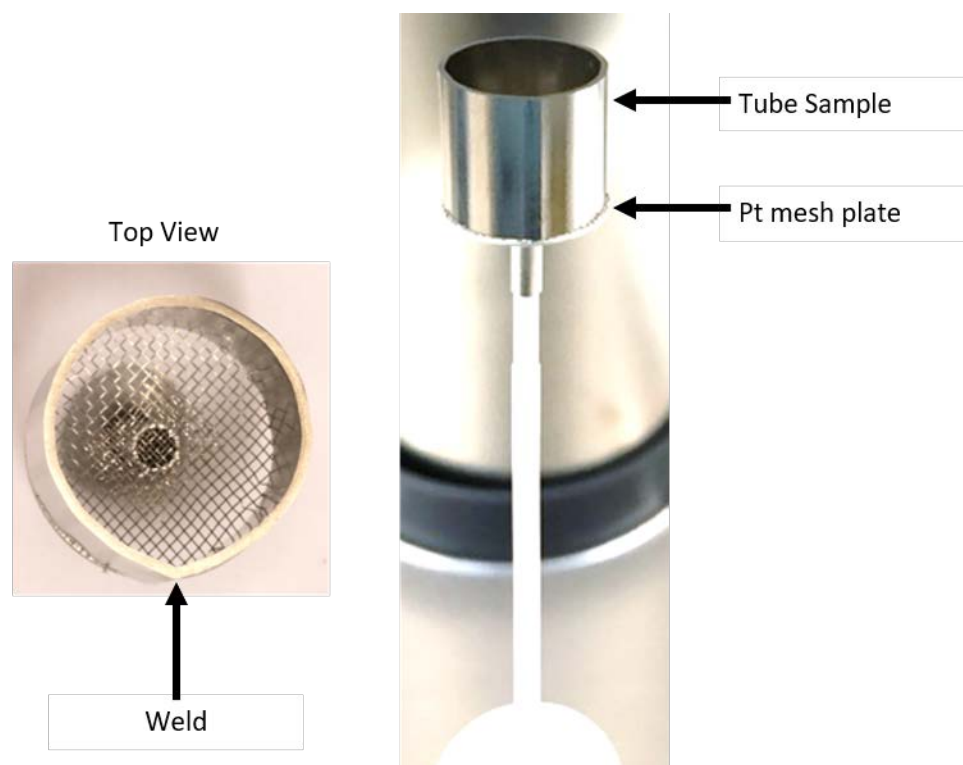


**Figure 3.2:** Experimental setup inside the STA showing a welded tube specimen on the platinum mesh plate.

The oxide thickness of the non-plastically deformed (bulk), chamfered, and welded regions were each measured after 20-hour isothermal oxidation at 700 °C. Only samples oxidized at 700 °C were measured because a direct comparison of oxidation behavior could be made, whereas the samples oxidized at higher temperatures were oxidized for various durations, as previously stated. The tubes were ground down approximately 2 mm from the top surface to image the metal/oxide interface using optical microscopy. At least 30 measurements were taken for the bulk and chamfer regions, and at least 15 measurements were taken of the weld region.

### 3.3.3 Transient Oxidation

As previously stated, TREAT is designed to produce rapid transients with heating rates up to 700 °C/s and a relatively slow cooling rate over an extended period of time (10 or more hours to reach room temperature). To replicate these conditions, fifteen transients from 600–500 °C ( $\approx$  600 minutes of exposure) were completed to simulate normal TREAT operation, followed by a transient from 820–450 °C to simulate a DBA scenario. One of the temperature profiles measured from these experiments is shown in Figure 3.3. To replicate the transients, a benchtop muffle furnace was heated to the temperature of interest (either 600 or 820 °C) and the specimen was inserted through a port on the top of the furnace. A pure zirconium tube with a thermocouple spot welded onto the surface was inserted simultaneously with the specimen to monitor the temperature (Figure 3.4). The experiments were repeated for 2 samples per alloy. The samples were weighed and imaged between each cycle.

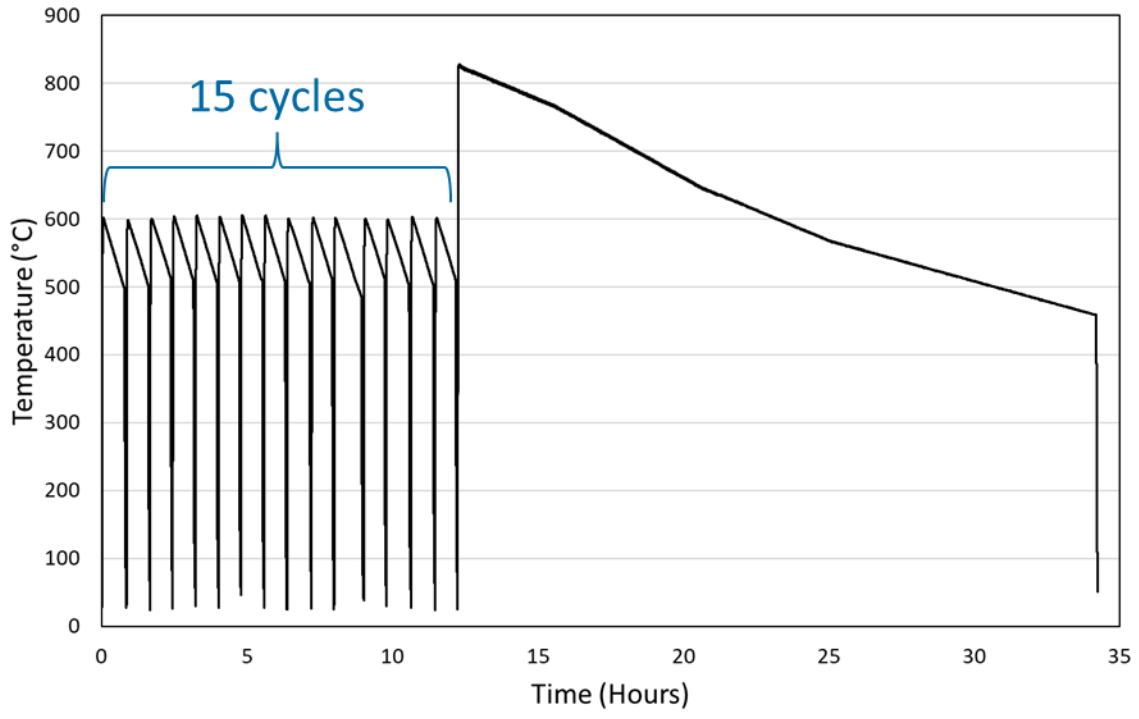


**Figure 3.3: Transient oxidation temperature profile followed for each sample showing fifteen transients from 600 – 500 °C simulating normal TREAT operation, followed by a DBA temperature profile from 820 – 450 °C.**

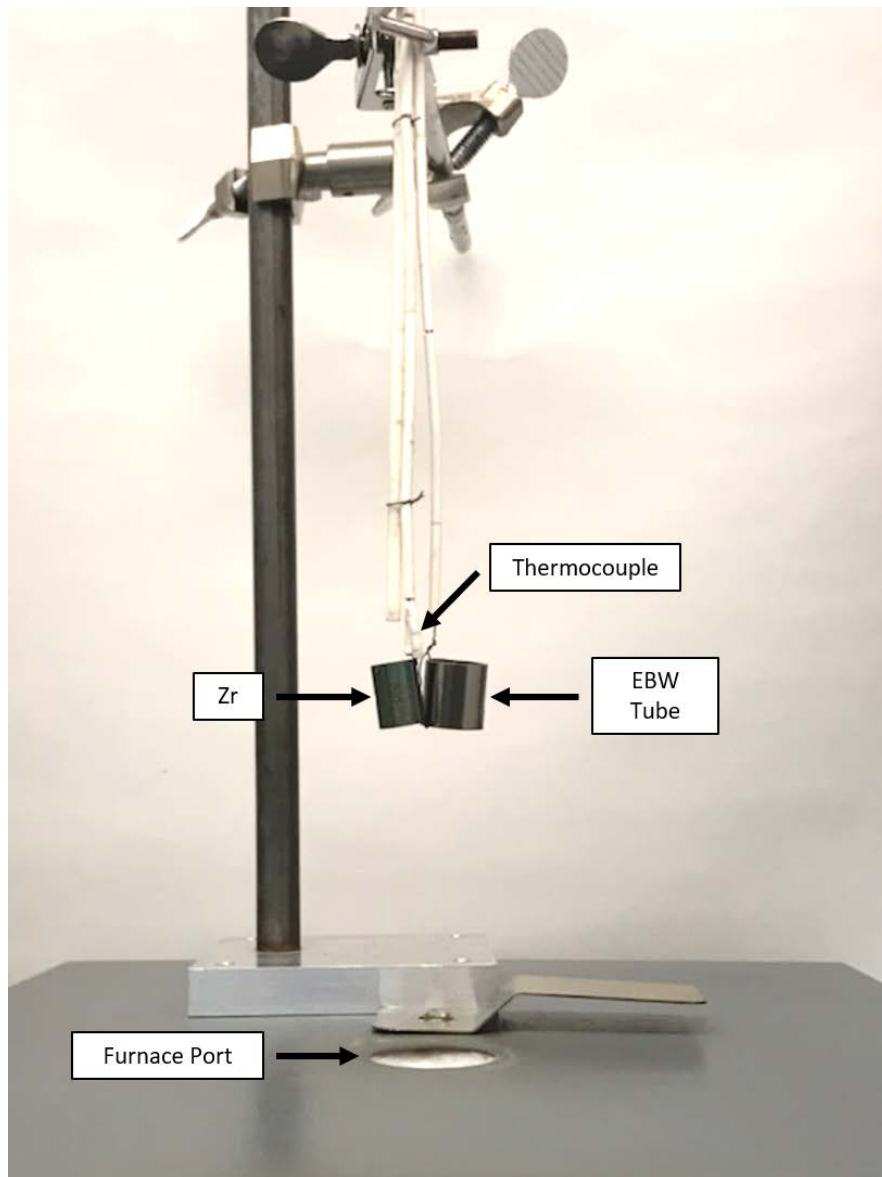


**Figure 3.4:** Experimental setup for transient oxidation experiments. A pure Zr tube with a thermocouple spot welded to the surface was inserted into the furnace with the EBW zirconium alloy tube to monitor temperature during the experiment.

### 3.4 Results

#### 3.4.1 Isothermal Oxidation

The macroscopic images after isothermal oxidation of EBW and TIG welded Zry-3, Zry-4, and Zr-1Nb in dry and humid air are shown in Figure 3.5, Figure 3.6, and Figure 3.7. The corresponding normalized mass gain data collected during oxidation is shown in

Figure 3.8. As seen in the mass gain plots, breakaway oxidation occurs in all three alloys at temperatures  $\geq 700$  °C and Zry-4 experiences breakaway the earliest of the three alloys, while Zr-1Nb is the most resistant to breakaway.

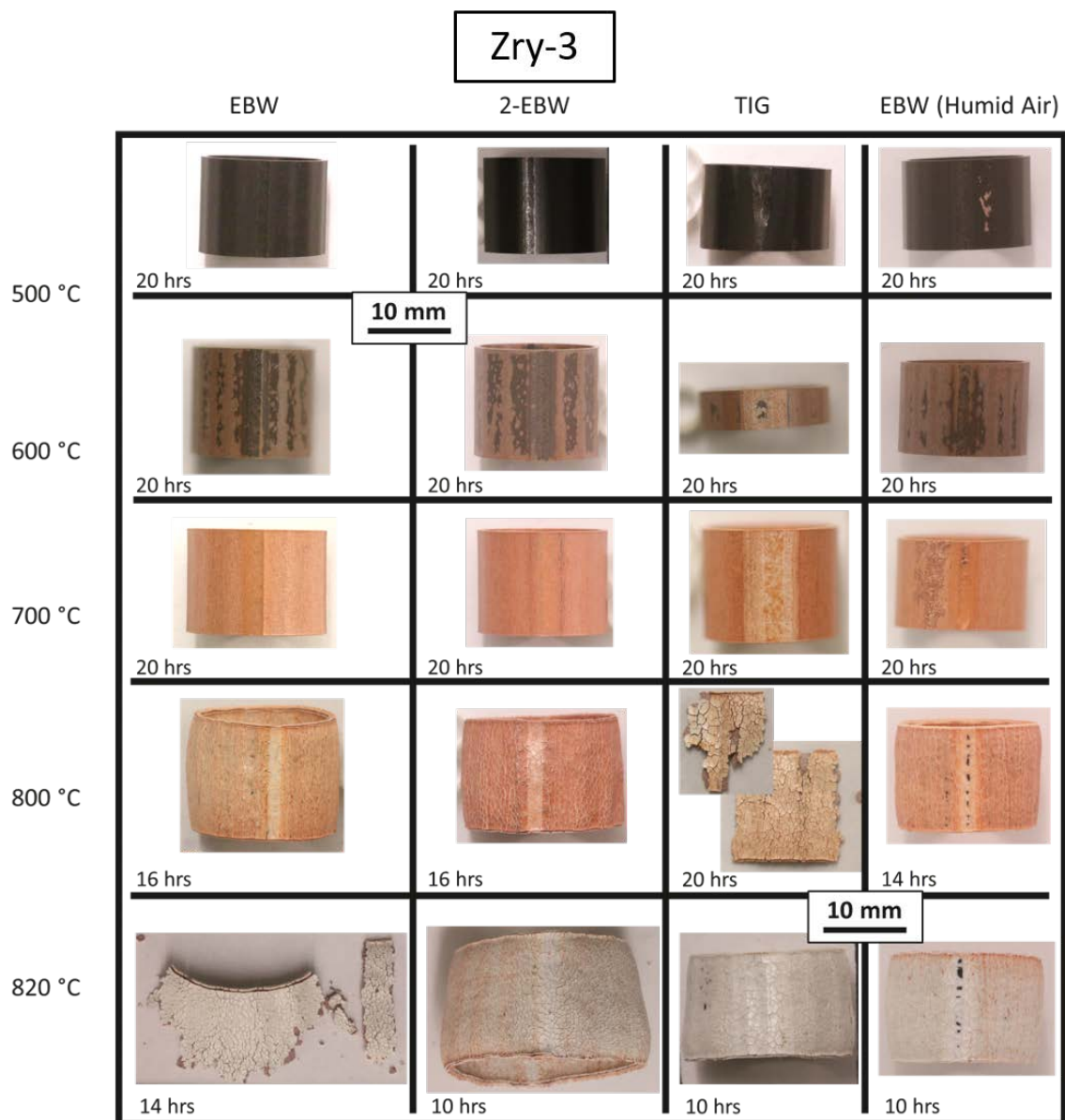


**Figure 3.5:** Macroscopic images of Zry-3 EBW or TIG welded tubes after isothermal oxidation experiments in dry or humid air.

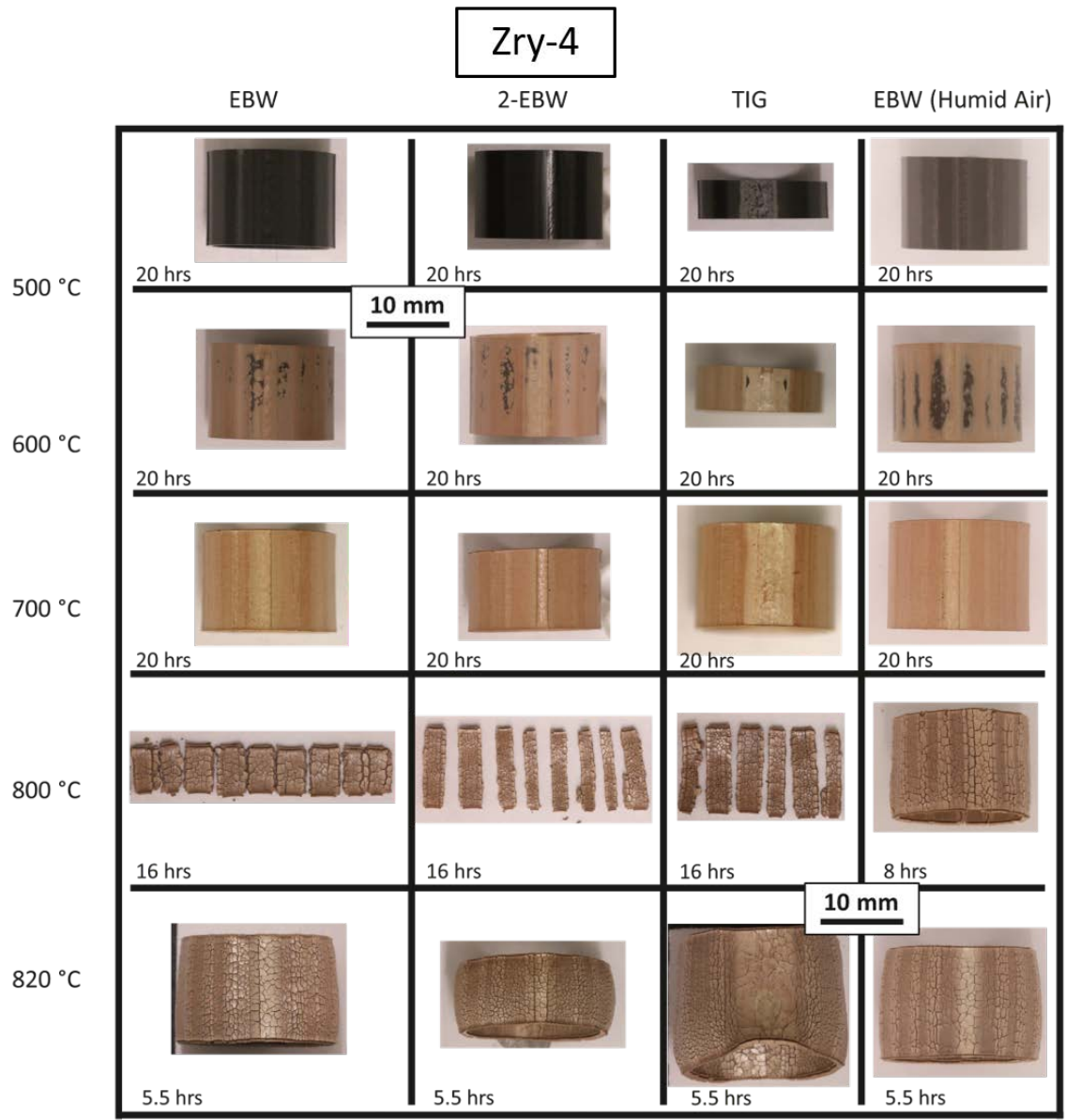


**Figure 3.6: Macroscopic images of Zry-4 EBW or TIG welded tubes after isothermal oxidation experiments in dry or humid air.**

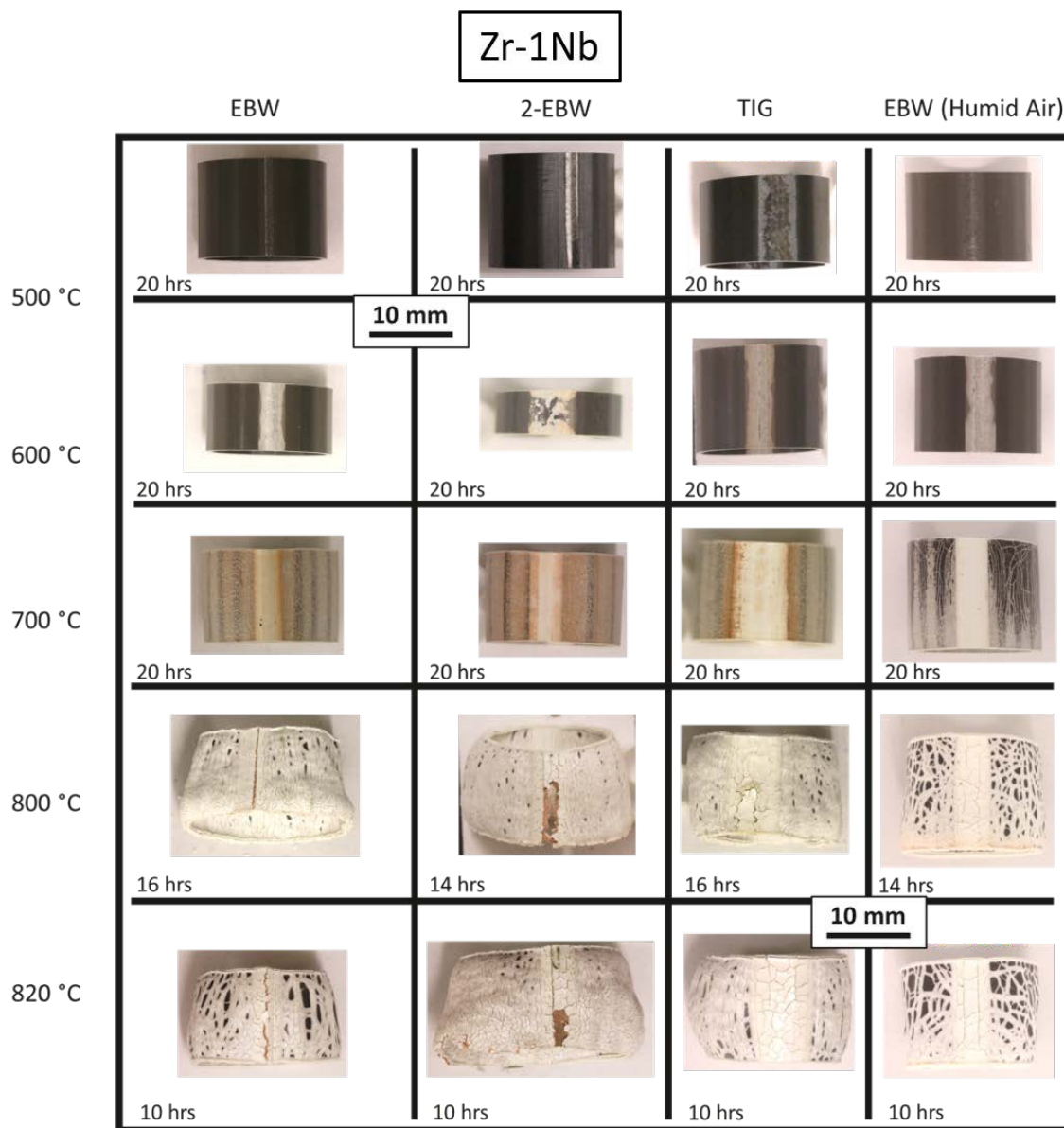


**Figure 3.7: Macroscopic images of Zr-1Nb EBW or TIG welded tubes after isothermal oxidation experiments in dry or humid air.**

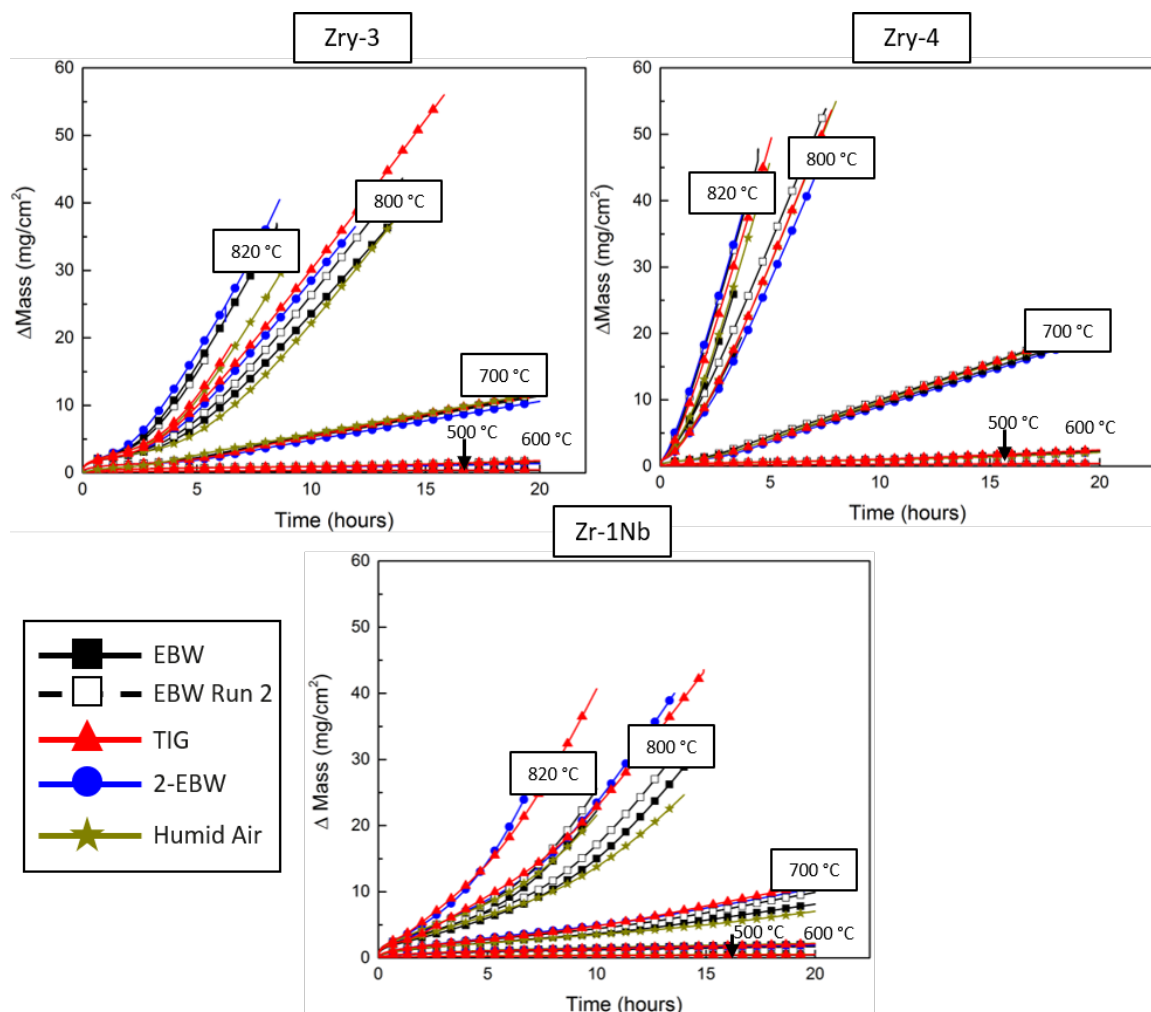


**Figure 3.8:** Mass gain normalized to measured initial surface area during isothermal oxidation experiments of EBW or TIG welded Zry-3, Zry-4, Zr-1Nb tubes in dry or humid air.

From Figure 3.5-Figure 3.7, and as expected from the discussion above, the HAZ is larger in the TIG welded tubes than in the EBW specimens [18]. The effect of plastic deformation on oxidation behavior is seen in the Sn-Fe containing alloys (Zry-3 and Zry-4); accelerated oxidation on the chamfer regions are clearly visible. In cases where the sample fell apart, the Zry-3 and Zry-4 failed at the chamfers. The opposite is true for the Zr-1Nb alloy; accelerated oxidation occurs first on the non-plastically deformed, or bulk, regions of the tube and fracture occurred at the weld. In contrast to the other two alloys, Zr-1Nb experiences accelerated oxidation in a crack-like network on the surface rather than on the

entirety of the surface as seen in the images taken after 800 and 820 °C oxidation. The same behavior was seen during the oxidation of plate specimens [5]. Ballooning occurs in Zry-3 and Zr-1Nb after oxidation  $\leq 800$  °C and after oxidation at 820 °C in Zry-4, although most of these samples fell apart at 800 °C making it difficult to determine if ballooning occurred or not. In Zry-4 and Zr-1Nb, the color of the oxide at the weld is noticeably different than the rest of the tube, the weld region being significantly lighter. This difference in color is also seen on Zry-3, however it is less pronounced, particularly on the EBW tubes oxidized at low temperatures.

From the mass gain data in Figure 3.8, EBW and TIG welded tubes have similar oxidation kinetics in Zry-4 at all temperatures. The effects of humid air on breakaway oxidation rates, for all specimens, appears insignificant. However, there was a slight difference in oxidation behavior between EBW and TIG welded Zry-3 and Zr-1Nb tubes. The single EBW Zry-3 tube oxidized in both dry and humid air resisted breakaway longer than the TIG welded and 2-EBW tubes during 800 °C oxidation. However, the EBW tube oxidized in humid air and the TIG welded tubes in dry air resisted breakaway the longest at 820 °C. A consistent trend is seen from the mass gain data during oxidation of Zr-1Nb. A difference can be seen in Zr-1Nb at high temperatures, with the single EBW tubes resisting breakaway oxidation longer than the TIG welded tubes.

Figure 3.9 shows the average oxide thickness of each specimen after isothermal oxidation at 700 °C. The measurements agree with what is seen in the images of the specimens: the oxidation behavior of Zry-3 is unaffected by chamfering or welding as there is no statistical difference in the oxide thickness between the three regions. The effect of chamfering and welding is clearly seen in Zry-4 (as is visible in Figure 3.6); the chamfer

and weld regions are approximately 70% thicker than the bulk regions. Zr-1Nb also exhibits accelerated oxidation at the weld, also clearly visible in Figure 3.7, while the bulk and chamfered regions have similar oxide thickness.

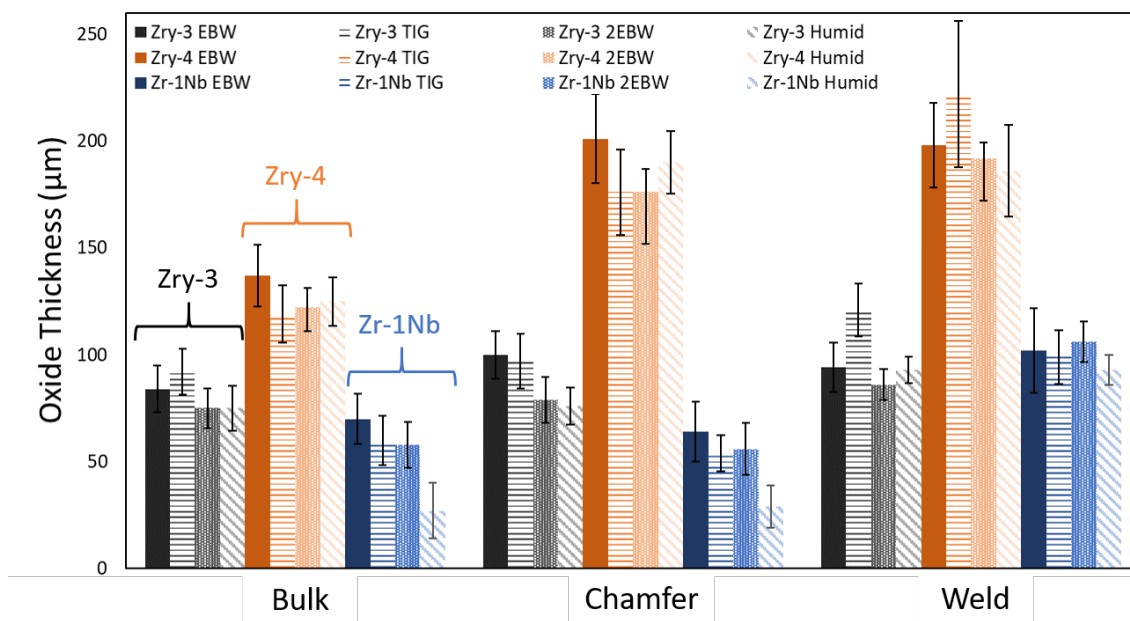


**Figure 3.9:** Oxide thickness of each section of the welded tubes after 20-hour isothermal oxidation at 700 °C. The error bars are the standard deviation of 15 (weld) or 30 (bulk and chamfer) measurements.

### 3.4.2 Transient Oxidation

Images of the EBW tubes before oxidation ( $N = 0$ ), after the first and fifteenth 600 °C transient cycles ( $N = 1$  and  $N = 15$ ) and the final 820 °C transient (*DBA*) are shown in Figure 3.10. The behavior of the alloys after transient oxidation is similar to what is seen after isothermal oxidation. Zry-3 and Zry-4 experience accelerated oxidation first on the chamfers (more prominent on Zry-4), while Zr-1Nb maintains its protective oxide until the *DBA* transient. It should be noted that the as received Zry-3 tube had deformation present next to the weld from the fabrication process (to the right of the weld, Figure 3.10). The deformation had different surface texture, and therefore different oxidation behavior than

the rest of the tube. After the DBA transient, the characteristic crack-like accelerated oxidation is present along with accelerated oxidation at the weld in Zr-1Nb.

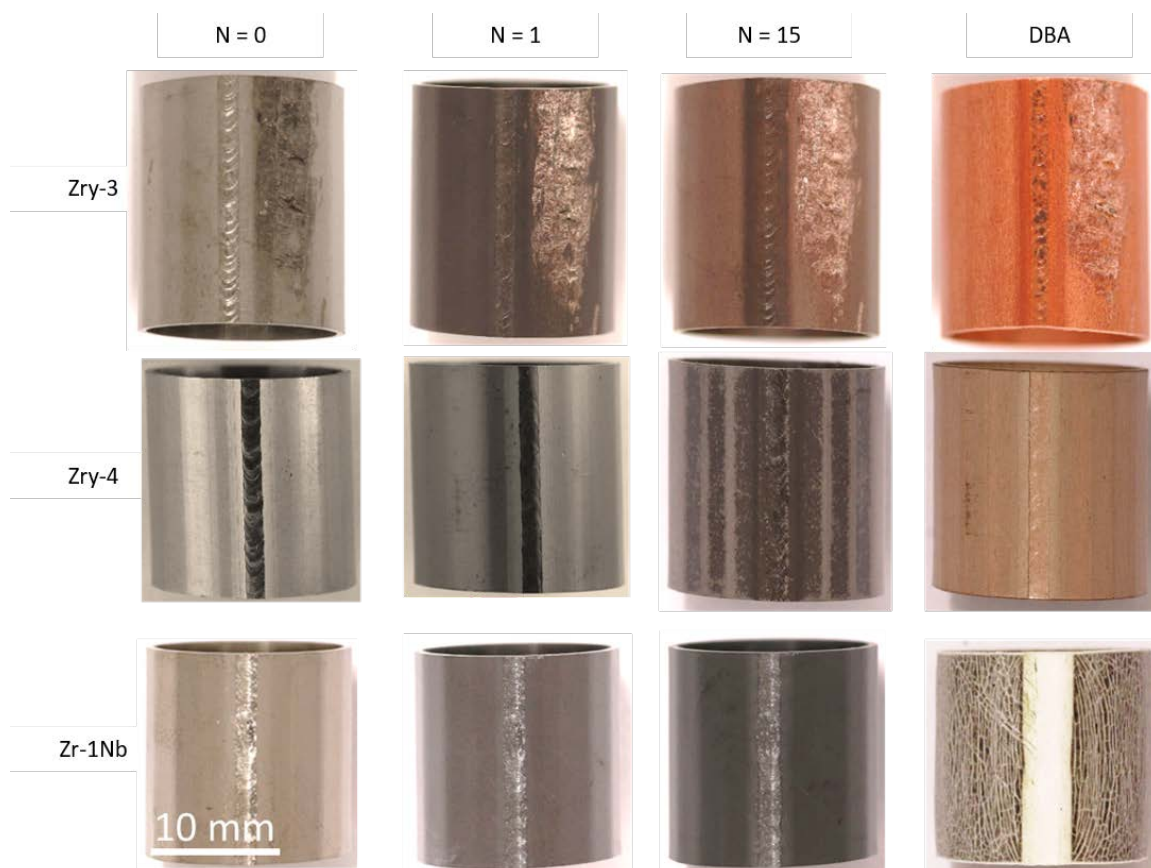


**Figure 3.10: EBW Zry-3, Zry-4, and Zr-1Nb after N = 0, 1, 15 (600 °C) and DBA (820 °C) transient oxidation cycles.**

### 3.5 Discussion

#### 3.5.1 General Oxidation Behavior

The initial oxidation behavior of zirconium alloys is typically characterized by parabolic kinetics and is governed by diffusion of oxygen anions through the oxide layer [19]. Once the oxide reaches a critical thickness, it cracks and exposes bare metal, which provides a direct path for oxygen to reach the surface. The kinetics then become linear and oxidation occurs very rapidly [4,19]. This transition is termed “breakaway.” The pre- and post-breakaway oxidation kinetics were quantified according to the method presented in a

previous publication [5]. The parabolic and linear rate constants for each specimen were determined and then plotted Arrheniusly. The activation energies were calculated from the slope of the curve as discussed in previous work [5]. The activation energies ( $E_a$ ), constant ( $A$ ), and variance between the data and linear fit ( $R^2$ ) both before and after breakaway are in Table 3.2. The activation energies are rounded to the nearest  $10 \text{ kJ/mol}$  due to the inherent uncertainty associated with fitting data that is highly dependent on the surface area of the starting material, which is not trivial to measure with the chamfered specimens.

**Table 3.2: Constants,  $R^2$  values, and calculated activation energies for oxidation of chamfered and welded Zry-3, Zry-4, and Zr-1Nb in air obtained from Arrhenius fits.**

		Pre-Breakaway			Post-Breakaway		
		$\ln(A)$	$-E_a$ (kJ/mol)	$R^2$	$\ln(A)$	$-E_a$ (kJ/mol)	$R^2$
<b>Zry-3</b>	EBW run 1	-0.92	130	0.99	5.27	150	1
	EBW run 2	0.57	140	0.99	4.21	140	0.99
	EBW-2	1.26	150	1	6.81	160	1
	TIG	-0.19	140	1	4.64	140	1
	Humid Air	-1.32	130	0.99	5.33	150	0.94
<b>Zry-4</b>	EBW run 1	2.21	160	1	6.65	150	1
	EBW run 2	3.19	160	1	7.29	160	1
	EBW-2	2.84	160	0.99	8.08	170	1
	TIG	0.98	150	0.99	6.73	160	1
	Humid Air	0.92	150	1	7.33	160	1
<b>Zr-1Nb</b>	EBW run 1	-0.83	130	0.99	5.50	150	1
	EBW run 2	-3.56	100	0.93	5.41	150	0.99
	EBW-2	3.75	170	0.99	8.10	170	1
	TIG	0.53	140	0.99	6.74	160	1
	Humid Air	0.25	140	0.99	5.87	160	0.99

### 3.5.2 Effect of Welding and Plastic Deformation on Oxidation Behavior

It has been shown that the oxidation behavior of zirconium alloys is dependent on the microstructure and secondary phases in the base metal [6-8]. The high temperature of welding alters the microstructure of the zirconium alloys, as is visible in the optical images

of the alloys in Figure 3.11-Figure 3.13, which shows the microstructure of the EBW bulk, chamfered, and welded regions in the as received material and after 700 °C isothermal oxidation in dry air. The grains in the bulk metal and HAZ are small, equiaxed shaped grains that become increasingly coarser towards the FZ. The FZ exhibits lamellar shaped grains similar to what has been shown in literature [9]. No difference in microstructure is seen between the bulk and chamfered regions in any of the alloys. In Zry-3 (Figure 3.11), after oxidation, precipitates appear to be homogeneously dispersed in the non-welded regions. As seen in Figure 3.12, no precipitates are visible after oxidation and the microstructure is similar to the as received microstructure. The grains in Zr-1Nb are much smaller than in the other alloys and are more visible after oxidation, which is likely due to segregation of precipitates at the grain boundaries.

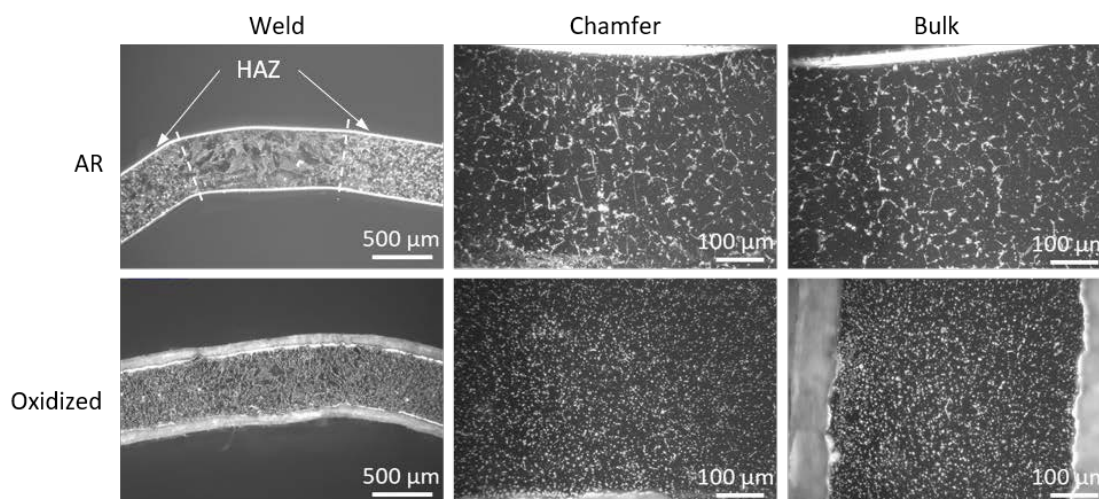


**Figure 3.11: Dark field optical images of as received (AR) EBW Zry-3 and after 20-hour isothermal oxidation at 700 °C in dry air. The microstructure of the weld, chamfered, and bulk regions are shown.**

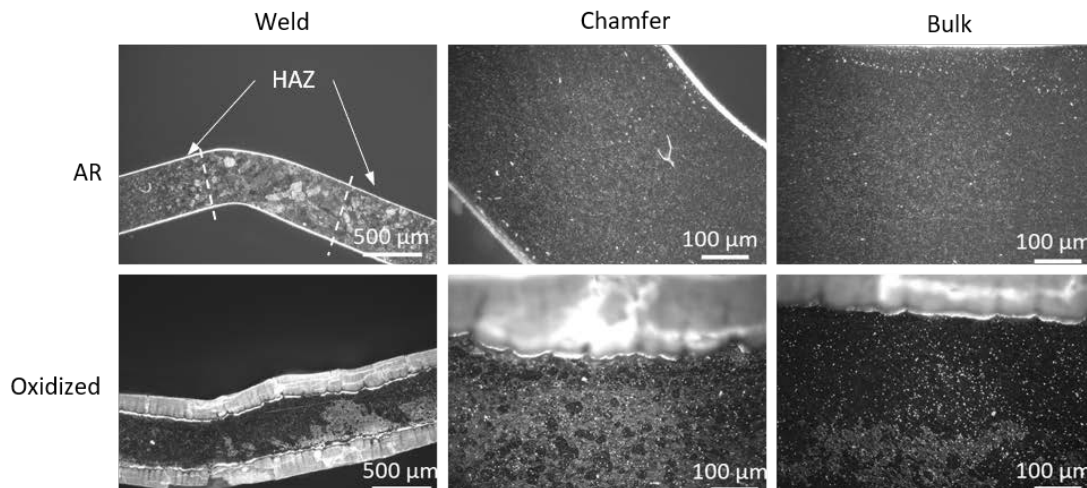


**Figure 3.12: Dark field optical images of as received (AR) EBW Zry-4 and after 20-hour isothermal oxidation at 700 °C in dry air. The microstructure of the weld, chamfered, and bulk regions are shown.**

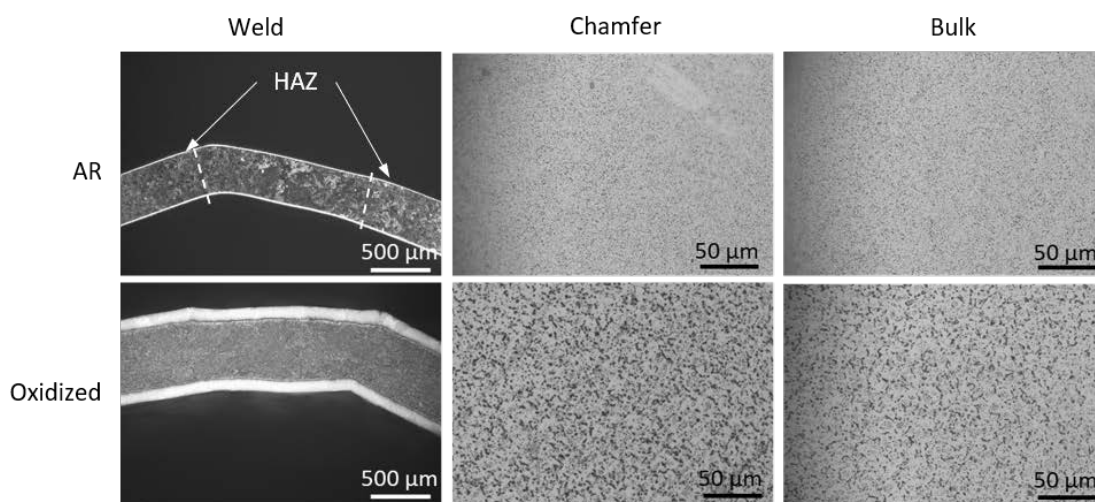


**Figure 3.13: Dark field (weld) and bright field (chamfer and bulk) optical images of as received (AR) EBW Zr-1Nb and after 20-hour isothermal oxidation at 700 °C in dry air. The microstructure of the weld, chamfered, and bulk regions are shown.**

Scanning electron microscopy (SEM) and energy dispersive x-ray spectroscopy (EDS) were used to characterize the as received and oxidized (700 °C dry air) EBW tubes. Images of the weld and bulk microstructure of the alloys before and after oxidation are shown in Figure 3.14-Figure 3.16. Prior to oxidation, no precipitates are present in the welded region of the three alloys. Similar results have been reported for zirconium alloys

as a result of EBW [7,9]. It is probable that the temperature achieved during welding was high enough for the precipitates to dissolve into the matrix. The non-welded regions of Zry-3 contained Fe-rich precipitates at the grain boundaries before oxidation, as shown in Figure 3.17. These precipitates were found to contain between 2-5 wt% Fe, while the surrounding matrix contained between 0.2-0.4 wt% Sn in solution, as expected from Table 3.1. No precipitates were found in Zry-4 or Zr-1Nb prior to oxidation.

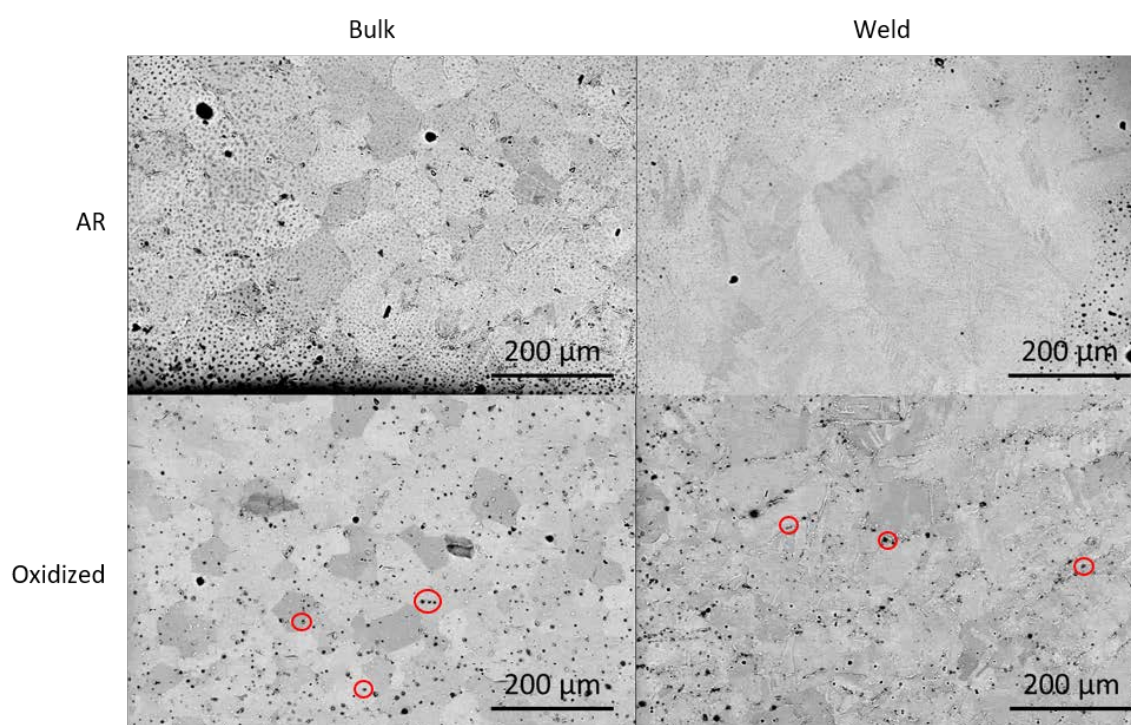


**Figure 3.14: SEM images of the weld and bulk microstructure of as received (AR) and oxidized (700 °C dry air) EBW Zry-3. All images were collected using backscatter electrons. The circles on the images after oxidation highlight high concentration Fe precipitates.**

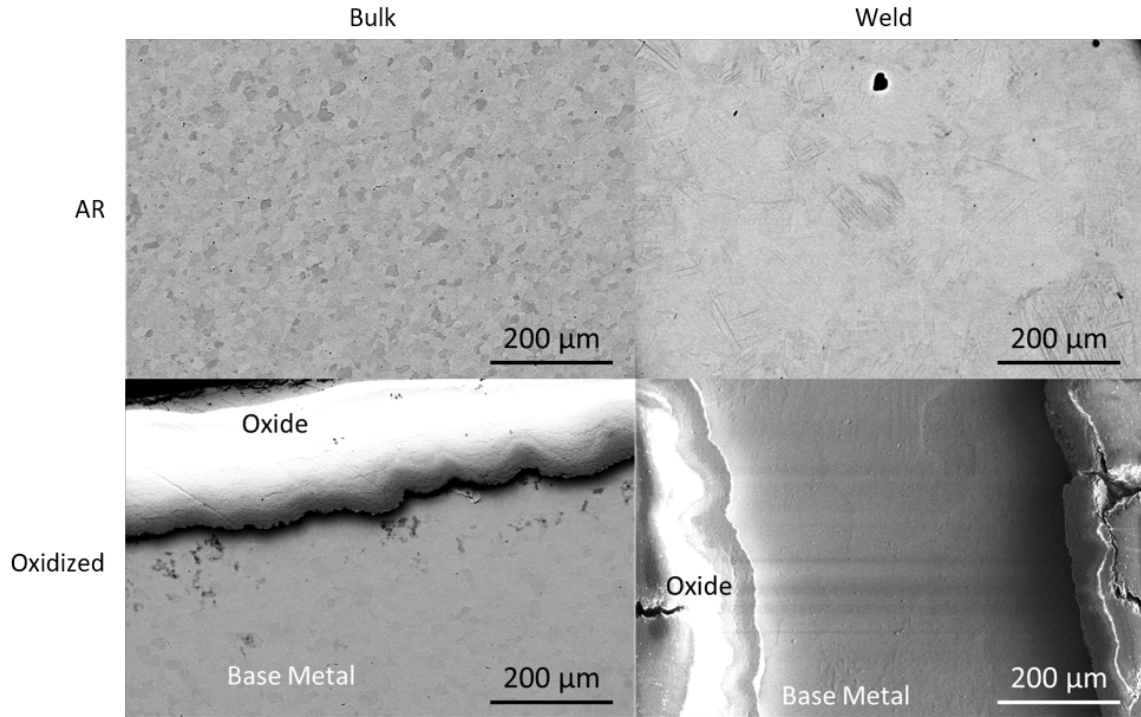


**Figure 3.15: SEM images of the weld and bulk microstructure of as received (AR) and oxidized (700 °C dry air) EBW Zry-4. All images were collected using backscatter electrons except the oxidized weld region, which is a secondary electron image.**

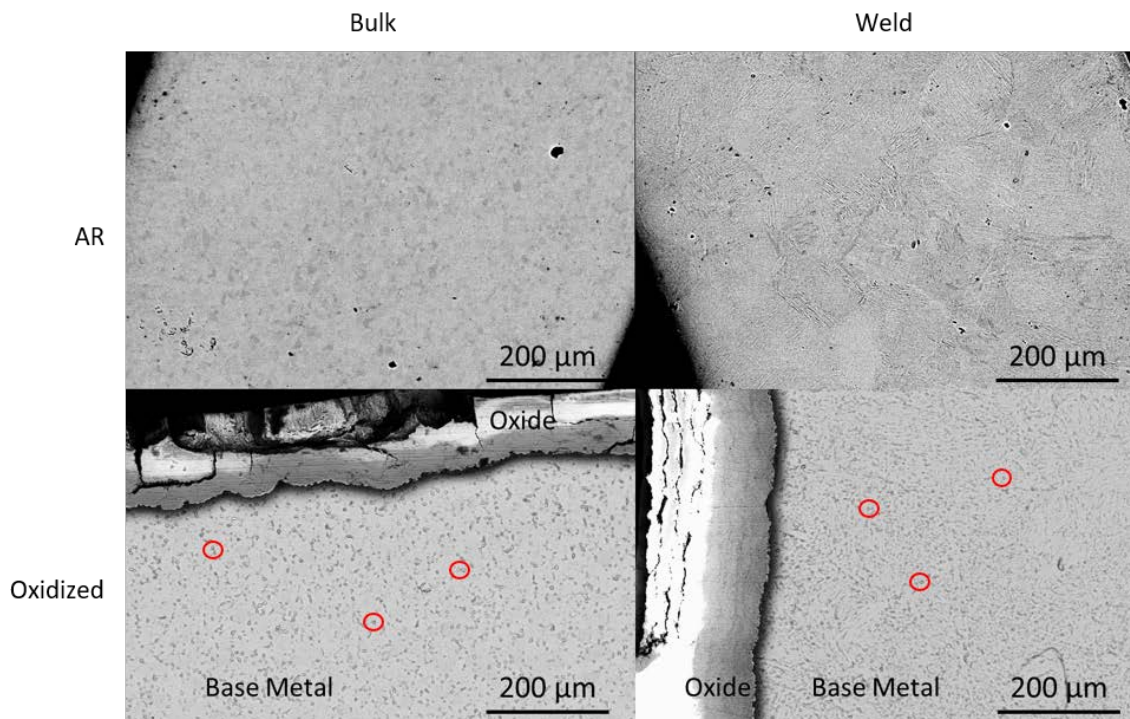


**Figure 3.16: SEM images of the weld and bulk microstructure of as received (AR) and oxidized (700 °C dry air) EBW Zr-1Nb. All images were collected using backscatter electrons. The circles on the images highlight the Nb and O-rich precipitates identified through EDS.**

After oxidation, increased Fe precipitation is seen at the grain boundaries in Zry-3 in all regions. The Fe segregation at the grain boundaries seen before oxidation remains, but with a slightly lower Fe concentration ( $\approx 1$  wt%). However, precipitates with much higher Fe concentration (11-13 wt%) formed during oxidation, seen as the dark spots in Figure 3.14 (highlighted with circles). Additionally, an approximately 20  $\mu\text{m}$  Fe-depleted region was identified at the metal/oxide interface in both the welded and non-welded regions, where the concentration dropped to nearly 0%. This depleted region was not observed in Zry-4 or Zr-1Nb. During oxidation, Fe segregated to the grain boundaries in the welded region of Zry-4 and had a composition of approximately 0.8 wt% Fe. No precipitates were identified in the non-welded regions. It has been well characterized that precipitates such as Fe act as nucleation sites for oxidation and can result in stresses and

cracks in the oxide, leading to enhanced oxidation [20-22]. Accordingly, the presence of Fe precipitates in the welded region of Zry-4 could contribute to the accelerated oxidation seen in this region. In Zr-1Nb, the precipitates at the grain boundaries after oxidation (some of which are highlighted in Figure 3.16) were found to be Nb and O-rich, with some precipitates containing up to 6 wt% Nb. The formation of small Nb precipitates in zirconium alloys has been shown to enhance resistance to breakaway oxidation due to the reduction of supersaturation of Nb in the Zr matrix and stabilization of the tetragonal zirconia phase [17,23]. The resistance to breakaway oxidation of Zr-1Nb is clear from Figure 3.8.

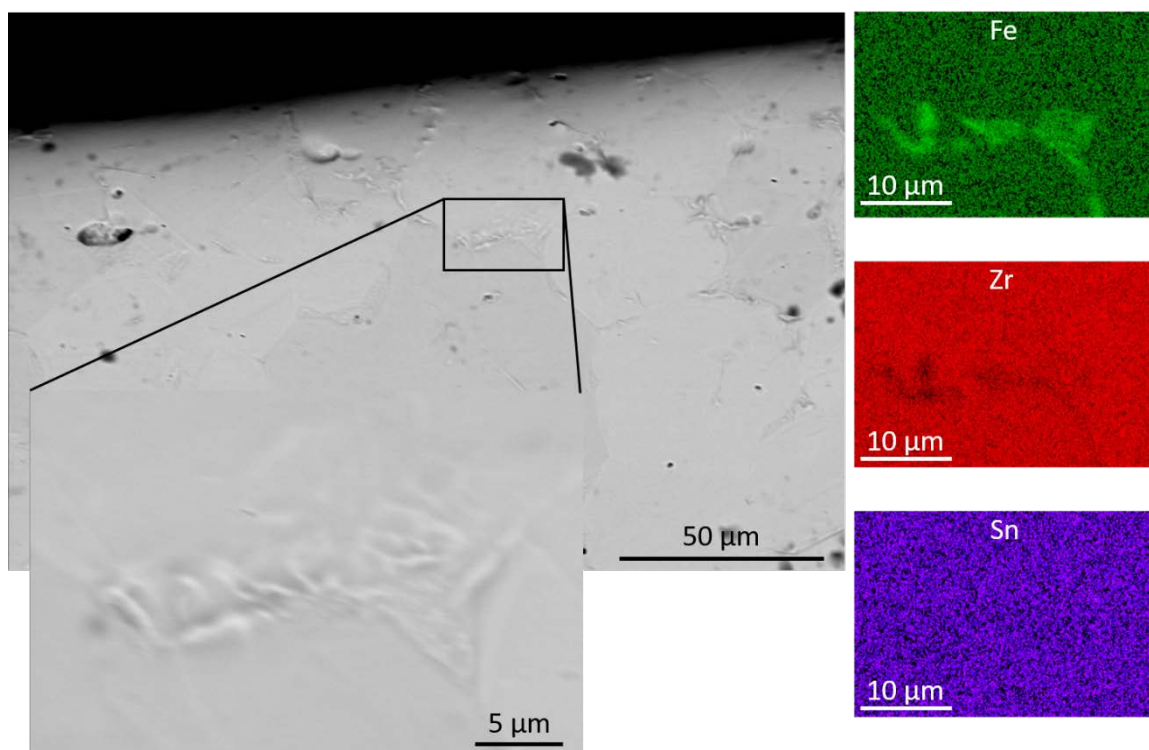


**Figure 3.17: SEM image and corresponding EDS maps of Fe-rich precipitates found at the grain boundaries of the non-welded regions of as received EBW Zry-3. The intensity of the EDS maps corresponds to concentration of the element in the material.**

### 3.5.3 Transient Oxidation

The mass gain (normalized to surface area before oxidation) of each specimen during  $N = 0-15$  and DBA transients and theoretical oxide thickness for each alloy is shown in Figure 3.18. The data is averaged between 2 runs. Minimal mass gain occurred during transients  $N = 1-15$  and all alloys experienced similar mass gain. After the 820 °C transient, a similar trend appears that was seen during isothermal oxidation: Zry-4 experienced the most mass gain while Zr-1Nb experienced the least after the DBA transient. The maximum allowed thickness is also shown in Figure 3.18. This maximum value is defined by the INL as 17% of the original wall thickness of the tube. The thinnest wall thickness (0.635 mm) was used to calculate the maximum oxide thickness shown in Figure 3.18 to reflect a conservative value. It is clear that during the 600 °C transients, which is TREAT's maximum normal operating temperature, the oxide thickness is well below the maximum allowed thickness. Even after an 820 °C transient, or accident temperature, all alloys are still well below this maximum thickness. However, the cladding would need to be replaced following a DBA transient to prevent failure during future normal operating conditions.

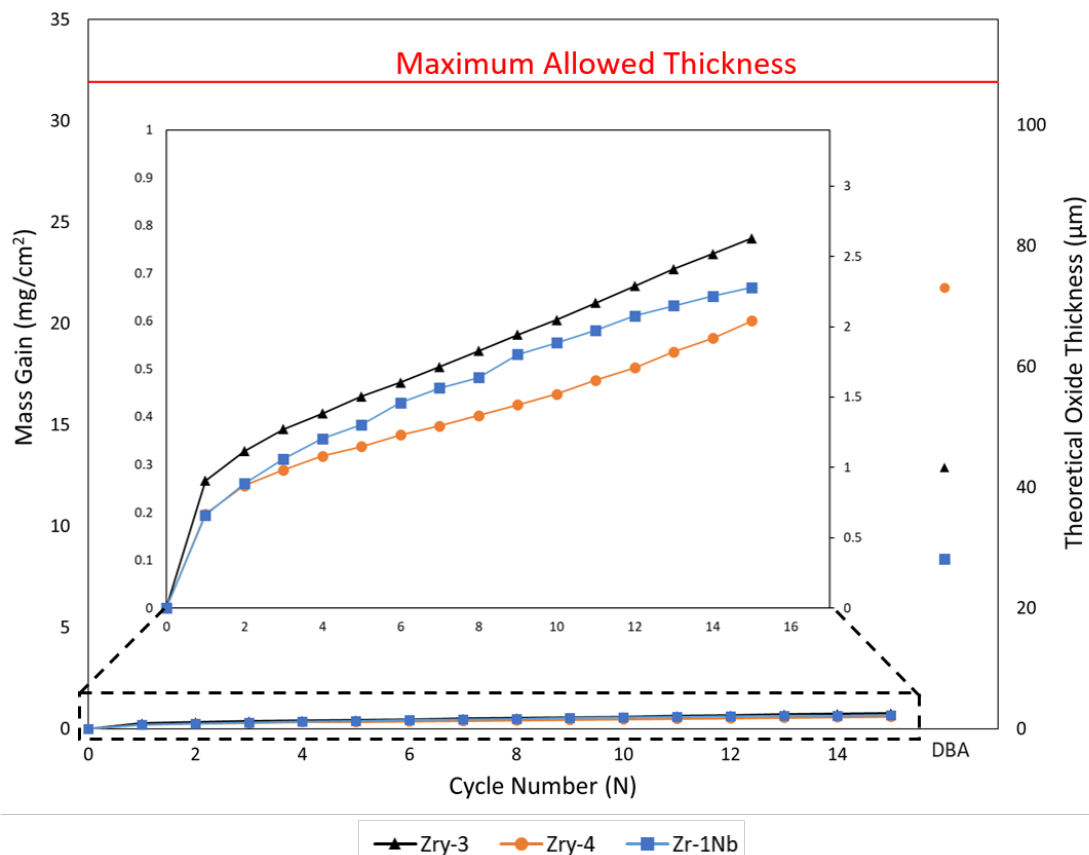


**Figure 3.18:** Average mass gain between runs 1 and 2 and associated theoretical oxide thickness after each 600 °C transient (N = 1-15) and after the final 820 °C DBA transient. Maximum allowed oxide thickness (17% of the original wall thickness) is shown for reference. The inset shows a magnified view of the mass gain and theoretical oxide thickness after the 600 °C transients.

### 3.6 Conclusion

TREAT's cladding is unique in that it has welds, chamfers, and is exposed to rapid transients (700 °C/s) in air. To study the effect of these conditions on potential cladding material, welded and chamfered Zry-3, Zry-4, and Zr-1Nb tubes have been oxidized under isothermal and transient conditions in both dry and humid air in the temperature range 500-820 °C. Thermogravimetric analysis data was used to quantitatively compare the oxidation behavior between the alloys and weld types. The data was then used to identify the oxidation kinetics of each specimen. Zry-4 was found to be the least resistant to the breakaway transition and oxidized the most rapidly, whereas Zr-1Nb was the most resistant

to breakaway. The oxide thickness was measured on the weld, chamfer, and bulk regions of the tubes after 20-hour isothermal oxidation at 700 °C and compared. It can be seen from the images in Figure 3.6 that Zry-4 experiences accelerated oxidation on the chamfered regions which is confirmed by the measurements in Figure 3.9. The oxide thickness is consistent between all three regions in Zry-3 at this temperature; however, at temperatures above 700 °C, it is clear that the tubes will fail at either the chamfer or the weld (Figure 3.5 and Figure 3.9). The oxide on the weld for Zr-1Nb was thicker than the other two regions, which is also seen from the images. Additionally, the oxidation behavior was the same regardless of weld type in Zry-4 as seen in Figure 3.8, while the Zr-1Nb EBW tubes resisted breakaway longer than the TIG welded tubes at temperatures  $\leq 700$  °C. In Zry-3 at oxidation temperatures  $\geq 700$  °C, the EBW and TIG welded tubes had similar oxidation kinetics. At 800 °C, the EBW tubes resisted breakaway longer than the TIG welded tubes; however, at 820 °C the TIG welded tubes resisted breakaway the longest.

Comparing the microstructure of the EBW tubes before and after oxidation (Figure 3.11-Figure 3.16), it was seen that precipitation of secondary phases occurred in all three alloys during oxidation. After oxidation, Zry-3 and Zry-4 contained Fe-rich precipitates at the grain boundaries. In Zry-3, this occurred in the entire specimen. However, in Zry-4, the precipitation occurred only in the weld region. Zr-1Nb had small Nb-rich precipitates after oxidation. Comparing the microstructure between the weld, chamfer, and bulk regions of the EBW tubes, a clear difference is seen between the welded and non-welded regions. The welded regions consist of lamellar grains that coarsen towards the FZ, while the non-welded regions consist of small, equiaxed grains. The microstructure between the bulk and chamfered regions appear the same.

All three alloys had similar behavior during transient oxidation as in isothermal oxidation. Zry-4 experienced accelerated oxidation on the chamfered regions during the 600 °C transient cycles while Zry-3 only experienced slightly increased oxidation on the chamfers. Zr-1Nb maintained a thin, dense oxide on the entire tube through all 600 °C transients. Additionally, it was determined that after 15 cycles to TREAT's maximum normal operating temperature, followed by an accident type transient to 820 °C, the oxide thickness of all three alloys is still well below (<30 %) the maximum allowed thickness defined by the INL.

### 3.7 Acknowledgements

The work reported here was funded primarily through Department of Energy's National Nuclear Security Administration (DOE-NNSA) Office of Materials Minimization and Management. The authors would like to thank A. Lupercio and J. Watkins at Boise State University for assistance in performing some of the TGA experiments. The authors would also like to acknowledge B. Forsmann at the Center for Advanced Energy Studies for his help preparing and imaging samples for oxide thickness measurements.

### 3.8 References

- [1] J. Carmack, Future transient testing of advanced fuels testing workshop, Rep. INL/EXT-09-16392. (2009).
- [2] C. Duriez, T. Dupont, B. Schmet, F. Enoch, Zircaloy-4 and M5® high temperature oxidation and nitriding in air, *J. Nucl. Mater.* 380 (2008) 30–45. doi:10.1016/j.jnucmat.2008.07.002.
- [3] C. Duriez, D. Drouan, G. Pouzadoux, Reaction in air and in nitrogen of pre-oxidised Zircaloy-4 and M5TM claddings, *J. Nucl. Mater.* 441 (2013) 84–95. doi:10.1016/j.jnucmat.2013.04.095.

- [4] M. Steinbrück, S. Schaffer, High-temperature oxidation of Zircaloy-4 in oxygen-nitrogen mixtures, *Oxid. Met.* 85 (2016) 245–262. doi:10.1007/s11085-015-9572-1.
- [5] J.L. Vandegrift, P.M. Price, J.P. Stroud, C.J. Parga, I.J. Van Rooyen, B.J. Jaques, D.P. Butt, Oxidation behavior of Zirconium, Zircaloy-3, Zircaloy-4, Zr-1Nb, and Zr-2.5Nb in air and oxygen, *Nuclear Materials and Energy.* (2019). doi:10.1016/j.nme.2019.100692.
- [6] Y.H. Jeong, K. Ok, H.G. Kim, H.G. Jeong, Y. H., Lee, K. O., Kim, Y.H. Jeong, K. Ok, H.G. Kim, Correlation between microstructure and corrosion behavior of Zr – Nb binary alloy, *J. Nucl. Mater.* 302 (2002) 9–19. doi:10.1016/S0022-3115(02)00703-1.
- [7] C. Cai, L. Li, W. Tao, G. Peng, X. Wang, Weld bead size, microstructure and corrosion behavior of zirconium alloys joints welded by pulsed laser spot welding, *J. Mater. Eng. Perform.* 25 (2016) 3783–3792. doi:10.1007/s11665-016-2250-x.
- [8] K.Y. Huang, The effect of heat treatment on the microstructure and the corrosion resistance of Zircaloy-4 in 450 °C steam, *J. Nucl. Mater.* 136 (1985) 16–29.
- [9] B. Zhang, X. Li, T. Wang, X. Wang, Microstructure and corrosion behavior of Zr-702 joined by electron beam welding, *Vacuum.* 121 (2015) 159–165. doi:http://dx.doi.org/10.1016/j.vacuum.2015.08.005.
- [10] C. Cai, W. Tao, L. Li, Y. Chen, Weld bead formation and corrosion behavior of pulsed laser welded zirconium alloy, *Int. J. Adv. Manuf. Technol.* 77 (2015) 621–628. doi:10.1007/s00170-014-6474-3.
- [11] B.R. Ryabichenko, The corrosion resistance of welded joints in a zirconium-niobium alloy, *Autom. Weld.* 38 (1985) 17–20.
- [12] A.Y. Eroshenko, A.M. Mairambekova, Y.P. Sharkeev, Z.G. Kovalevskaya, M.A. Khimich, P. V Uvarkin, Structure, phase composition and mechanical properties in bioinert zirconium-based alloy after severe plastic deformation, 7 (2017) 469–472.

- [13] S.O. Rogachev, S.A. Nikulin, A.B. Rozhnov, M. V Gorshenkov, Microstructure, phase composition, and thermal stability of two zirconium alloys subjected to high-pressure torsion at different temperatures, *Adv. Eng. Mater.* 20 (2018). doi:10.1002/adem.201800151.
- [14] D. Fuloria, N. Kumar, R. Jayaganthan, S.K. Jha, D. Srivastava, An investigation of effect of annealing at different temperatures on microstructures and bulk textures development in deformed Zircaloy-4, *Mater. Charact.* 129 (2017) 217–233. doi:10.1016/j.matchar.2017.04.038.
- [15] X.Y. Zhang, M.H. Shi, C. Li, N.F. Liu, Y.M. Wei, The influence of grain size on the corrosion resistance of nanocrystalline zirconium metal, *Mater. Sci. Eng. A.* 448 (2007) 259–263. doi:10.1016/j.msea.2006.10.029.
- [16] C.J. Parga, S.K. Varma, Correlation between microstructures and oxidation resistance in Zr-Nb-Ti alloys, *Metall. Mater. Trans. A Phys. Metall. Mater. Sci.* 40 (2009) 2987–2993. doi:10.1007/s11661-009-0017-9.
- [17] K.N. Choo, Y.H. Kang, S.I. Pyun, V.F. Urbanic, Effect of composition and heat treatment on the microstructure and corrosion behavior of Zr-Nb alloys, *J. Nucl. Mater.* 209 (1994) 226–235. doi:10.1111/cpr.12282.
- [18] P. Rudling, A. Strasser, F. Garzarolli, *Welding of Zirconium Alloys*, 2007.
- [19] E. Beuzet, J.S. Lamy, A. Bretault, E. Simoni, Modelling of Zry-4 cladding oxidation by air, under severe accident conditions using the MAAP4 code, *Nucl. Eng. Des.* 241 (2011) 1217–1224. doi:10.1016/j.nucengdes.2010.04.024.
- [20] C. Proff, S. Abolhassani, M.M. Dadras, C. Lemaignan, In situ oxidation of zirconium binary alloys by environmental SEM and analysis by AFM, FIB, and TEM, *J. Nucl. Mater.* 404 (2010) 97–108. doi:10.1016/j.jnucmat.2010.05.012.
- [21] C. Proff, S. Abolhassani, C. Lemaignan, Oxidation behaviour of zirconium alloys and their precipitates – A mechanistic study, *J. Nucl. Mater.* 432 (2013) 222–238. doi:10.1016/j.jnucmat.2012.06.026.

- [22] B. De Gabory, A.T. Motta, K. Wang, Transmission electron microscopy characterization of Zircaloy-4 and ZIRLO<sup>TM</sup> oxide layers, *J. Nucl. Mater.* 456 (2015) 272–280. doi:10.1016/j.jnucmat.2014.09.073.
- [23] J.H. Baek, Y.H. Jeong, Breakaway phenomenon of Zr-based alloys during a high-temperature oxidation, *J. Nucl. Mater.* 372 (2008) 152–159. doi:10.1016/j.jnucmat.2007.02.011.
- [24] B. Cox, V.G. Kristsky, C. Lemaignan, V. Polley, I.G. Ritchie, H. Ruhmann, V.N. Shishov, *Waterside corrosion of zirconium alloys in nuclear power plants*, Vienna, Austria, 1998.

CHAPTER FOUR: OXIDATION BEHAVIOR OF ZR-ALLOY CLADDING  
CANDIDATES FOR THE TREAT REACTOR

This chapter has submitted for publication in the Top Fuel 2019 conference proceedings.

Reference:

J.L. Vandegrift, C.M. Efaw, P.M. Price, C.J. Parga, D. Butt, B. Coryell, M. Hurley, and B.J. Jaques, "Oxidation Behavior of Zr-alloy Cladding Candidates for the TREAT Reactor" *Submitted to Top Fuel*. (2019).

## Oxidation Behavior of Zr-alloy Cladding Candidates for the TREAT Reactor

Jordan L. Vandegrift<sup>1,2</sup>

Corey M. Efaw<sup>1</sup>

Patrick M. Price<sup>1,2,3</sup>

Clemente J. Parga<sup>4</sup>

Darryl P. Butt<sup>1,2,5</sup>

Ben Coryell<sup>4</sup>

Michael F. Hurley<sup>1</sup>

Brian J. Jaques<sup>1,2</sup>

Submitted for publication in the conference proceedings of Top Fuel 2019

1. *Boise State University, 1910 University Dr., Boise, ID 83725*
2. *Center for Advanced Energy Studies, 995 University Blvd., Idaho Falls, ID 83401*
3. *Sandia National Laboratory, 1515 Eubank Blvd. SE, Albuquerque, NM 87123*
4. *Idaho National Laboratory, 2525 Fremont Ave, Idaho Falls, ID 83402*
5. *University of Utah, 201 Presidents Cir, Salt Lake City, UT 84112*

### 4.1 Abstract

The TREAT facility, located at the Idaho National Laboratory, is an air-cooled test facility designed to simulate rapid reactor transient conditions up to 600 °C. Zirconium and its alloys are known to undergo a transition from parabolic to linear oxidation kinetics,

termed “breakaway.” After breakaway, the oxide formed is porous and non-protective which significantly decreases its mechanical stability as a cladding material. In this work, the oxidation behavior of Zircaloy-3, Zircaloy-4, and Zr-1Nb is evaluated in isothermal and rapid transient conditions (air at  $\leq 820$  °C). Separate effects studies were done on plate samples in air (80% N<sub>2</sub>+O<sub>2</sub>) and oxygen (80% Ar+O<sub>2</sub>) to characterize the effect of nitrogen on the oxidation behavior during isothermal oxidation using thermogravimetric analysis. It was observed that the three alloys exhibit decreased resistance to breakaway in air. In addition, the effects of chamfering and welding on the oxidation behavior were investigated during isothermal and rapid transient oxidation. All alloys were affected by welding, however only the Fe/Sn containing alloys were affected by plastic deformation. Advanced characterization techniques (scanning Kelvin probe force microscopy and Raman spectroscopy) were performed on cross sections of oxidized specimens to further investigate the effects of oxide phase and composition on breakaway.

## 4.2 Introduction

The Transient Reactor Test (TREAT) facility located at the Idaho National Laboratory (INL) is designed to simulate transients and provide data on new fuel designs. TREAT has previously used Zircaloy-3 (Zry-3) cladding material, however Zry-3 is no longer commercially available, so an alternative zirconium alloy must be identified. Zirconium alloys are often used as nuclear fuel cladding material in light water reactors (LWRs) due to their favorable mechanical properties and corrosion resistance as well as their low absorption cross section for thermal neutrons [1]. The corrosion behavior of zirconium alloys is well studied in typical LWR conditions (i.e. 250-350 °C water) [1-3], however, less is reported on the oxidation behavior of zirconium alloys in air during

transient conditions. TREAT's conditions are unique in that the cladding is exposed to air during rapid transients where the core will be heated to 600 °C in approximately 1 second, with a design basis accident (DBA) temperature of 820 °C. At high temperatures ( $\geq 700$  °C), the oxidation kinetics have been shown to undergo a transition from parabolic to faster, linear kinetics. This transition is termed breakaway [1]. After breakaway, the oxide grows rapidly and results in the failure of the cladding material. Many factors have been reported to contribute to the breakaway phenomenon including: the oxidation of secondary phases, phase transformations in the oxide, and cracking of the oxide due to compressive stresses [4-9]. The relationship between the monoclinic to tetragonal phase transformation of  $ZrO_2$  and breakaway has been an area of interest. The transformation occurs at 1205 °C [10]. However, the compressive stresses generated during oxidation stabilize the tetragonal phase at lower temperatures [11,12]. During further oxidation and stress relaxation, the tetragonal grains undergo a martensitic transformation to a monoclinic structure, which results in a volume expansion [13]. The tetragonal to monoclinic phase transformation is thought to be a contributing factor to breakaway oxidation due to the associated porosity and crack formation [1,14]. Alloying elements added to improve the properties of zirconium can stabilize either the monoclinic or tetragonal phase, strongly influencing the oxidation behavior of the material.

Additionally, zirconium alloys have been shown to experience accelerated oxidation kinetics in air compared to water, oxygen, or steam [15-21]. The nitrogen present in air has been shown to catalyze the oxidation reaction via the nitridation and re-oxidation of zirconium [15-19,21,22]. Oxidation in air has also been shown to result in a more porous and cracked oxide compared to oxidation in non-nitrogen containing atmospheres. This is

attributed to the volume expansion of approximately 49% associated with the oxidation of ZrN [20,23,24]. Rather than a seamless tube geometry, TREAT's cladding geometry is a rectangular prism shape that includes chamfers and welded end caps. Welding and plastic deformation alter the microstructure of the base metal, which can directly impact the corrosion behavior of the alloy [25-31].

The work presented in this paper investigates the effects of TREAT's unique conditions on the oxidation behavior of two potential cladding candidates: Zircaloy-4 (Zry-4), and Zr-1Nb compared to the behavior of the legacy Zry-3 cladding. The effects of nitrogen, alloying elements, welding, plastic deformation, and rapid transients on the oxidation behavior are characterized between 400-820 °C.

### 4.3 Experimental Procedures

The cladding candidates investigated in this work are Zry-3, Zry-4, and Zr-1Nb.

The typical compositions for each of these alloys is shown below in Table 4.1.

**Table 4.1: Typical composition (wt%) of zirconium alloys investigated in this work [1].**

	Sn	Fe	Cr	O	Nb
Zry-3	0.25	0.25	-	-	-
Zry-4	1.4	0.2	0.1	0.12	-
Zr-1Nb	-	0.015-0.06	-	0.09-0.12	1

#### 4.3.1 Isothermal Oxidation

Isothermal oxidation experiments were performed in a NETZSCH STA-449 F3 Jupiter equipped with thermogravimetric analysis (TGA). A ramp rate of 20 °C/min with a 100 mL/min flow rate of ultra-high purity argon cleaned with a thermal oxygen getter was used during heating and cooling. 20-hour isothermal oxidation experiments were performed on plate samples (Figure 4.1a) to investigate the effect of nitrogen on the

oxidation behavior of Zry-3, Zry-4, and Zr-1Nb. The experiments were performed in two different atmospheres: 80% N<sub>2</sub>+O<sub>2</sub> (air) or 80% Ar+O<sub>2</sub> (oxygen). The details of this experiment have been previously described [32].

Specimens that are more representative of TREAT's unique cladding geometry were also studied. These specimens were tube-shaped and had welds and chamfers, as shown in Figure 4.1b. The tube samples had slightly different thicknesses: Zry-3 had a wall thickness of 0.63 mm, while Zry-4 and Zr-1Nb had thicknesses of 0.66 mm. The diameter of the tubes was approximately 16 mm. Prior to oxidation experiments, the internal stresses present from fabrication were removed via an annealing heat treatment of 450 °C for 24 hours under high vacuum (10<sup>-7</sup> torr). Isothermal oxidation experiments were performed in both dry and humid (P<sub>H2O</sub>=0.29 psi) air (flow rate of 100 mL/min) at 500, 600, 700, 800, and 820 °C. A platinum-mesh sample carrier that allowed both the inside and the outside of the tubes to be exposed to the oxidizing atmosphere was used. Two different weld types were investigated: electron-beam welding (EBW) and tungsten inert gas (TIG) welding. Additionally, the effect of the number of welds on the oxidation behavior was investigated, and samples that had two longitudinal EBWs were also oxidized. These samples are denoted (2-EBW). After isothermal oxidation, the oxide thickness of the tube samples was measured after oxidation at 700 °C and the average thicknesses at the weld, chamfer, and bulk (non-welded or plastically deformed) regions were compared.

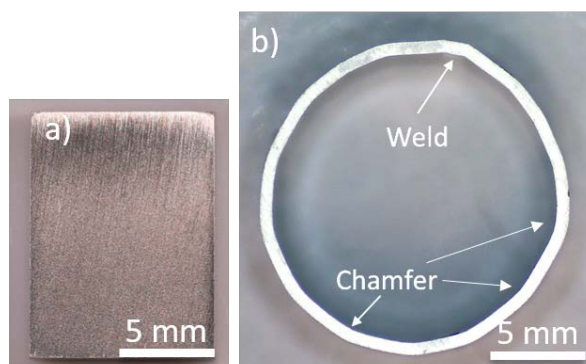


**Figure 4.1:** Specimen geometries investigated with isothermal oxidation: A) plate samples and B) welded and chamfered tubes representative of TREAT's cladding.

#### 4.3.2 Transient Oxidation

Transient oxidation experiments were performed on EBW tubes using either a benchtop muffle furnace or an induction furnace. The muffle furnace experiments consisted of fifteen normal operation transients up to 600 °C, followed by a DBA transient up to 820 °C. The experiments were conducted by first heating the furnace to the temperature of interest (either 600 °C or 820 °C) and allowing the furnace to equilibrate for approximately 45 minutes. The specimen along with a pure zirconium tube were inserted into the furnace through a port on the top. The pure zirconium tube had a thermocouple spot welded onto the surface to monitor the temperature during the experiment. Once the specimens reached the appropriate temperature, the furnace was cooled to either 500 °C or 450 °C before the specimens were removed and allowed to cool to room temperature. Images were taken of the specimens between each transient cycle.

Oxidation using an induction furnace included two successive transients up to 600 °C with a ramp rate of approximately 250 °C/s and a slow cooling rate of 4 °C/min down to 400 °C before the furnace was shut off and the specimen was rapidly cooled to room temperature using a prototypic TREAT cooling air flow of approximately 28 mph at the sample surface. Four thermocouples were spot welded to the inside of the tube, 90° apart,

to monitor temperature during the transient. Images were taken of the specimens between each transient.

#### 4.3.3 Raman and SKPFM Characterization

Raman spectroscopy and scanning Kelvin probe force microscopy (SKPFM) were performed on Zry-3 and Zry-4 plate samples after isothermal oxidation in 700 °C air on specimens both before and after the breakaway transition. The composition of the secondary phase precipitates as well as the monoclinic and tetragonal phases and internal stresses present at the metal/oxide interface were characterized. Raman spectroscopy was done using a Horiba LabRAM HR Evolution with a monochromatic 532 nm laser. Monoclinic (M) and tetragonal (T) phases were identified at the metal/oxide interface and the volume fraction of tetragonal phase was mapped according to Equation 1 which is the fraction of the intensities of the T<sub>1</sub> (262-287 cm<sup>-1</sup>) peak versus adjacent M<sub>3</sub> (220-224 cm<sup>-1</sup>), and M<sub>4</sub> (305-315 cm<sup>-1</sup>) Raman peaks [33]. Additionally, induced stresses at the metal/oxide interface were qualitatively related to shifts in the 381 cm<sup>-1</sup> M<sub>7</sub> peak. It has been shown that a linear relationship between peak shift and stress exists for corroded zirconium alloys, where a negative shift implies compressive stress while a positive shift corresponds to tensile stress [4,6].

$$\%T_{ZrO_2} = \frac{I(T_1)}{I(M_3)+I(T_1)+I(M_4)} * 100\% \quad (1)$$

SKPFM was used to produce Volta potential difference (VPD) maps of the materials, which can be related to the work function of a material to identify the composition of nanoscale-sized features. SKPFM has been used in the corrosion

community to characterize probable corrosion initiation sites; however, it has yet to be used to characterize zirconium alloys. Scanning electron microscopy (SEM) and energy-dispersive x-ray spectroscopy (EDS) were used to confirm the composition data obtained from SKPFM. The SKPFM maps were acquired using a Bruker Dimension Icon AFM in an argon atmosphere. A dual-pass method called frequency modulation PeakForce-Kelvin probe force microscopy (FM PF-KPFM) was used with PFQNE-AL probes (5 nm radius of curvature). The specific sample preparation procedures done prior to Raman and SKPFM have been previously described in another publication [34].

## 4.4 Results

### 4.4.1 Isothermal Oxidation

#### *4.4.1.1 Effect of Nitrogen (Plate Samples)*

Mass gain data (normalized to the initial surface area) measured during isothermal oxidation of Zry-3, Zry-4, and Zr-1Nb plate samples at 800 °C in either air or oxygen are shown in Figure 4.2. The corresponding macroscopic images of the specimens after oxidation are shown in Figure 4.3. It is clear from the two figures that all three alloys experience accelerated oxidation in the presence of nitrogen (air) compared to oxygen. From Figure 4.2, specimens oxidized in air experience the breakaway transition sooner than those oxidized in oxygen, resulting in more overall degradation.

This is also seen in Figure 4.3. The samples oxidized in air clearly have a thicker and more cracked oxide than those oxidized in oxygen. In the case of Zr-1Nb, the metal is almost completely corroded after air oxidation. At the oxidation temperatures where breakaway does not occur or is very minimal (400 and 600 °C), the effect of nitrogen on the oxidation behavior of the alloys is negligible. At 700 °C, where breakaway occurs but

is not as rapid as it is at 800 °C, breakaway also occurs slightly sooner in air than in oxygen. This effect is more apparent for the Fe and Sn containing alloys (Zry-3 and Zry-4) than for the Zr-1Nb alloy. At all temperatures and in both air and oxygen, Zry-4 had the fastest oxidation kinetics and exhibited breakaway the earliest of the three alloys, while Zr-1Nb resisted breakaway oxidation the longest.

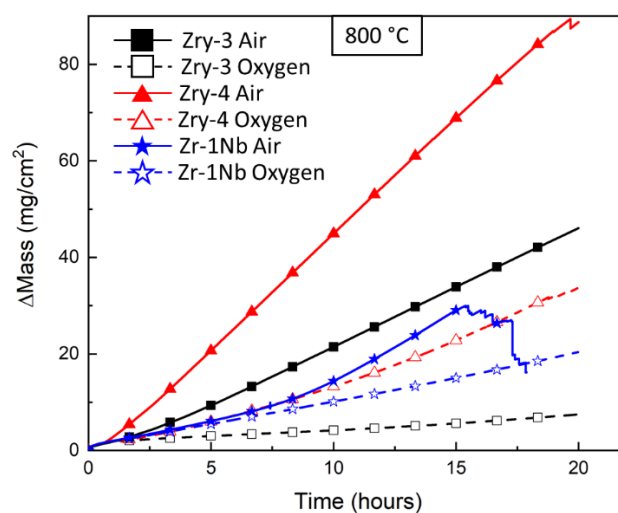


**Figure 4.2:** Normalized mass gain during isothermal oxidation of Zry-3, Zry-4, and Zr-1Nb plate samples at 800 °C in air (solid lines and closed symbols) or oxygen (dashed lines and open symbols).

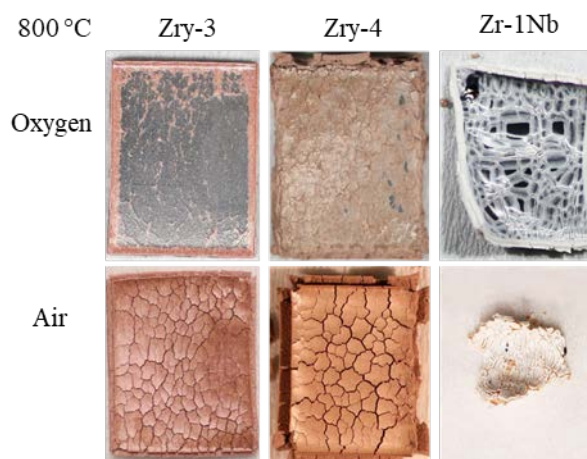


**Figure 4.3:** Macroscopic images of Zry-3, Zry-4, and Zr-1Nb plate samples after 20-hour isothermal oxidation at 800 °C in air or oxygen.

#### 4.4.1.2. *Effect of Welding, Plastic Deformation, and Humidity (Tube Samples)*

The mass gain normalized to initial surface area of the Zry-3, Zry-4, and Zr-1Nb welded tube specimens during isothermal oxidation at 800 °C in dry and humid air is shown in Figure 4.4. It is seen that the effect of weld type (EBW vs TIG) and number of welds (EBW vs 2-EBW) on the oxidation behavior of the alloys is more apparent in Zr-1Nb than Zry-3 and Zry-4. The Zr-1Nb EBW tubes exhibit slower oxidation kinetics than TIG and 2-EBW tubes, while all weld types had relatively similar oxidation kinetics in Zry-3 and Zry-4. A similar trend is seen at lower isothermal oxidation temperatures; however, it is most pronounced at 800 and 820 °C. As expected from oxidation of the plate samples, Zr-1Nb has the slowest oxidation kinetics and resists breakaway the longest, while the opposite is true for Zry-4. Additionally, the Zr-1Nb EBW tubes oxidized in humid air at temperatures 600 °C and above have slower oxidation kinetics than the EBW tubes oxidized in dry air. The Zry-3 and Zry-4 EBW tubes oxidized in humid air had similar oxidation kinetics to those oxidized in dry air, and no trend was noticeable. From Figure 4.5, which shows images of the samples after isothermal oxidation at 800 °C, it is clear that the Zr-1Nb EBW tube oxidized in humid air experienced less degradation compared to the other tubes oxidized in dry air. The dark, protective oxide is still visible between the network-like structure where the white accelerated oxidation occurred. It should be noted that the specimens in Figure 4.5 were oxidized for different periods of time to minimize spallation in the STA.

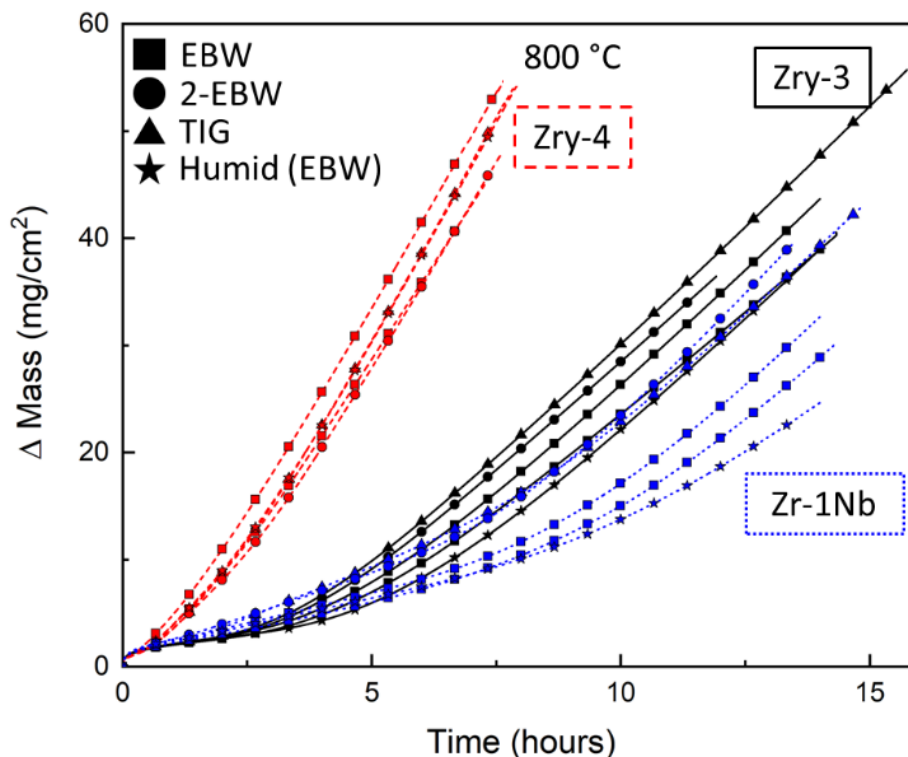


**Figure 4.4:** Normalized mass gain during isothermal oxidation of Zry-3, Zry-4, and Zr-1Nb EBW and TIG welded tubes in dry or humid air.

The effect of chamfering and welding on the oxidation behavior of the alloys can also be seen in Figure 4.5. In Zry-3, the oxidation behavior appears to be uniform across the sample, except for the weld region, where the oxide is slightly lighter in color. In the Zry-3 EBW tube oxidized in humid air, some of the dark pre-breakaway oxide can be seen in the weld region. The Zry-4 tubes clearly experienced accelerated oxidation at the chamfered regions, resulting in the specimens separating at those regions. Zr-1Nb appears to have a thicker oxide at the weld but is not affected by chamfering. The Zr-1Nb EBW tubes oxidized in dry air failed at the weld regions, while the TIG welded tube and EBW tube oxidized in humid air did not fail at the weld, however they clearly have a thicker oxide in that region.

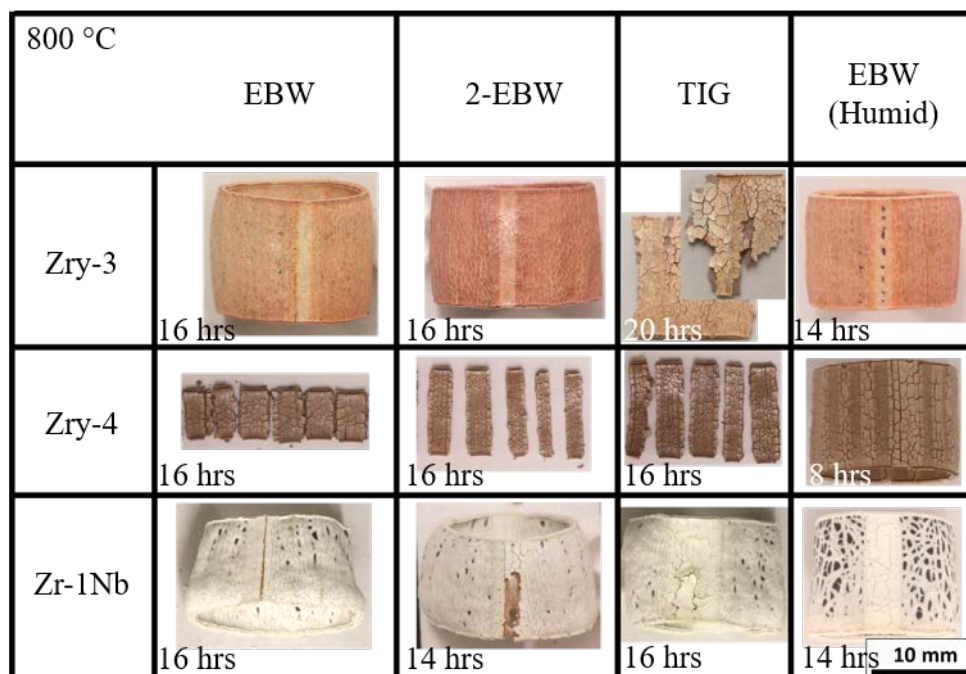


**Figure 4.5:** Macroscopic images of Zry-3, Zry-4, and Zr-1Nb welded tube specimens after isothermal oxidation at 800 °C in dry and humid air. The specimens were oxidized for different lengths of time to minimize spallation of the material inside the STA.

#### 4.4.2 Transient Oxidation

Images of EBW tubes after transient oxidation in the induction furnace and muffle furnace are shown in Figure 4.6. The images shown are Zry-3, Zry-4, and Zr-1Nb tubes after two 600 °C transients in the induction furnace, after fifteen 600 °C transients in the muffle furnace, and after fifteen 600 °C transients followed by an 820 °C transient in the muffle furnace. The transient oxidation behavior is similar to the isothermal oxidation behavior. Zry-3 has a relatively uniform oxide growth. There is a slightly lighter-colored oxide present on the chamfered regions after fifteen 600 °C and one 820 °C transient that may correspond to a slightly thicker oxide. Zry-4 experienced accelerated oxidation at the chamfers which is obvious from the images after the 600 °C transients. Zr-1Nb maintained its protective oxide during all 600 °C transients. After the 820 °C transient the specimens exhibit the same network-like structure of accelerated oxidation that was seen after

isothermal oxidation, although the network produced from transient oxidation is much finer than that seen after isothermal conditions. Accelerated oxidation at the weld region of Zr-1Nb is also present. No excessive oxide cracking or degradation as a result of rapid heating was noticed in either the induction furnace or the muffle furnace experiments.

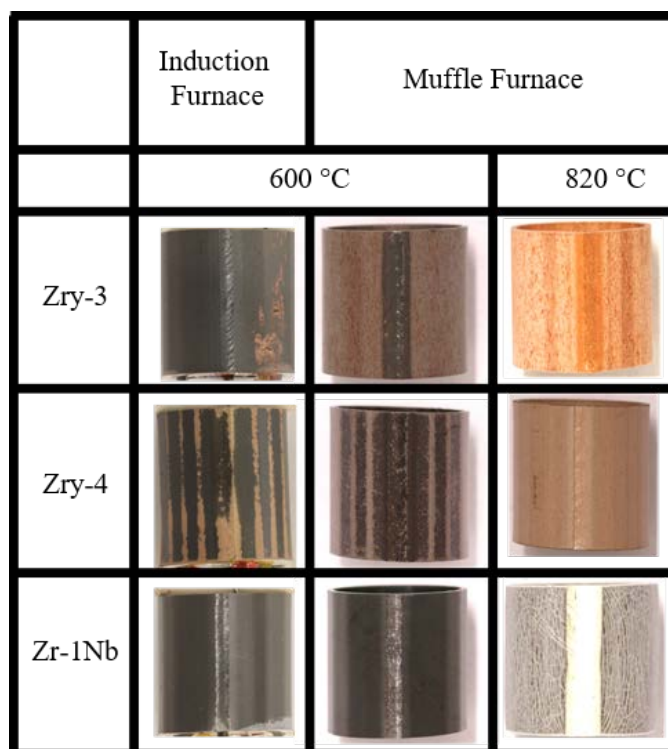


**Figure 4.6:** Images of Zry-3, Zry-4, and Zr-1Nb EBW tubes after transient oxidation experiments. The images in the left column are specimens after two successive rapid 600 °C transients in the induction furnace. The middle column shows specimens after fifteen 600 °C transients in the muffle furnace. The right column represents specimens after fifteen 600 °C transients and one 820 °C transient.

#### 4.4.3 Raman and SKPFM Characterization

The VPD map measured using SKPFM and corresponding EDS maps of oxidized Zry-3 after breakaway are shown in Figure 4.7. Clear correlations are seen (circled) between the potential differences identified in SKPFM and Fe precipitates in EDS.

Although this technique has been performed on both Zry-3 and Zry-4 before and after breakaway, only the Zry-3 post-breakaway data is shown here.

The corresponding SEM images, % tetragonality map, and stress map at the metal/oxide interface for Zry-3 and Zry-4 before and after breakaway are shown in Figure 4.8. It is clear in both samples that a tetragonal layer is present at the metal/oxide interface. The thickness of this layer decreases from pre- to post-breakaway. Additionally, the interface after breakaway is under more compression than before breakaway, particularly in the case of Zry-4.

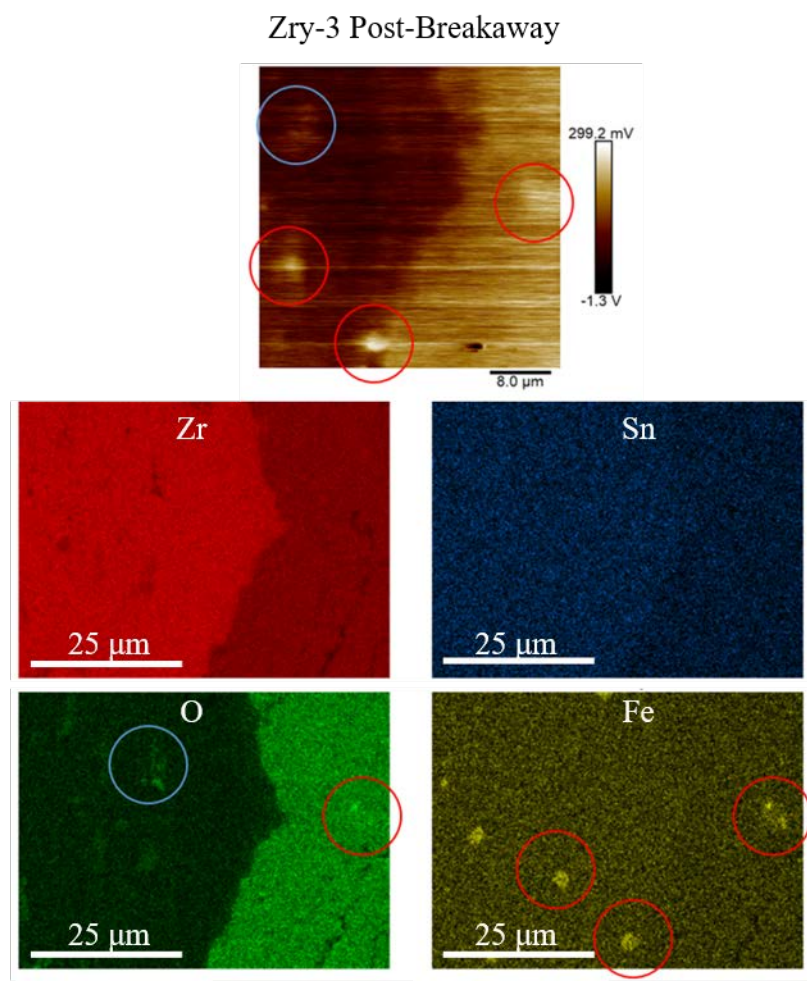


**Figure 4.7:** SKPFM mapping of oxidized Zry-3 after breakaway. Identified precipitates (Fe, Sn, and O) confirmed with EDS, where the intensity of the color in the map is proportional to the concentration of the element.

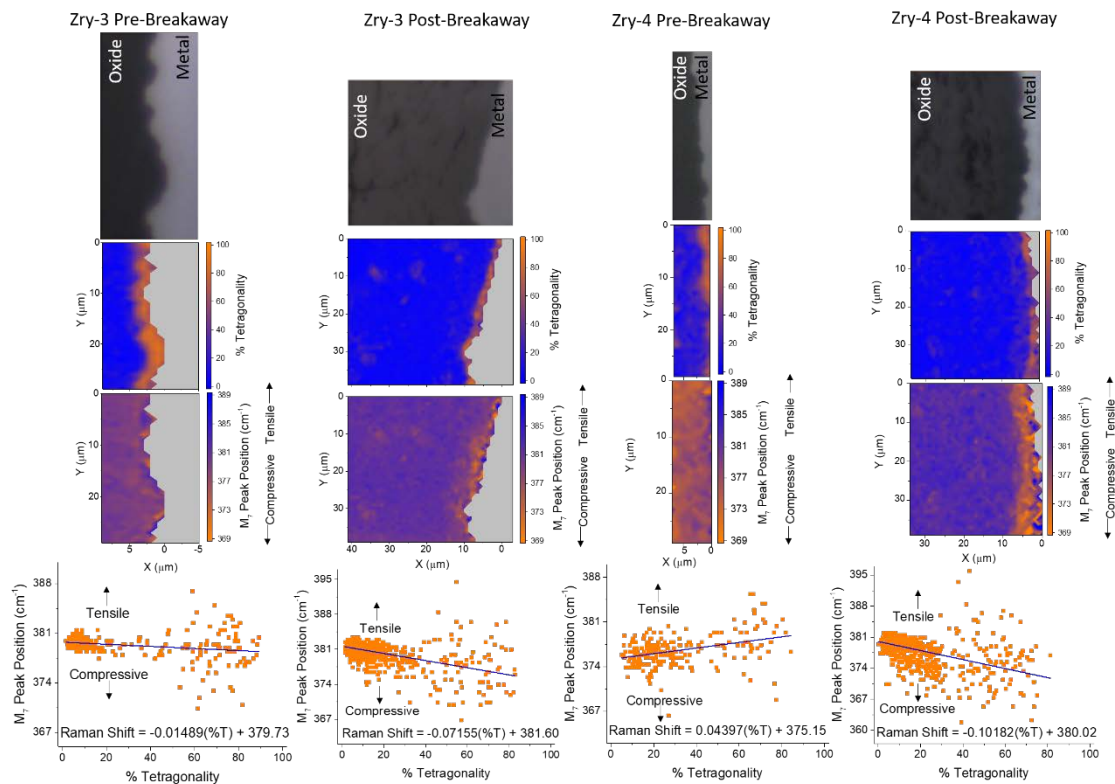


**Figure 4.8:** SEM image, % tetragonality map, and stress map at the metal/oxide interface of Zry-3 and Zry-4 oxidized at 700 °C in air to points before and after breakaway.

## 4.5 Discussion

### 4.5.1 Effect of Welding, Chamfering, and Alloying

As briefly discussed in the introduction and shown in Figure 4.2 and Figure 4.3, oxidation in a mixed nitrogen/oxygen atmosphere such as air leads to enhanced degradation of zirconium alloys. The mechanism by which this enhanced degradation occurs has been previously studied [22-24]. A ZrN phase has been found to form at the metal/oxide interface during oxidation. With further oxidation time, the ZrN oxidizes to form ZrO<sub>2</sub> via a rapid exothermic reaction that has an associated volume expansion of approximately 49%. Thus, the re-oxidation of ZrN at the interface causes cracking and porosity in the oxide which creates a direct path for oxygen anions to diffuse to the base metal. This

discussion is in agreement with what is seen in Figure 4.2 and Figure 4.3, as the breakaway transition occurs earlier and the oxide layer is more cracked and degraded after oxidation in air compared to oxygen.

It was shown that Zry-3 is relatively unaffected by chamfering and welding, Zry-4 experiences accelerated oxidation at chamfers and welds, and Zr-1Nb oxidizes more at the weld. The effect of chamfering and welding on the oxidation behavior of Zry-3, Zry-4, and Zr-1Nb was further characterized by measuring the average oxide thickness of the separate regions (chamfer, weld, and bulk) of tubes after 20-hour isothermal oxidation at 700 °C. The average thickness and standard deviation of the measurements are shown in Table 4.2. To obtain these values, oxidized samples were first polished from one end until a clear metal/oxide interface was clear ( $\approx 2$  mm). The entire cross-section was then imaged using an optical microscope and the oxide thicknesses were measured every 20  $\mu\text{m}$  using an image processing software. From these measurements, it is confirmed what is seen visually in Figure 4.5: the oxide thickness of Zry-3 is relatively uniform in all regions (within 10  $\mu\text{m}$ ), whereas the oxide at the chamfer and weld in Zry-4 is approximately 60  $\mu\text{m}$  ( $\approx 50\%$ ) thicker than the bulk region. However, the variation in oxide thickness between the weld and chamfer regions is statistically insignificant. Zr-1Nb has the same oxide thickness at the bulk and chamfer regions and a thicker oxide at the weld.

Furthermore, the TIG weld region in Zry-3 and Zry-4 has a thicker oxide than EBW. The Zr-1Nb EBW tube has the thickest oxide on all regions compared to the other specimens. This contradicts what is seen in the mass gain data, however the difference in oxide thickness is only about 10  $\mu\text{m}$  and is within the measurement error. Regarding the oxidizing atmosphere, Zry-3 and Zry-4 are relatively unaffected by the presence of nitrogen

and water. Zr-1Nb, however, grows an oxide that is double the thickness on the bulk and chamfer regions in dry air compared to humid air. The oxide thickness on the weld region is still comparatively the same as in dry air.

**Table 4.2: Average oxide thickness and standard deviation of sections of the welded tubes oxidized at 700 °C for 20 hours in dry or humid air.**

700 °C, 20 hours		Zry-3 ( $\mu\text{m}$ )	Zry-4 ( $\mu\text{m}$ )	Zr-1Nb ( $\mu\text{m}$ )
<b>EBW</b>	Bulk	$80 \pm 11$	$140 \pm 15$	$70 \pm 14$
	Chamfer	$100 \pm 11$	$200 \pm 21$	$70 \pm 10$
	Weld	$90 \pm 12$	$200 \pm 20$	$110 \pm 12$
<b>TIG</b>	Bulk	$90 \pm 11$	$120 \pm 13$	$60 \pm 11$
	Chamfer	$100 \pm 13$	$180 \pm 20$	$50 \pm 9$
	Weld	$120 \pm 12$	$220 \pm 30$	$100 \pm 12$
<b>2-EBW</b>	Bulk	$80 \pm 9$	$120 \pm 10$	$60 \pm 8$
	Chamfer	$90 \pm 8$	$180 \pm 17$	$60 \pm 10$
	Weld	$80 \pm 12$	$180 \pm 21$	$70 \pm 22$
<b>Humid (EBW)</b>	Bulk	$80 \pm 11$	$130 \pm 11$	$30 \pm 13$
	Chamfer	$80 \pm 9$	$190 \pm 15$	$30 \pm 10$
	Weld	$90 \pm 6$	$190 \pm 22$	$90 \pm 7$

#### 4.5.2 Effect of Oxide Phase and Stresses at Interface

As noted previously and seen in Figure 4.8, a tetragonal-rich layer is seen at the metal/oxide interface of Zry-3 and Zry-4 both before and after breakaway, as expected [35]. The thickness of the tetragonal layer decreases from pre- to post-breakaway, indicating that the tetragonal phase is being transformed to monoclinic as the compressive stress in the oxide relax with further oxidation [35]. These results are consistent with the oxidation model proposed by Wei et al., which states that higher Sn concentration (as in Zry-4) results in the stress stabilization of the tetragonal phase [9]. The tetragonal phase is also stabilized below a critical grain size, which is the mechanism for stabilization when the Sn concentration is reduced (as in Zry-3). As oxidation proceeds and the stress at the metal/oxide interface is reduced, the stress-stabilized tetragonal grains undergo a

martensitic transformation to monoclinic [13]. This rapid transformation causes damage in the oxide, and can reduce the alloy's resistance to breakaway [9]. This theory also corresponds to what is seen in the stress maps associated with post-breakaway Zry-3 and Zry-4 (Figure 4.8). While similar amounts of tetragonal phase are present at the interface of both alloys after breakaway, the tetragonal region in Zry-4 is under more compression than Zry-3. This indicates that the tetragonal phase in Zry-3 is also stabilized due to grain size, making it more resistant to the influence of the tetragonal to monoclinic phase transformation on breakaway than Zry-4.

The effect of secondary phase precipitates (SPPs) in the metal and oxide of zirconium alloys on the oxidation behavior of zirconium alloys has been characterized [7,8,36-39]. It has been reported that the SPPs can be categorized into two groups: those that oxidize at the same time as the matrix, and those that oxidize later, after being surrounded by the oxide. Those that exhibit delayed oxidation, such as Cr and Nb, can cause cracks in the oxide due to their increased Pilling-Bedworth (PB) ratio compared to  $ZrO_2$  (PB ratios;  $ZrO_2$ : 1.51,  $Cr_2O_3$ : 2.00, NbO: 1.37,  $NbO_2$ : 1.92,  $Nb_2O_5$ : 2.67) [7]. Additionally, Fe precipitates have been shown to act as nucleation sites for nodular corrosion on the surface of the metal, which leads to accelerated corrosion [8,36]. It is clear from Figure 4.7 that the feasibility of SKPFM as a viable characterization technique for identifying SPPs in the metal and oxide of zirconium alloys has been demonstrated. Further characterization with SKPFM will aid in the discussion of the influence of SPP composition and location on the oxidation behavior of zirconium alloys. The ability to detect nitride phases with SKPFM has been demonstrated on stainless steels [40-42]. The use of SKPFM to characterize the nitrides present in zirconium alloys after oxidation in air

could help further explain the accelerated oxidation kinetics exhibited in the presence of nitrogen containing atmospheres compared to oxygen or water.

#### 4.6 Conclusion

The oxidation behavior of three zirconium alloys: Zry-3, Zry-4, and Zr-1Nb was investigated in oxygen, dry air, and humid air. The effect of nitrogen on the oxidation behavior of these alloys was characterized as well as the effect of chamfering and welding via TIG or EBW. Additionally, the effect of the number of welds on the oxidation behavior was considered. The effect of rapid (transient) heating on the oxidation behavior was also investigated. The oxide phases and stresses at the metal/oxide interface of Zry-3 and Zry-4 before and after breakaway were characterized with Raman spectroscopy, while the SPPs at the interface were characterized by SKPFM and EDS. The following conclusions have been made:

- (1) *Effects of atmosphere and alloying:* Zry-3, Zry-4, and Zr-1Nb experience breakaway sooner in air than in oxygen, resulting in increased degradation in air. This has been reported to be due to the formation and re-oxidation of ZrN at the metal/oxide interface [22-24]. In all conditions, Zry-4 was the least resistant to breakaway and had the fastest oxidation kinetics. Zr-1Nb was the most resistant to breakaway and oxidized the least.
- (2) *Effects of chamfering and welding:* Zry-3 is relatively unaffected by chamfering and welding. Zry-4 experiences accelerated degradation at chamfers and welds that can induce failure in these regions. Zr-1Nb had accelerated oxidation at the weld region, particularly in the TIG welded sample.

(3) *Effects of rapid transient:* The transient oxidation behavior was similar to what was seen during isothermal oxidation, and no excessive cracking or degradation of the oxide was found.

(4) *Effect of oxide phase and stresses at the interface:* Raman spectroscopy identified a layer of tetragonal oxide phase present at the metal/oxide interface of both Zry-3 and Zry-4 before and after breakaway. This layer decreased in thickness between pre- and post-breakaway, indicating the transformation to monoclinic with increased oxidation. The improved breakaway resistance of Zry-3 over Zry-4 is likely due to the grain size-stabilization rather than stress-stabilization of the tetragonal phase as proposed by Wei et al. [9]. This is consistent with the increased compressive stresses seen at the Zry-4 interface after breakaway compared to Zry-3.

#### **4.7 Acknowledgements**

The work reported here was primarily funded through the Department of Energy's National Nuclear Security Administration (DOE-NNSA) Office of Materials Minimization and Management. This work was supported in part through the Department of Energy In-Pile Instrumentation program under DOE Idaho Operations Office Contract DE-AC07-05ID14517. The views and opinions of authors expressed herein do not necessarily state or reflect those of the U.S. Government or any agency thereof.

#### **4.8 References**

- [1] B. Cox, V.G. Kristsky, C. Lemaignan, V. Polley, I.G. Ritchie, H. Ruhmann, V.N. Shishov, Waterside corrosion of zirconium alloys in nuclear power plants, Vienna, Austria, 1998.

- [2] J.S. Moya, M. Diaz, J.F. Bartolomé, E. Roman, J.L. Sacedon, J. Izquierdo, Zirconium oxide film formation on zircaloy by water corrosion, *Acta Mater.* 48 (2000) 4749–4754. doi:10.1016/S1359-6454(00)00267-6.
- [3] N. Ni, D. Hudson, J. Wei, P. Wang, S. Lozano-Perez, G.D.W. Smith, J.M. Sykes, S.S. Yardley, K.L. Moore, S. Lyon, R. Cottis, M. Preuss, C.R.M. Grovenor, How the crystallography and nanoscale chemistry of the metal/oxide interface develops during the aqueous oxidation of zirconium cladding alloys, *Acta Mater.* 60 (2012) 7132–7149. doi:10.1016/j.actamat.2012.09.021.
- [4] L. Kurpaska, J. Favergeon, J. Grosseau-poussard, L. Lahoche, G. Moulin, In-situ stress analysis of the Zr/ZrO<sub>2</sub> system as studied by Raman spectroscopy and deflection test in monofacial oxidation techniques, *Appl. Surf. Sci.* 385 (2016) 106–112. doi:10.1016/j.apsusc.2016.05.074.
- [5] L. Kurpaska, J. Favergeon, Zirconia layer formed by high temperature oxidation of pure zirconium: Stress generated at the zirconium/zirconia interface, (2013) 261–277. doi:10.1007/s11085-012-9348-9.
- [6] L. Kurpaska, M. Kozanecki, J.J. Jasinski, M. Sitarz, Stress analysis of zirconia studied by Raman spectroscopy at low temperatures, *Spectrochim. Acta Part A Mol. Biomol. Spectrosc.* 131 (2014) 691–695. doi:10.1016/j.saa.2014.05.023.
- [7] C. Proff, S. Abolhassani, C. Lemaignan, Oxidation behaviour of zirconium alloys and their precipitates – A mechanistic study, *J. Nucl. Mater.* 432 (2013) 222–238. doi:10.1016/j.jnucmat.2012.06.026.
- [8] C. Proff, S. Abolhassani, M.M. Dadras, C. Lemaignan, In situ oxidation of zirconium binary alloys by environmental SEM and analysis by AFM, FIB, and TEM, *J. Nucl. Mater.* 404 (2010) 97–108. doi:10.1016/j.jnucmat.2010.05.012.
- [9] J. Wei, P. Frankel, E. Polatidis, M. Blat, A. Ambard, R.J. Comstock, The effect of Sn on autoclave corrosion performance and corrosion mechanisms in Zr – Sn – Nb alloys, *Acta Mater.* 61 (2013) 4200–4214.

- [10] P.Y. Chevalier, E. Fischer, B. Cheynet, Progress in the thermodynamic modelling of the O-U-Zr ternary system, *Comput. Coupling Phase Diagrams Thermochem.* 28 (2004) 15–40.
- [11] P. Bouvier, J. Godlewski, G. Lucazeau, A Raman study of the nanocrystallite size effect on the pressure – temperature phase diagram of zirconia grown by zirconium-based alloys oxidation, *J. N.* 300 (2002) 118–126.
- [12] S. Block, Pressure-temperature phase diagram of zirconia, *J. Am. Ceram. Soc.* 68 (1985) 497.
- [13] A. Heuer, M. Ruhle, On the nucleation of the martensitic transformation in zirconia, *Acta Metall.* 33 (1985) 2101–2112.
- [14] H.A. Porte, J.G. Schnizlein, R.C. Vogel, D.F. Fischer, Oxidation of zirconium and zirconium alloys, *J. Electrochem. Soc.* 107 (1960) 506–515.
- [15] M. Steinbrück, M. Böttcher, Air oxidation of Zircaloy-4, M5® and ZIRLO™ cladding alloys at high temperatures, *J. Nucl. Mater.* 414 (2011) 276–285. doi:10.1016/j.jnucmat.2011.04.012.
- [16] C. Duriez, D. Drouan, G. Pouzadoux, Reaction in air and in nitrogen of pre-oxidised Zircaloy-4 and M5™ claddings, *J. Nucl. Mater.* 441 (2013) 84–95. doi:10.1016/j.jnucmat.2013.04.095.
- [17] C. Duriez, T. Dupont, B. Schmet, F. Enoch, Zircaloy-4 and M5® high temperature oxidation and nitriding in air, *J. Nucl. Mater.* 380 (2008) 30–45. doi:10.1016/j.jnucmat.2008.07.002.
- [18] M. Lasserre, V. Peres, M. Pijolat, O. Coindreau, C. Duriez, J.P. Mardon, Qualitative analysis of Zircaloy-4 cladding air degradation in O<sub>2</sub>-N<sub>2</sub> mixtures at high temperature, *Mater. Corros.* 65 (2014) 250–259.
- [19] M. Steinbrück, Prototypical experiments relating to air oxidation of Zircaloy-4 at high temperatures, *J. Nucl. Mater.* 392 (2009) 531–544. doi:10.1016/j.jnucmat.2009.04.018.

- [20] E.T. Hayes, A.H. Roberson, Some effects of heating zirconium in air, oxygen, and nitrogen, *J. Electrochem. Soc.* 96 (1949) 142–151.
- [21] M. Steinbrück, J. Birchley, A.V. Boldyrev, A.V. Goryachev, M. Grosse, T.J. Haste, Z. Hózer, A.E. Kisselev, V.I. Nalivaev, V.P. Semishkin, L. Sepold, J. Stuckert, N. Vér, M.S. Veshchunov, High-temperature oxidation and quench behaviour of Zircaloy-4 and E110 cladding alloys, *Prog. Nucl. Energy.* 52 (2010) 19–36. doi:10.1016/j.pnucene.2009.07.012.
- [22] M. Steinbrück, S. Schaffer, High-temperature oxidation of Zircaloy-4 in oxygen-nitrogen mixtures, *Oxid. Met.* 85 (2016) 245–262. doi:10.1007/s11085-015-9572-1.
- [23] E. Beuzet, J.S. Lamy, A. Bretault, E. Simoni, Modelling of Zry-4 cladding oxidation by air, under severe accident conditions using the MAAP4 code, *Nucl. Eng. Des.* 241 (2011) 1217–1224. doi:10.1016/j.nucengdes.2010.04.024.
- [24] J. Stuckert, Z. Hózer, A. Kiselev, M. Steinbrück, Cladding oxidation during air ingress. Part I: experiments on air ingress, *Ann. Nucl. Energy.* 93 (2016) 4–17. doi:10.1016/j.anucene.2015.12.034.
- [25] Y.H. Jeong, K. Ok, H.G. Kim, H.G. Jeong, Y. H., Lee, K. O., Kim, Y.H. Jeong, K. Ok, H.G. Kim, Correlation between microstructure and corrosion behavior of Zr – Nb binary alloy, *J. Nucl. Mater.* 302 (2002) 9–19. doi:10.1016/S0022-3115(02)00703-1.
- [26] C. Cai, L. Li, W. Tao, G. Peng, X. Wang, Weld bead size, microstructure and corrosion behavior of zirconium alloys joints welded by pulsed laser spot welding, *J. Mater. Eng. Perform.* 25 (2016) 3783–3792. doi:10.1007/s11665-016-2250-x.
- [27] K.Y. Huang, The effect of heat treatment on the microstructure and the corrosion resistance of Zircaloy-4 in 450 °C steam, *J. Nucl. Mater.* 136 (1985) 16–29.
- [28] B. Zhang, X. Li, T. Wang, X. Wang, Microstructure and corrosion behavior of Zr-702 joined by electron beam welding, *Vacuum.* 121 (2015) 159–165. doi:http://dx.doi.org/10.1016/j.vacuum.2015.08.005.

- [29] A.Y. Eroshenko, A.M. Mairambekova, Y.P. Sharkeev, Z.G. Kovalevskaya, M.A. Khimich, P. V Uvarkin, Structure, phase composition and mechanical properties in bioinert zirconium-based alloy after severe plastic deformation, *7* (2017) 469–472.
- [30] S.O. Rogachev, S.A. Nikulin, A.B. Rozhnov, M. V Gorshenkov, Microstructure, phase composition, and thermal stability of two zirconium alloys subjected to high-pressure torsion at different temperatures, *Adv. Eng. Mater.* *20* (2018). doi:10.1002/adem.201800151.
- [31] D. Fuloria, N. Kumar, R. Jayaganthan, S.K. Jha, D. Srivastava, An investigation of effect of annealing at different temperatures on microstructures and bulk textures development in deformed Zircaloy-4, *Mater. Charact.* *129* (2017) 217–233. doi:10.1016/j.matchar.2017.04.038.
- [32] J.L. Vandegrift, P.M. Price, J.P. Stroud, C.J. Parga, I.J. Van Rooyen, B.J. Jaques, D.P. Butt, Oxidation behavior of Zirconium, Zircaloy-3, Zircaloy-4, Zr-1Nb, and Zr-2.5Nb in air and oxygen, *Nuclear Materials and Energy.* (2019). doi:10.1016/j.nme.2019.100692.
- [33] K.B. Chong, M.E. Fitzpatrick, Evolution of stress fields and phase content in corroded zirconium cladding materials, *Surf. Coat. Technol.* *324* (2017) 140–145. doi:10.1016/j.surfcoat.2017.05.072.
- [34] C.M. Efaw, M. Reynolds, J.L. Vandegrift, K. Smith, Y. Wu, B.J. Jaques, H. Hu, C. Xiong, M.F. Hurley, Determination of zirconium oxide chemistry through complementary characterization techniques, in: *Top Fuel*, 2019.
- [35] W. Gong, H. Zhang, Y. Qiao, H. Tian, X. Ni, Z. Li, X. Wang, Grain morphology and crystal structure of pre-transition oxides formed on Zircaloy-4, *Corros. Sci.* *74* (2013) 323–331. doi:10.1016/j.corsci.2013.05.007.
- [36] C. Proff, S. Abolhassani, C. Lemaignan, Oxidation behaviour of binary zirconium alloys containing intermetallic precipitates, *J. Nucl. Mater.* *416* (2011) 125–134. doi:10.1016/j.jnucmat.2010.11.099.

- [37] J.H. Baek, Y.H. Jeong, Breakaway phenomenon of Zr-based alloys during a high-temperature oxidation, *J. Nucl. Mater.* 372 (2008) 152–159. doi:10.1016/j.jnucmat.2007.02.011.
- [38] B. de Gabory, A.T. Motta, K. Wang, Transmission electron microscopy characterization of Zircaloy-4 and ZIRLO<sup>TM</sup> oxide layers, *J. Nucl. Mater.* 456 (2015) 272–280. doi:10.1016/j.jnucmat.2014.09.073.
- [39] K.N. Choo, Effect of composition and heat treatment on the microstructure and corrosion behavior of Zr-Nb alloys, (n.d.). doi:10.1111/cpr.12282.
- [40] C. Örnek, D.L. Engelberg, Correlative EBSD and SKPFM characterisation of microstructure development to assist determination of corrosion propensity in grade 2205 duplex stainless steel, *J. Mater. Sci.* 51 (2016) 1931–1948. doi:10.1007/s10853-015-9501-3.
- [41] N. Sathirachinda, R. Pettersson, S. Wessman, J. Pan, Study of nobility of chromium nitrides in isothermally aged duplex stainless steels by using SKPFM and SEM/EDS, *Corros. Sci.* 52 (2010) 179–186. doi:10.1016/j.corsci.2009.08.057.
- [42] N. Sathirachinda, R. Pettersson, S. Wessman, U. Kivisäkk, J. Pan, Scanning Kelvin probe force microscopy study of chromium nitrides in 2507 super duplex stainless steel — Implications and limitations, *Electrochim. Acta.* 56 (2011) 1792–1798. doi:10.1016/j.electacta.2010.08.038.

## CHAPTER FIVE: CONCLUSIONS

The work presented here investigated the oxidation behavior of zirconium alloy cladding material in conditions that the core of the TREAT reactor would experience during transient testing and DBA scenarios. Along with contributing unique studies to the literature base on the oxidation behavior of cladding materials, the goal of this work was to identify a zirconium alloy suited for fuel cladding in the extreme conditions produced by the TREAT facility (air-cooled, rapid transients, operating temperature up to 600 °C). The oxidation behavior of zirconium alloys is not well studied in TREAT's conditions and no direct comparison of the alloys of interest are presented in literature. The work presented in the previous chapters provides a direct comparison of the oxidation behavior of candidate zirconium alloy cladding materials. Chapter Two investigated the effects of air on the oxidation behavior of pure Zr, Zry-3, Zry-4, Zr-1Nb, and Zr-2.5Nb. It was found that the Sn and Fe containing alloys (Zry-3, and Zry-4) were more affected by the presence of nitrogen in the oxidizing atmosphere than the Nb alloys and had faster oxidation kinetics in air than in oxygen. Zr-1Nb and Zry-3 were the most resistant to breakaway oxidation (transition from parabolic to linear kinetics), while Zry-4 and Zr-2.5Nb experienced breakaway quickly, resulting in faster degradation.

Chapter Three focused on the effects of TREAT's unique cladding geometry, humidity, and the effect of rapid heating on the oxidation behavior of Zry-3, Zry-4, and Zr-1Nb. Chamfered and welded (TIG and EBW) tubes were oxidized in isothermal conditions in dry and humid air. EBW tubes were also oxidized in air under transient

heating conditions. Zry-4 was the most effected by chamfering and welding, exhibiting accelerated oxidation in those regions. Zry-3 was the least affected by these conditions and had similar oxide thickness in the weld, chamfer, and bulk of the tube after oxidation at 700 °C. At higher temperatures, however, it becomes apparent that accelerated oxidation occurs at the chamfers and welds. Zr-1Nb had a thicker oxide at the weld than the rest of the tube. Again, Zry-4 was found to be the least resistant to breakaway oxidation while Zr-1Nb was the most resistant. Of the two weld types, the EBW Zr-1Nb tube was found to exhibit the slowest oxidation kinetics.

Chapter Four covers the effect of nitrogen, chamfering, welding, and rapid transients on the oxidation behavior of Zry-3, Zry-4, and Zr-1Nb, and investigates the effect of oxide phase and stresses at the metal/oxide interface. Accordingly, it is summarized that Zr-1Nb experiences the slowest oxidation kinetics and is the least effected by the presence of nitrogen in the oxidizing atmosphere, and the EBW tube resists breakaway oxidation the longest. Additionally, Raman spectroscopy and SKPFM identified that a layer of tetragonal-rich oxide exists at the metal/oxide interface of Zry-3 and Zry-4 both before and after breakaway oxidation. When compared to literature, it is likely that the resistance to breakaway of Zry-3 over Zry-4 is likely due to the increased transformation from tetragonal to monoclinic zirconium oxide in Zry-4 during oxidation. The transformation has been shown to be martensitic in nature and result in porosity and cracks in the oxide, which causes increased degradation.

From this work, it is clear that the oxidation behavior of zirconium alloys is dependent on the oxidizing conditions and material processing. This work has expanded the knowledge about the behavior zirconium alloy nuclear fuel cladding material during

transient or failure conditions, which is necessary to further the development of accident tolerant cladding. With these studies, it was found that Zr-1Nb exhibited the most favorable oxidation behavior in simulated TREAT conditions. The experiments realized with the TREAT facility will be instrumental in designing and testing accident tolerant fuels and make harnessing nuclear energy safer and more efficient.

## APPENDIX

### **Determination of Zirconium Oxide Chemistry Through Complementary Characterization Techniques**

## Determination of Zirconium Oxide Chemistry Through Complementary Characterization Techniques

Submitted for publication in the conference proceedings of Top Fuel 2019

Reference:

C.M. Efaw, M. Reynolds, J.L. Vandegrift, K. Smith, Y. Wu, B.J. Jaques, H. Hu, C. Xiong, M.F. Hurley, "Determination of Zirconium Oxide Chemistry Through Complementary Characterization Techniques." *Submitted to Top Fuel*. (2019).

### A.1 Abstract

Nuclear energy has been increasingly recognized as an effective and low carbon-emission energy source. Though low in probability, nuclear reactors are susceptible to adverse effects that can lead to potentially severe consequences. To ensure safety and improved monitoring of reactors, there have been increasing interests in developing sensors to monitor key parameters relating to the status within a reactor. In order to improve sensor accuracy, high-resolution characterization of cladding materials can be utilized to correlate with sensor output. A common issue with zirconium cladding is the so-called "breakaway phenomenon", a critical factor seen as the transition from an initially passive zirconia to an active material. Existing research presents many factors that contribute to the breakaway mechanism, ultimately resulting in difficulty to predict its activation and propagation. As part of the effort to develop sensors, an improved understanding of pre- and post-breakaway zirconium alloys (Zr, Zr-2.65Nb, Zry-3, and Zry-4) is accomplished with

Raman spectroscopy, scanning Kelvin probe force microscopy, and atom probe tomography.

## A.2 Introduction

Within a nuclear core, uranium-based fuels release multiple high energy neutrons by fission and cause a chain reaction, generating useable energy for our society's ever-increasing power demands. To allow a fission chain reaction to occur unperturbed and generate energy efficiently, a cladding material encapsulates the fuel, preventing highly radioactive fission products from escaping into the surrounding coolant. Zirconium is a viable material choice for cladding due to its low neutron absorption cross-section, high mechanical strength, and strong corrosion resistance while in an extreme environment [1]. Alloying of zirconium has been shown to increase cladding performance by improving mechanical properties and corrosion resistance in high-temperature water [2-6].

It has been found that the general high-temperature oxidation mechanisms for zirconium cladding are similar regardless of oxidizing media (oxygen, air, water, or steam) [7]. Initial formation of the oxide film provides a passivating film, thus slowing the rate of oxidation to follow empirical power-law with parabolic to sub-parabolic characteristics (exponent,  $n \leq 0.5$ ). Here, the kinetics are limited by diffusion of corrosion species to the metal/oxide interface [8]. However, it has been found that cracks develop within the oxide, providing pathways for species to reach the base metal at an increased rate. This is observed as a transition in mass growth, progressing to an increased oxidation rate [8-11]. This is commonly termed as the "breakaway phenomenon" [9]. Some alloying elements support cyclic transition between passivation and oxidation, while others fail to recover from the

first breakaway. Regardless, continuous oxidation of the metal eventually leads to failure of the cladding material [9,10].

Though this general trend is seen regardless of coolant environment, there are additional effects that contribute to cladding failure at unpredictable points in time. Addition of hydrogen species in the coolant has been shown to cause cladding embrittlement by dendrite-like precipitation in the metal [2,12,13]. Inclusion of nitrogen species has been found to advance the breakaway phenomenon by creating defects and lattice mismatch in the oxide, thus permitting increased oxygen diffusion to the base metal [14-21]. Additional effects such as high compressive stresses [10,22-27], zirconia phase content [16,17,20,28-30], sub-stoichiometry of the oxide [7,15-17], operating temperature [31-34], and alloying dopants [2,8,12,24,25,35] are all believed to play a role in cladding failure. Additional contributions from the fuel/cladding interface, such as fuel swelling [36], fuel fracture [37], and stress corrosion cracking lead to unpredictable cladding lifetime, as well as decreased energy efficiency. The complexity of differing effects presents a difficult problem to predict cladding failure, and thus has been a major focus of nuclear research.

Presently, chemical evolution over the lifetime of the fuel and cladding inside a nuclear reactor can only be inferred using post-irradiation examination (PIE) [38]. Due to the adverse environment created from harsh ambient conditions and irradiation, the corrosion mechanisms of cladding are difficult to observe in-core or effectively mimic through experimentation. This limitation presents a significant obstacle for achieving a comprehensive and unified understanding of cladding degradation mechanisms. Progress is being made to establish a new sensing technique by monitoring cladding and fuels in-

core with electrochemical impedance spectroscopy (EIS). Predicted EIS modelling of the corrosion mechanisms can be confirmed with the use of high-resolution characterization techniques, thus providing feasibility of new sensor technology. This work utilizes Raman spectroscopy, scanning Kelvin probe force microscopy (SKPFM), and atom probe tomography (APT) to provide high-resolution characterization of zirconium metal/oxide interfaces. With improved understanding of these techniques, their usability can expand to support EIS sensor technology for in-core operation.

### A.3 Experimental Methods

Zirconium (Goodfellow) and its alloys Zr-2.65Nb (ATI Metals), Zry-3, and Zry-4 (Idaho National Laboratory) were chosen for the current work (Table A.1) Samples were isothermally oxidized in a NETZSCH STA-449 F3 Jupiter equipped with thermogravimetric analysis (TGA). Prior to oxidation, samples were prepared by electronic discharge machining (EDM). This was followed by grinding of samples up to 1200 grit SiC and then sonication in 1:1:1 acetone:ethanol:DI solution.

**Table A.1: Zirconium alloy compositions.**

	Zr (ppm)	Zr-2.65Nb (wt. %)	Zry-3 (wt. %)	Zry-4 (wt. %)
Sn	-	-	0.25	1.4
Fe	200	0.061	0.25	0.2
Cr	200	-	-	0.1
Nb	-	2.62	-	-
C	250	-	-	-
Hf	2500	-	-	-
O	1000	0.106	-	0.12
N	100	-	-	-
H	10	-	-	-

Isothermal oxidation of the samples was done at 700 °C in 80% N<sub>2</sub>, 20% O<sub>2</sub> environment. Samples were heated and cooled between RT and 700 °C at a 20 °C/<sub>min</sub> ramp

rate. Samples were held in an alumina crucible to allow for oxidation of maximum surface area.

After oxidation, samples were sectioned and mounted in epoxy. They were then ground with SiC up to 1200 grit, followed by polishing with 1 and 0.05  $\mu\text{m}$  alumina slurries. Following polishing, samples were cleaned with Alconox solution on a soft pad, rinsed with ultrapure water, and then air dried. SEM with a Hitachi S-3400N-II (Oxford Instruments Energy+) at 10 keV and 10 mm working distance was performed on each alloy to determine approximate oxide thicknesses.

Raman spectroscopy was accomplished using a Horiba LabRAM HR Evolution (Horiba Scientific) with a monochromatic 532 nm laser. Spectral range of 150-700  $\text{cm}^{-1}$  was used to examine peaks of interest. Spectra were processed via LabSpec6 with a 'normal variate' normalization, a baseline correction to remove background, and DeNoise smoothing and filtering to enhance spectra. Peak analysis was accomplished with Gaussian-Lorentzian fitting.

SKPFM mapping was done with a Bruker Dimension Icon AFM (Bruker) in an argon filled glovebox. SKPFM is an atomic force microscope (AFM)-variant used to detect the Volta potential difference (VPD) at the nano-scale. PFQNE-AL probes were used to acquire results, operating under a dual-pass method called FM PF-KPFM. The first pass of this method employs PeakForce (PF, Bruker) tapping of the probe at 2 kHz frequency to acquire topographical variations of the surface. Upon completion of a trace and retrace line of topography, the probe lifts off the surface and traces the line of topography at a user-defined lift height of 100 nm, creating a nano-scale scenario synonymous to the traditional Kelvin probe. During this second pass, VPD between probe and surface is measured via

probe frequency modulation (FM). This process is repeated line-by-line until a complete map of both topography and relative Volta potential are acquired. Prior to SKPFM mapping of different zirconium alloys, probes were calibrated with a Bruker PFKPFM-SMPL, consisting of n-doped silicon substrate with patterned islands of aluminum surrounded by a gold interconnect. This sample was utilized to ensure relative consistency of probes by providing a step-wise VPD map from gold to silicon to aluminum. [39] Image processing and analysis were conducted using NanoScope Analysis V1.8 (Bruker). Topography maps underwent a flattening process to remove sample tilt.

APT tips were produced with a dual beam FIB/SEM (FEI Quanta 3D FEG) and analyzed with a Local Electrode Atom Probe (LEAP) (CAMECA LEAP 4000X HR). Tips were collected from the metal/oxide interface, revealing atomistic make-up of the few 10s of surrounding nanometers.

## A.4 Results and Discussion

### A.4.1 Thermogravimetric Analysis

TGA provided observable mass gain rate, and subsequently oxidation rate, for zirconium and its alloys. Pre- and post-breakaway samples were confirmed with TGA (Figure A.1). SEM provided relative thickness of the oxide grown on each sample, as described in Table A.2.

**Table A.2: Approximate oxide thickness of each sample, pre- and post-breakaway, to the nearest 5  $\mu\text{m}$ .**

	Oxide Thickness ( $\mu\text{m}$ )			
	Zr	Zr-2.65Nb	Zry-3	Zry-4
Pre-break	20	25	10	5
Post-break	100	50	35	30

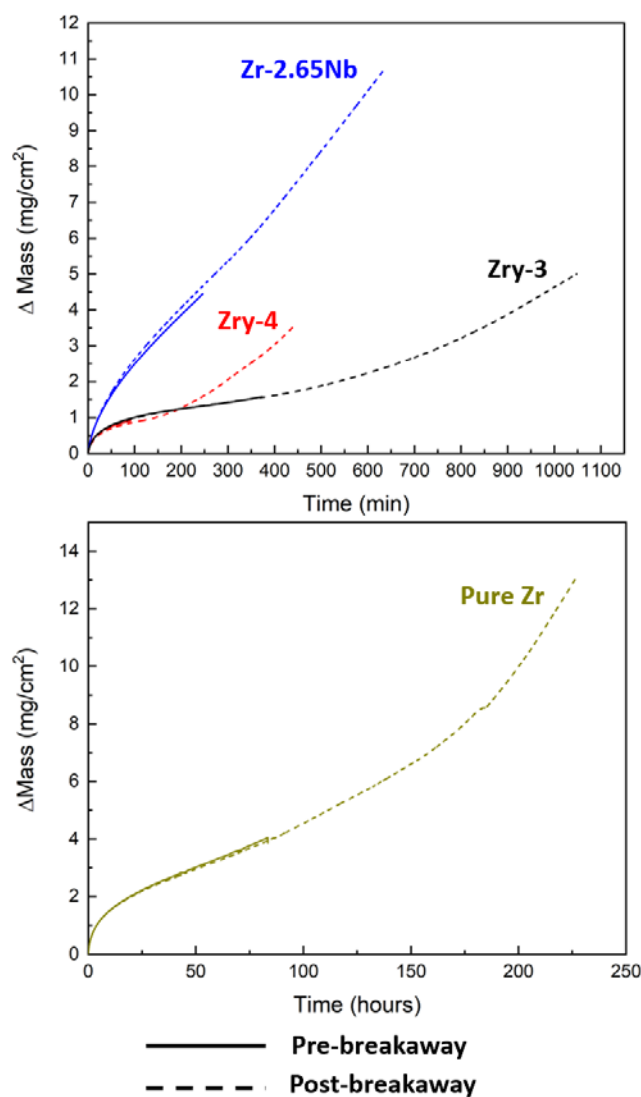


**Figure A.1:** TGA results for each zirconium alloy, pre-breakaway designated with solid lines, post-breakaway with dotted lines.

#### A.4.2 Raman Spectroscopy

Raman provides qualitative to semi-quantitative information on the material composition seen in oxides. The Raman spectra of common zirconium-based polymorphs have been extensively covered [16,17,20,23-26,28,29,40-46]. Distinct peaks have been well established for both monoclinic and tetragonal zirconia [14,18,22,24,26,40,42-44]. In particular, Table A.3 describes specific peak positions used in this study. The wide ranges in the tetragonal peak position has been attributed to high compressive stresses observed

near the metal/oxide interface, at times even causing distinction between a “relaxed” tetragonal phase and an “interface” tetragonal phase [16,20,27].

**Table A.3: Notable tetragonal (T) and monoclinic (M) zirconia Raman peak positions [16,20,25,27,29,44,46-48].**

Attribution	Peak Position (cm <sup>-1</sup> )
M <sub>3</sub>	220-224
T <sub>1</sub>	262-287
M <sub>4</sub>	300-310
M <sub>7</sub>	380-384

There has been much discussion about the relationship between the presence of tetragonal zirconia and the stress state. Tetragonal zirconia is thermodynamically stable above 1205 °C [49], but can be stabilized at lower temperatures by high compressive stress near the metal/oxide interface [50]. Therefore, presently, regions of scale with high tetragonal concentration near the metal/oxide interface should coincide with high compressive stresses. The understanding of this correlation is important, as prior efforts have led to a belief that the formation of tetragonal phase relates to alloy passivity, porosity, and crack formation.

Content of tetragonal phase (i.e., “percent tetragonality”) has been estimated as a volume fraction of tetragonal peak intensity versus monoclinic peaks (Equation 1). Different forms of Equation 1 have been used in literature to determine percent tetragonality [10,27,29,51,52]. The T<sub>1</sub> peak is commonly seen as the most intense tetragonal peak, and thus the T<sub>1</sub> peak versus its adjacent monoclinic peaks (M<sub>3</sub> and M<sub>4</sub>) was adopted for calculating percent tetragonality in this work.

$$\%T_{ZrO_2} = \frac{I(T_1)}{I(M_3)+I(T_1)+I(M_4)} \times 100\% \quad (1)$$

As for the stress-state, stress development of zirconia has been covered for more than 50 years [9,10,22-27,53]. In particular, Raman spectroscopy has been utilized to observe oxide scales both during heating of a sample [23-25], as well as with post-exposure examination of sectioned oxides. The stress presented from post-exposure Raman analysis is defined as a residual stress, which comprises of growth, thermal, and relaxation contributions to the stress state [22]. Residual stress is commonly observed by shifts from non-stressed Raman peak positions, where certain peaks are more reliable than others during calibration. Using Raman, residual stress has been calculated between hundreds of MPa to more than 5 GPa at the metal/oxide interface [22]. In one instance, Chong and Fitzpatrick discussed the feasibility of the  $M_7$  peak for residual stress calculation, warranted by a calibrated peak shift arising from uniaxial compression applied to laboratory-prepared monoclinic zirconia [10]. In general, a direct correlation between shift from expected peak position and residual stress has been shown, where a positive peak shift coordinates to tensile stress and a negative peak shift coordinates to compressive stress [10]. For this work, residual stress is qualitatively observed as a shift from expected  $M_7$  peak position at  $381 \text{ cm}^{-1}$ .

Percent tetragonality and peak shift (as it relates to residual stress) were observed with Raman of pre- and post-breakaway oxides of zirconium and its alloys. Figure A.2 presents these two parameters as a function of distance from the metal/oxide interface of a pre-breakaway Zr sample. The tetragonal-rich region near the metal/oxide interface is clearly seen. The  $T_1$  peak slowly transitions to greater wavenumbers as the distance from the metal/oxide interface increases, until finally it is not visible at the  $6 \text{ }\mu\text{m}$  spectra and

beyond. This corresponds to a rapid decrease in percent tetragonality as the distance from the interface increases. Likewise, a highly compressive stress, relating to a negative shift in the  $M_7$  peak position, is seen near the interface, with the bulk of the oxide expressing a peak shift within a  $\text{cm}^{-1}$  of the “non-stressed” expected position. Additionally, from this line scan the percent tetragonality and the relative residual stress were compared. The fit of the line scan data displays a general trend where an increase in tetragonality corresponds to an increasingly compressive residual stress, which is in agreement with previous works. However, statistically speaking this linear trend does not fit well to a data, as there is notable scatter.

This concept of statistically comparing residual stress to percent tetragonality can be expanded from an individual line scan to a full Raman map. Figure A.3 presents this idea, observing both the percent tetragonality and  $M_7$  peak position over a  $25 \times 40 \mu\text{m}$  area. Tetragonal-rich zirconia can be seen in the few microns nearest the metal/oxide interface, with the bulk of the oxide showing majority monoclinic phase. The trend of  $M_7$  peak position as a function of percent tetragonality for a full map is similar to that of the line scan, where an increase in tetragonality is correlated to a decreasing  $M_7$  peak position, and thus greater compressive stress. Again, though this trend is in agreement with previous works, the data does not appear to fit well to a linear trend. This is especially noticeable when looking at the far right of the plot, where volume fraction of the zirconia is predominantly tetragonal. The distribution for highly tetragonal spectra is large, ranging nearly  $20 \text{ cm}^{-1}$  in peak position.

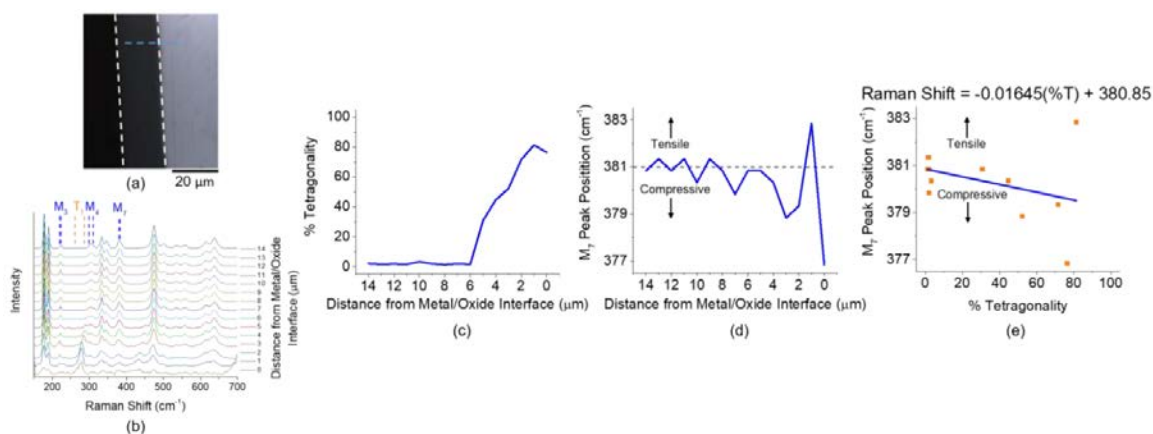


**Figure A.2:** (a) Optical image of pre-breakaway Zr sectioned sample. White lines separate (left) epoxy/oxide and (right) oxide/metal interfaces. Blue line displays collected Raman line scan. (b) Spectra from collected Raman line scan, with notable peak ranges presented. (c) Percent tetragonality and (d) position of the  $M_7$  peak as a function of distance from the metal/oxide interface. (e) Percent tetragonality as a function of the  $M_7$  peak position.

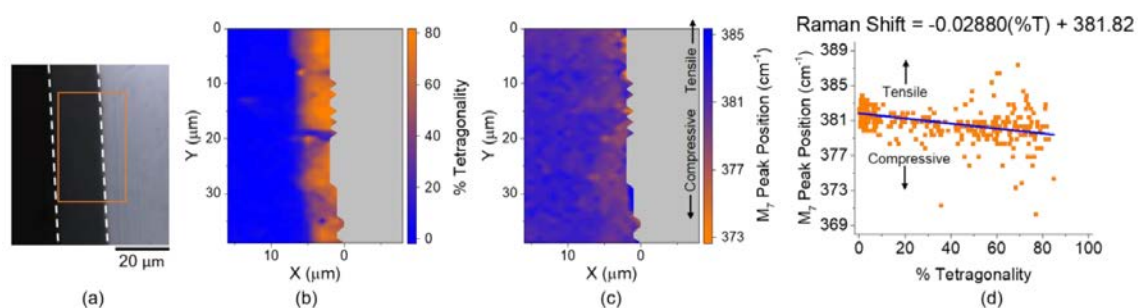


**Figure A.3:** (a) Optical image of pre-breakaway Zr sectioned sample. White lines separate (left) epoxy/oxide and (right) oxide/metal interfaces. Orange rectangle displays collected Raman map area. (b) Percent tetragonality and (c) position of the  $M_7$  peak as a function of location. Grey represents metal, where Raman peaks are non-apparent. (d) Percent tetragonality as a function of the  $M_7$  peak position for the data collected in the Raman map.

Similar effects were accomplished for each zirconium alloy, both pre- and post-breakaway (Figure A.4). In general, the post-breakaway Zr, Zry-3, and Zry-4 show signs of the “relaxed” tetragonal zone in the bulk of the oxide. Kurpaska et al describe stability of this relaxed tetragonal phase as unrelated to high compressive stress tensor, and rather induced by sub-stoichiometry of the oxide, as it relates to porosity of the scale [20]. In other words, this is a stress-free grown tetragonal zirconia that forms within the bulk of the

monoclinic zirconia scale, developed by a lack of available oxygen to form monoclinic zirconia.

All pre-breakaway samples did not display this relaxed tetragonal phase; tetragonal-rich zirconia was seen only in the few microns nearest the metal/oxide interface. The exception to this distinction is the pre-breakaway Zry-4. This Raman map displays high tetragonality on the epoxy side of the oxide, which are observed as “relaxed” tetragonal peaks with lower wavenumbers (e.g., less than  $265\text{ cm}^{-1}$ ) than those peaks seen in the stress-stabilized tetragonal zirconia at the metal/oxide interface.

As for percent tetragonality and compressive stress, all samples except for Zry-4 pre-breakaway show a general correlation between the two measured parameters. As was stated before, there is a notable increase in scatter for the high percent tetragonality spectra. This could be contributed to the addition of relaxed tetragonal phase in the data. However, this increase in scatter is also seen in Raman maps where no relaxed tetragonal zirconia is seen.

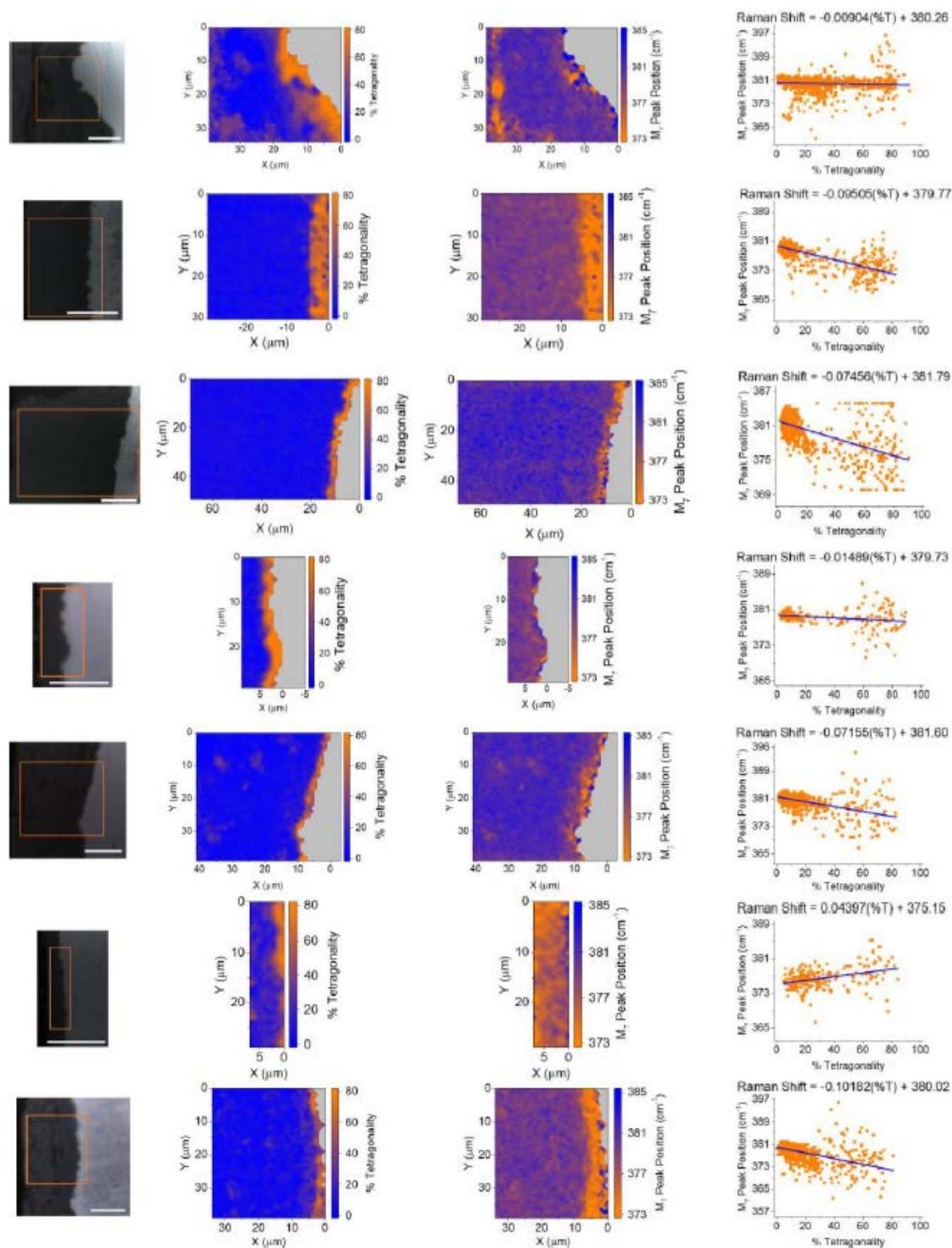


**Figure A.4:** Raman mapping analysis for (top to bottom) post-breakaway Zr, pre- and post-breakaway Zr-2.65Nb, pre- and post-breakaway Zry-3, pre- and post-breakaway Zry-4.

#### A.4.3 Scanning Kelvin Probe Force Microscopy

SKPFM mapping provides nano-scale spatial resolution of relative Volta potentials seen at and around the metal/oxide interface for zirconium and its alloy. SKPFM has been used in the corrosion community to quantify relative nobility of different microstructural features for many materials. This technique has yet to be realized with regards to zirconium alloys used in nuclear cladding applications. Figure A.5 presents topography and SKPFM maps of pre- and post-breakaway samples.

Segregation between oxide and metal is noted on both topography and potential maps. Interestingly, the measurable Volta potential of the oxide is less than the Volta potential of the metal in each image of pure Zr sample. This is contrary to expectation, as it would be assumed that a ceramic oxide would intrinsically have a greater work function (and thus greater relative Volta potential) than zirconium metal. This contradiction is furthered when observing the Zr-2.65Nb, Zry-3, and Zry-4 SKPFM maps. Here, it can be seen that the oxide consistently displays, as expected, a higher Volta potential than the metal. Also of note is after an initial peak in Volta for the oxide of post-breakaway Zry-4, there is a noticeable drop in the Volta potential. Additionally, micro features are seen in many of the maps, which display much higher potentials than the surroundings (Zr, Zry-3, and Zry-4). This represents a key benefit of SKPFM, which is commonly utilized to recognize phase separation in metal alloys. These secondary particles are likely caused by the inclusions of iron, tin, and/or chromium, which tend to phase separate and cause lattice mismatches in zirconium.

Another benefit of SKPFM is the utility of observing both metal and oxide, rather than solely oxide with Raman. With this addition of the metal, the transition from metal to oxide can be observed.

Plausible future utility of SKPFM is the detection of hydrogen precipitation in the oxide and metal. Hydrogen-enriched zones have been detected with SKPFM on a variety of metals [54-65]. Therefore, SKPFM should be able to provide similar rapid, non-destructive examination of hydrogen embrittlement within zirconium alloys. Establishing SKPFM as a high-resolution characterization technique can potentially improve the understanding of cladding degradation mechanisms.

Co-localized areas of many samples were accomplished with SKPFM and Raman mapping. Co-localization of these two techniques provide the opportunity to compare crystallographic information via Raman to electronic properties via SKPFM. As SKPFM is relatively less destructive, as well as done in an inert environment and is highly sensitive to surface reactions, this technique was done prior to Raman mapping. Co-localization was accomplished on Zr, Zr-2.65Nb, pre-breakaway Zry-3, and post-breakaway Zry-4.

For example, on post-breakaway Zr a similar co-localized feature can be seen near the metal oxide interface, presented as a high VPD particle from SKPFM (Figure A.5) and low tetragonality in an otherwise highly tetragonal area from Raman (Figure A.4).

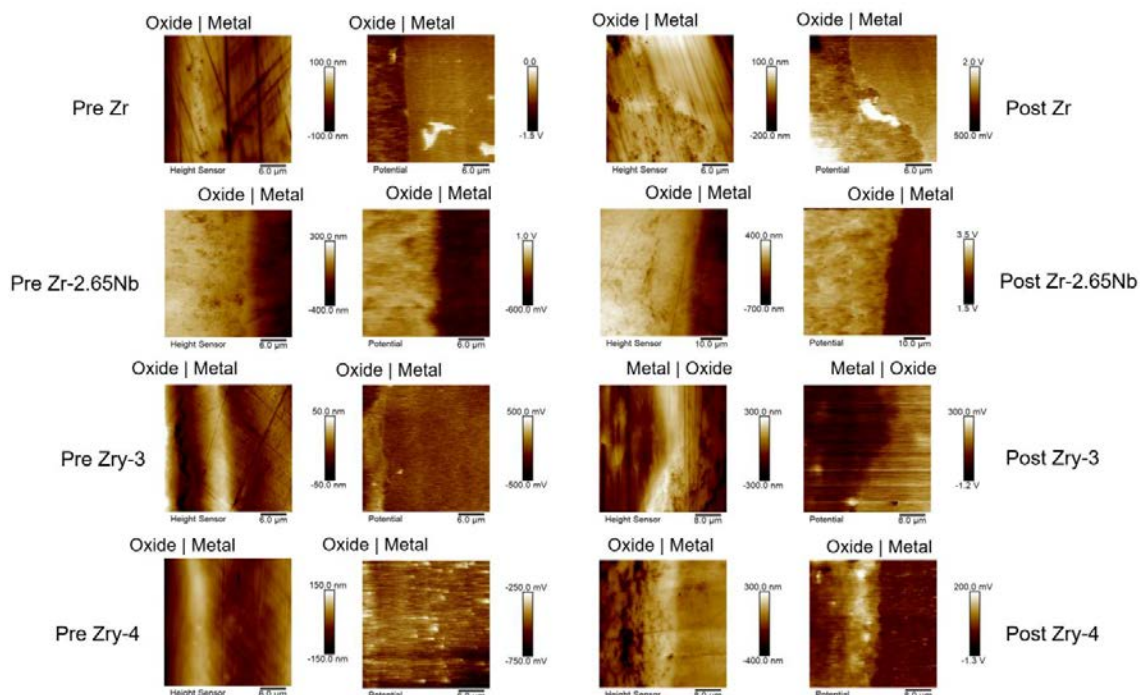


**Figure A.5: Topography (left) and Volta potential (right) maps for pre- and post-breakaway Zr, Zr-2.65Nb, Zry-3, and Zry-4. Oxide/metal interfaces are noted in each map.**

#### A.4.4 Atom Probe Tomography

APT tips at the metal/oxide interface were successfully acquired and analyzed for pre-breakaway Zr (Figure A.6) and post-breakaway Zr-2.65Nb (Figure A.7). On the pre-breakaway Zr sample, there is evidence of  $Zr(O)_{ads}$  region at the boundary between the metal and oxide, confirming other's results [7,35,66] This is also in agreement with the general oxide formation model presented by Motta et al, where oxygen diffusion forms a metastable region at the interface [8]. On the post-breakaway Zr-2.65Nb sample, a differing composition is seen at the interface. It can be seen that the  $Zr(O)_{ads}$  region is much thicker, as both top and bottom of the tip is made up of 52-54 at. % Zr. However, in the middle of these regions there are two different tiers showing closer to 1:1 Zr:O percentages. Additionally, the amount of niobium observed in this volume (ranging from 0.4-0.7 at. %) is much less than expected. It is also notable that there is a high and even distribution of

iron across the volume, which is contrary to the concentrated secondary particles observed in Zry-3 and Zry-4 alloys.

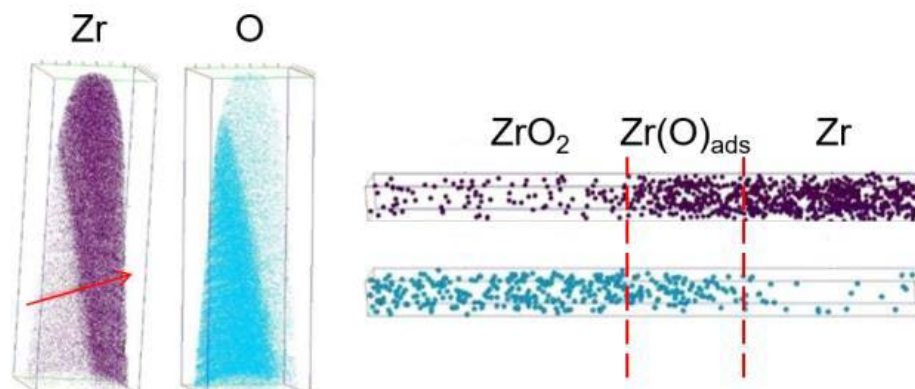


**Figure A.6:** APT results from pre-breakaway Zr sample. (Left) Tip dimensions are  $75.9 \times 74.6 \times 223.8 \text{ nm}^3$ , with the arrow representing a  $4 \times 4 \times 60 \text{ nm}^3$  volume. (Right) 1D concentration profile of zirconium and oxygen, with phases segregated. Fixed bin size of 0.5 nm was used.

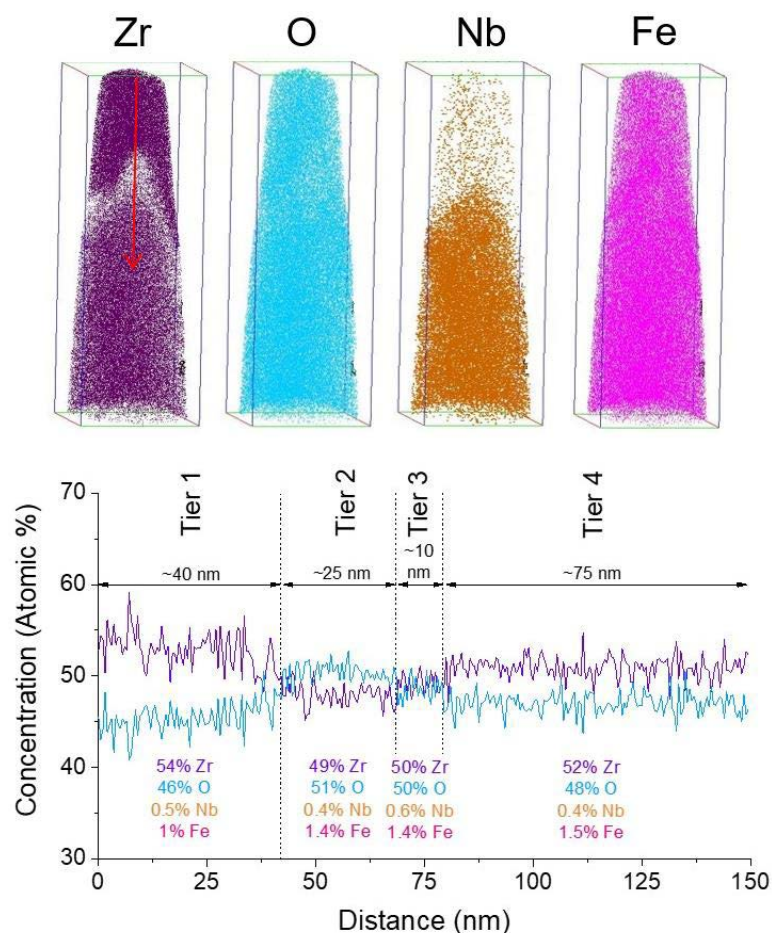


**Figure A.7:** APT results from post-breakaway Zr-2.65Nb sample. (Top) Tip dimensions are  $103.8 \times 97.9 \times 285.7 \text{ nm}^3$ , with the arrow representing a  $5 \times 5 \times 150 \text{ nm}^3$  volume. (Bottom) 1D concentration profile of zirconium and oxygen across the volume, with average concentrations noted in each “tier”. Fixed bin size of  $0.5 \text{ nm}$  was used.

## A.5 Conclusions

Observing specific features of Raman spectra can provide insight into the mechanisms at play during zirconium oxide growth. Post-examination Raman of sectioned oxides, with the use of quantitative formulas, provided mapping of percent tetragonality and relative residual stress for Zr, Zr-2.65Nb, Zry-3, and Zry-4 alloys at points before and after breakaway. A general trend of increasingly compressive stress as a function of

increased tetragonal zirconia volume was seen. However, the idea of linear correlation between crystal makeup and stress development is in question; there may perhaps be additional factors that support either of these factors, and how they drive the breakaway phenomenon.

SKPFM was used for the first time to examine oxidized zirconium alloys. With SKPFM, distinguishing different phases was accomplished, both at the metal/oxide interface, as well as when observing secondary phase separation. This tool may be feasible to provide further insight into degradation of zirconium alloys, with applications in relative phase nobility, hydrogen detection, and other possible utilities yet to be discovered.

APT was used to observe atomistic make-up of the region about the metal/oxide interface, presenting differences in  $\text{Zr(O)}_{\text{ads}}$  region between pre- and post-breakaway samples. Post-breakaway Zr-2.65Nb showed “tiers” of differing elemental make-up within the  $\text{Zr(O)}_{\text{ads}}$  region.

These different characterization techniques are useful to improve understanding of oxidation mechanisms of zirconium cladding materials. In addition, they can be used to support development of sensors, particularly in confirming EIS modelling of cladding oxide growth.

## **A.6 Acknowledgments**

The authors acknowledge the In-Pile Instrumentation Initiative (I2) sponsored by the Department of Energy (DOE). Paul H. Davis, Elton Graugnard, and Bill Knowlton of the Boise State Surface Science Laboratory, as well as Jatuporn Burns and Megha Dubey of CAES are thanked for their support. FIB and APT were done at Microscopy and

Characterization Suite (MaCS) in CAES. The authors also acknowledge the departmental support from Boise State's Micron School of Materials Science and Engineering.

### A.7 References

- [1] N. Stojilovic, E.T. Bender, R.D. Ramsier, Surface chemistry of zirconium, *Prog. Surf. Sci.* 78 (2005) 101–184. doi:10.1016/j.progsurf.2005.07.001.
- [2] A. Couet, A.T. Motta, A. Ambard, D. Livigni, In-situ electrochemical impedance spectroscopy measurements of zirconium alloy oxide conductivity : Relationship to hydrogen pickup, *Eval. Program Plann.* 119 (2017) 1–13. doi:10.1016/j.corsci.2016.12.008.
- [3] B. Cox, Some thoughts on the mechanisms of in-reactor corrosion of zirconium alloys, *J. Nucl. Mater.* 336 (2005) 331–368. doi:10.1016/j.jnucmat.2004.09.029.
- [4] B. Cox, The oxidation and corrosion of zirconium and its alloys, *J. Electrochem. Soc.* 108 (1961) 24–30.
- [5] C. Proff, S. Abolhassani, C. Lemaignan, Oxidation behaviour of binary zirconium alloys containing intermetallic precipitates, *J. Nucl. Mater.* 416 (2011) 125–134. doi:10.1016/j.jnucmat.2010.11.099.
- [6] J. Wei, P. Frankel, E. Polatidis, M. Blat, A. Ambard, R.J. Comstock, The effect of Sn on autoclave corrosion performance and corrosion mechanisms in Zr – Sn – Nb alloys, *Acta Mater.* 61 (2013) 4200–4214.
- [7] N. Ni, D. Hudson, J. Wei, P. Wang, S. Lozano-Perez, G.D.W. Smith, J.M. Sykes, S.S. Yardley, K.L. Moore, S. Lyon, R. Cottis, M. Preuss, C.R.M. Grovenor, How the crystallography and nanoscale chemistry of the metal/oxide interface develops during the aqueous oxidation of zirconium cladding alloys, *Acta Mater.* 60 (2012) 7132–7149. doi:10.1016/j.actamat.2012.09.021.
- [8] A.T. Motta, A. Couet, R.J. Comstock, Corrosion of Zirconium Alloys Used for Nuclear Fuel Cladding, (n.d.). doi:10.1146/annurev-matsci-070214-020951.
- [9] D.H. Bradhurst, P.M. Heuer, Influence of oxide stress on the breakaway behavior of Zircaloy-2, *J. Nucl. Mater.* (1970) 35–47. doi:10.1111/cpr.12282.

- [10] K.B. Chong, M.E. Fitzpatrick, Evolution of stress fields and phase content in corroded zirconium cladding materials, *Surf. Coat. Technol.* 324 (2017) 140–145. doi:10.1016/j.surfcoat.2017.05.072.
- [11] A. Couet, A.T. Motta, A. Ambard, The coupled current charge compensation model for zirconium alloy fuel cladding oxidation : I . Parabolic oxidation of zirconium alloys, *Corros. Sci.* 100 (2015) 73–84. doi:10.1016/j.corsci.2015.07.003.
- [12] M. Oskarsson, E. Ahlberg, K. Pettersson, Oxidation of Zircaloy-2 and Zircaloy-4 in water and lithiated water at 360 °C, *J. Nucl. Mater.* 295 (2001) 97–108.
- [13] A. Zielinski, S. Sobieszczyk, Hydrogen-enhanced degradation and oxide effects in zirconium alloys for nuclear applications, *Int. J. Hydrogen Energy.* 36 (2011) 8619–8629.
- [14] C. Duriez, D. Drouan, G. Pouzadoux, Reaction in air and in nitrogen of pre-oxidised Zircaloy-4 and M5<sup>TM</sup> claddings, *J. Nucl. Mater.* 441 (2013) 84–95. doi:10.1016/j.jnucmat.2013.04.095.
- [15] C. Duriez, T. Dupont, B. Schmet, F. Enoch, Zircaloy-4 and M5<sup>®</sup> high temperature oxidation and nitriding in air, *J. Nucl. Mater.* 380 (2008) 30–45. doi:10.1016/j.jnucmat.2008.07.002.
- [16] I. Idarraga, M. Mermoux, C. Duriez, a. Crisci, J.P. Mardon, Potentialities of Raman Imaging for the Analysis of Oxide Scales Formed on Zircaloy-4 and M5<sup>®</sup> in Air at High Temperature, *Oxid. Met.* 79 (2012) 289–302. doi:10.1007/s11085-012-9331-5.
- [17] I. Idarraga, M. Mermoux, C. Duriez, a. Crisci, J.P. Mardon, Raman investigation of pre- and post-breakaway oxide scales formed on Zircaloy-4 and M5<sup>®</sup> in air at high temperature, *J. Nucl. Mater.* 421 (2012) 160–171. doi:10.1016/j.jnucmat.2011.11.071.
- [18] M. Lasserre, V. Peres, M. Pijolat, O. Coindreau, C. Duriez, J.P. Mardon, Modelling of Zircaloy-4 accelerated degradation kinetics in nitrogen–oxygen

- mixtures at 850°C, *J. Nucl. Mater.* 462 (2015) 221–229.  
doi:10.1016/j.jnucmat.2015.03.052.
- [19] M. Lasserre, V. Peres, M. Pijolat, O. Coindreau, C. Duriez, J.P. Mardon, Qualitative analysis of Zircaloy-4 cladding air degradation in O<sub>2</sub>-N<sub>2</sub> mixtures at high temperature, *Mater. Corros.* 65 (2014) 250–259.
- [20] L. Kurpaska, J. Favergeon, L. Lahoche, M. El-marssi, J.G. Poussard, Raman spectroscopy analysis of air grown oxide scale developed on pure zirconium substrate, *J. Nucl. Mater.* 466 (2015) 460–467.  
doi:10.1016/j.jnucmat.2015.06.005.
- [21] E.T. Hayes, A.H. Roberson, Some effects of heating zirconium in air, oxygen, and nitrogen, *J. Electrochem. Soc.* 96 (1949) 142–151.
- [22] M. Guerain, C. Duriez, J.L. Grosseau-poussard, M. Mermoux, Review of stress fields in Zirconium alloys corrosion scales, *Corros. Sci.* 95 (2015) 11–21.  
doi:10.1016/j.corsci.2015.03.004.
- [23] L. Kurpaska, J. Favergeon, L. Lahoche, On the determination of growth stress during oxidation of pure zirconium at elevated temperature, *Appl. Surf. Sci.* 446 (2018) 27–35.
- [24] L. Kurpaska, J. Favergeon, J. Grosseau-poussard, L. Lahoche, G. Moulin, In-situ stress analysis of the Zr/ZrO<sub>2</sub> system as studied by Raman spectroscopy and deflection test in monofacial oxidation techniques, *Appl. Surf. Sci.* 385 (2016) 106–112. doi:10.1016/j.apsusc.2016.05.074.
- [25] L. Kurpaska, M. Lesniak, R. Jadach, Shift in low-frequency vibrational spectra measured in-situ at 600 °C by Raman spectroscopy of zirconia developed on pure zirconium and Zr-1%Nb alloy, *J. Mol. Struct.* 1126 (2016) 186–191.
- [26] L. Kurpaska, M. Kozanecki, J.J. Jasinski, M. Sitarz, Stress analysis of zirconia studied by Raman spectroscopy at low temperatures, *Spectrochim. Acta Part A Mol. Biomol. Spectrosc.* 131 (2014) 691–695. doi:10.1016/j.saa.2014.05.023.

- [27] L. Kurpaska, J. Favergeon, Zirconia Layer Formed by High Temperature Oxidation of Pure Zirconium: Stress Generated at the Zirconium/Zirconia Interface, (2013) 261–277. doi:10.1007/s11085-012-9348-9.
- [28] P. Barberis, G. Corolleur-Thomas, R. Guinebretiere, Raman spectra of tetragonal zirconia: powder to zircaloy oxide frequency shift, *J. Nucl. Mater.* 288 (2001) 241–247.
- [29] P. Barberis, T. Merle-mrjean, On Raman spectroscopy of zirconium oxide films, 246 (1997) 232–243.
- [30] O.I. Malyi, P. Wu, V.V. Kulish, Formation and migration of oxygen and zirconium vacancies in cubic zirconia and zirconium oxysulfide, *Solid State Ionics.* 212 (2012) 117–122.
- [31] C. Duriez, M. Steinbrück, D. Ohai, T. Meleg, J. Birchley, T. Haste, Separate-effect tests on zirconium cladding degradation in air ingress situations, *Nucl. Eng. Des.* 239 (2009) 244–253. doi:10.1016/j.nucengdes.2008.10.017.
- [32] M. Steinbrück, M. Böttcher, Air oxidation of Zircaloy-4, M5® and ZIRLO™ cladding alloys at high temperatures, *J. Nucl. Mater.* 414 (2011) 276–285. doi:10.1016/j.jnucmat.2011.04.012.
- [33] M. Steinbrück, N. Ver, M. Grosse, Oxidation of advanced zirconium cladding alloys in steam at temperatures in the range of 600-1200 °C, *Oxid. Met.* 76 (2011) 215–232.
- [34] M. Steinbrück, Prototypical experiments relating to air oxidation of Zircaloy-4 at high temperatures, *J. Nucl. Mater.* 392 (2009) 531–544. doi:10.1016/j.jnucmat.2009.04.018.
- [35] B. De Gabory, Y. Dong, A.T. Motta, E.A. Marquis, EELS and atom probe tomography study of the evolution of the metal/oxide interface during zirconium alloy oxidation, *J. Nucl. Mater.* 462 (2015) 304–309. doi:10.1016/j.jnucmat.2015.03.043.
- [36] D.R. Olander, W.E. Wang, Y.S. Kim, Chemical processes in defective LWR fuel rods, *J. Nucl. Mater.* 248 (1997) 214–219.

- [37] B. Michel, J. Sercombe, G. Thouvenin, 3D fuel cracking modelling in pellet cladding mechanical interaction, *Eng. Fract. Mech.* 75 (2008) 3581–3598.
- [38] H.K. Jenssen, PIE results and mechanistic interpretation on on-line EIS data from the cladding corrosion test IFA-731, (2017).
- [39] C.M. Efaw, Toward improving ambient volta potential measurements with SKPFM for corrosion studies, *J. Electrochem. Soc.* 166 (2019).
- [40] C. Ciszak, M. Mermoux, S. Miro, Micro-Raman analysis of the fuel-cladding interface in a high burnup PWR fuel rod, *J. Nucl. Mater.* 495 (2017) 392–404. doi:10.1016/j.jnucmat.2017.08.038.
- [41] A. Kasperski, M. Guerain, M. Mermoux, F. Jomard, High-temperature oxidation of Zircaloy-4 in air studied with labeled oxygen and Raman imaging, *Oxid. Met.* 87 (2017) 501–513. doi:10.1007/s11085-017-9713-9.
- [42] L. Kurpaska, M. Frelek-Kozak, J.L. Grosseau-Poussard, Identification of the zirconia phases by means of Raman spectroscopy for specimens prepared by FIB lift-out technique, *Oxid. Met.* 88 (2017) 521–530.
- [43] M. Guerain, M. Mermoux, C. Duriez, The use of micro-Raman imaging to measure  $^{18}\text{O}$  tracer distribution in thermally grown zirconia scales, *Corros. Sci.* 98 (2015) 140–149. doi:10.1016/j.corsci.2015.05.020.
- [44] H. Mi, S. Mikael, T. Allen, K. Sridharan, D. Butt, J.P. Blanchard, Z. Ma, Monitoring the oxidation of nuclear fuel cladding using Raman spectroscopy, *J. Nucl. Mater.* 445 (2014) 7–11. doi:10.1016/j.jnucmat.2013.10.052.
- [45] M. Ishigame, Temperature dependence of Raman spectra of  $\text{ZrO}_2$ , *J. Am. Ceram. Soc.* 60 (1977) 367.
- [46] C.M. Phillippi, K.S. Mazdiyasi, Infrared and Raman spectra of zirconia polymorphs, *J. Am. Ceram. Soc.* 54 (1971) 254.
- [47] V.G. Keramidis, Raman scattering study of the crystallization and phase transformations of  $\text{ZrO}_2$ , *J. Am. Ceram. Soc.* 57 (1974) 22.

- [48] G.G. Siu, M.J. Stokes, Y.L. Liu, Variation of fundamental and higher-order Raman spectra of ZrO<sub>2</sub> nanograins with annealing temperature, *Phys. Rev. B.* 59 (1999) 3173–3179.
- [49] O-Zr Phase Diagram, ASM Int. (2009) Diagram No. 101191.
- [50] S. Block, Pressure-temperature phase diagram of zirconia, *J. Am. Ceram. Soc.* 68 (1985) 497.
- [51] D.R. Clarke, F. Adar, Measurement of the crystallographically transformed zone produced by fracture in ceramics containing tetragonal zirconia, *J. Am. Ceram. Soc.* 65 (1982).
- [52] J. Godlewski, AS, ASTM-STP, 1132. (1991).
- [53] L. Kurpaska, Structural properties of zirconia-in-situ high temperature XRD characterization, *J. Mol. Struct.* 1163 (2018) 287–293.
- [54] Z.L. Hua, Scanning Kelvin probe force microscopy study on hydrogen distribution in austenitic stainless steel after martensitic transformation, *Mater. Lett.* 245 (2019) 41–44.
- [55] Z. Hua, S. Zhu, B. An, The finding of hydrogen trapping at phase boundary in austenitic stainless steel by scanning Kelvin probe force microscopy, *Scr. Mater.* 162 (2019) 219–222.
- [56] Z. Hua, D. Wang, Z. Liu, Hydrogen distribution at twin boundary in austenitic stainless steel studied by scanning Kelvin probe force microscopy, *Mater. Lett.* 234 (2019) 175–178.
- [57] Z. Hua, B. An, T. Iijima, The finding of crystallographic orientation dependence of hydrogen diffusion in austenitic stainless steel by scanning Kelvin probe force microscopy, *Scr. Mater.* 131 (2017) 47–50.
- [58] S. Kolsch, F. Fritz, M.A. Fenner, Kelvin probe force microscopy studies of the charge effects upon adsorption of carbon nanotubes and C-60 fullerenes on hydrogen-terminated diamond, *J. Appl. Phys.* 123 (2018).

- [59] M.C. Lafouresse, M.L. de Bonfils-Lahovary, C. Charvillat, A Kelvin probe force microscopy study of hydrogen insertion and desorption into 2024 aluminum alloy, *J. Alloys Compd.* 722 (2017) 760–766.
- [60] S. Evers, C. Senoz, M. Rohwerder, Hydrogen detection in metals: A review and introduction of a Kelvin probe approach, *Sci. Technol. Adv. Mater.* 14 (2013).
- [61] C. Larignon, J. Alexis, E. Andrieu, Investigation of Kelvin probe force microscopy efficiency for the detection of hydrogen ingress by cathodic charging in an aluminum alloy, *Scr. Mater.* 68 (2013) 479–482.
- [62] L. Oger, M.C. Lafouresse, G. Odemer, Hydrogen diffusion and trapping in a low copper 7xxx aluminum alloy investigated by Scanning Kelvin Probe Force Microscopy, *Mater. Sci. Eng. A- Struct. Mater. Prop. Microstruct. Process.* 706 (2017) 126–135.
- [63] G. Wang, Y. Yan, X. Yang, Investigation of hydrogen evolution and enrichment by scanning Kelvin probe force microscopy, *Electrochem. Commun.* 35 (2013) 100–103.
- [64] W. Burgstaller, G. Schimo, A.W. Hassel, Challenges in hydrogen quantification using Kelvin probe technique at different levels of relative humidity, *J. Solid State Electrochem.* 21 (2017) 1785–1796.
- [65] C. Senoz, S. Evers, M. Stratmann, Scanning Kelvin Probe as a highly sensitive tool for detecting hydrogen permeation with high local resolution, *Electrochem. Commun.* 13 (2011) 1542–1545.
- [66] Y. Dong, A.T. Motta, E. a. Marquis, Atom probe tomography study of alloying element distributions in Zr alloys and their oxides, *J. Nucl. Mater.* 442 (2013) 270–281. doi:10.1016/j.jnucmat.2013.08.055.